# MESENCHYMAL STEM CELL THERAPIES FOR THE TRABECULAR MESHWORK IN GLAUCOMA

A Dissertation
Presented to
The Academic Faculty

By

Eric J. Snider

In Partial Fulfillment
of the Requirements for the Degree
Doctor of Philosophy in the
Wallace H. Coulter
Department of Biomedical Engineering

Georgia Institute of Technology
Emory University
May 2018

# MESENCHYMAL STEM CELL THERAPIES FOR THE TRABECULAR MESHWORK IN GLAUCOMA

Approved by:


Dr. C. Ross Ethier, Advisor
The Wallace H. Coulter
Department of Biomedical Engineering
*Georgia Institute of Technology*
*Emory University School of Medicine*

Dr. Andrés García
The George W. Woodruff
School of Mechanical Engineering
*Georgia Institute of Technology*

Dr. Mark Prausnitz
School of Chemical & Biomolecular
Engineering
*Georgia Institute of Technology*

Dr. Chunhui Xu
Department of Pediatrics
*Emory University School of Medicine*

Dr. W. Daniel Stamer
Department of Ophthalmology
*Duke University School of Medicine*


Date Approved: December 14, 2017

# ACKNOWLEDGEMENTS

Without the support and help of many individuals, this dissertation would not have been possible. I would like to sincerely extend thanks to everyone that had a positive impact on my research over the past 4 years.

I would like to express my deepest appreciation to my advisor, Dr. C. Ross Ethier, who provided me with the resources and space I needed to pursue my own ideas. Thanks for providing advice when experiments did not go as expected, and for thorough edits of my dissertation and other publications. Without your guidance throughout this process, I would not be where I am today.

I would like to acknowledge my thesis committee for overseeing my dissertation research these past few years and providing essential feedback. Specifically, I would like to thank Dr. W. Daniel Stamer for project advice from the very beginning as well as allowing me to visit and learn key techniques from your research group at Duke University.

I also would like to thank the research group in the Ethier lab for support and great ideas along the way. Specifically, I should thank Dr. Lisa Schildmeyer and Dr. Thomas Read for their assistance with cell culture and histology, respectively.

I would not have accomplished every project aspect without the assistance from my team of undergraduates. I have had the privilege of working with 11 undergraduate students that assisted me in designing, conducting (no matter how tedious), and analyzing experiments throughout my dissertation research. Without their help, this dissertation would not be in the form it is today. I also would like to thank the Project

ENGAGES program for providing me with two great high school students that assisted with my project over the years.

I would like to thank our ultrasound and photoacoustic imaging collaborators in Dr. Stanislav Emelianov's research group at Georgia Tech for contributing sizably to my dissertation. Specifically, I acknowledge Kelsey Kubelick for conducting many experiments along the way and putting up with my hectic schedule these past few months.

Finally, I must thank my family and friends for providing support during the stressful moments, dealing with my frantic schedule, and providing moments of escape from the dissertation process. Without this support, this dissertation would not have been possible.

# TABLE OF CONTENTS

**Acknowledgements** ..... **II**
**List of Tables** ..... **VIII**
**List of Figures** ..... **IX**
**Nomenclature** ..... **XVII**
**Summary** ..... **XX**
**Chapter 1. Introduction** ..... **1**
**1.1 Glaucoma** ..... **1**
**1.2 Aqueous Humor Dynamics** ..... **1**
**1.3 Current Glaucoma Therapeutics** ..... **3**
**1.4 Trabecular Meshwork** ..... **4**
1.4.1 Trabecular Meshwork Structure ..... 4
1.4.2 Trabecular Meshwork Tissue Function ..... 5
1.4.3 Trabecular Meshwork Cells ..... 6
1.4.4 Trabecular Meshwork During Glaucoma ..... 7
**1.5 Regenerative Medicine Therapies** ..... **8**
**1.6 Stem Cell therapies for the Trabecular Meshwork** ..... **9**
1.6.1 Native TM Stem Cells ..... 9
1.6.2 Induced Pluripotent Stem Cells ..... 10
1.6.3 Mesenchymal Stem Cells ..... 11
**Chapter 2. Specific Aims** ..... **14**
**Chapter 3. Characterize Differences Between Mesenchymal Stem Cells and Trabecular Meshwork Cells at RNA, Protein, and Functional Levels** ..... **17**
**3.1 Abstract** ..... **17**
**3.2 Introduction** ..... **18**
**3.3 Materials and Methods** ..... **20**
3.3.1 Mesenchymal Stem Cell Sourcing and Characterization ..... 20
3.3.2 Trabecular Meshwork Cell Sourcing and Characterization ..... 21
3.3.3 Reverse Transcription Quantitative PCR (RT-qPCR) ..... 22
3.3.4 Dexamethasone Induction of Myocilin ..... 23
3.3.5 Western Blotting ..... 24
3.3.6 Flow Cytometry ..... 25
3.3.7 Collagen Gel Contractility ..... 26
3.3.8 Phagocytosis Assessment ..... 27

3.3.9 Statistics....28
**3.4 Results....28**
3.4.1 Mesenchymal Stem Cell Characterization....28
3.4.2 Reverse Transcription Quantitative PCR....29
3.4.3 Dexamethasone Induction of MYOC....31
3.4.4 Additional Protein Markers....33
3.4.5 Collagen Gel Contractility....34
3.4.6 Phagocytosis....35
**3.5 Discussion....36**
**3.6 Conclusions....41**
**3.7 Acknowledgments....41**
**Chapter 4. An Ultrasound-Photoacoustic Imaging Platform for Visualizing Mesenchymal Stem Cell Delivery and Retention in the Trabecular Meshwork....42**
**4.1 Abstract....42**
**4.2 Introduction....43**
**4.3 Methods and Materials....46**
4.3.1 Mesenchymal Stem Cell Sourcing....46
4.3.2 Gold Nanotracer Synthesis....47
4.3.3 AuNS and CFSE Stem Cell Labeling....47
4.3.4 Stem Cell Delivery in ex vivo Experiments....48
4.3.5 Anterior Segment Dissection....49
4.3.6 Ultrasound-Photoacoustic Imaging of Porcine Eyes....49
4.3.7 Fluorescence Microscopy....50
4.3.8 Image Analysis....51
Statistics....53
**4.4 Results....53**
4.4.1 Labeling MSCs with AuNS and Their Corresponding Spectra....53
4.4.2 US-PA Imaging of AuNS-MSC Injections into the Anterior Segment....55
4.4.3 Detection of AuNS-MSCs in TM, 5 hours Post-Delivery....56
4.4.4 Assessment of MSC delivery to the TM....58
4.4.5 Correlation of MSC Distribution Between US-PA and Fluorescent Images....60
**4.5 Discussion....61**
**4.6 Conclusions....64**
**4.7 Acknowledgments....65**

**Chapter 5. Improving Mesenchymal Stem Cell Delivery to the Trabecular Meshwork Using Magnetic Nanoparticles ..... 66**

**5.1 Abstract ..... 66**

**Introduction ..... 67**

**5.2 Methods and Materials ..... 69**

5.2.1 Mesenchymal Stem Cell Sourcing ..... 69

5.2.2 PBNC Nanoparticle Synthesis and Characterization ..... 69

5.2.3 MSC Fluorescent and PBNC Labeling ..... 71

5.2.4 Organ Cultured Porcine Eyes ..... 72

5.2.5 PBNC-MSC magnetically steered delivery ..... 74

5.2.6 Fluorescent microscopy and quantification ..... 75

5.2.7 Histology ..... 77

5.2.8 Live-Dead Assessment of Effects of PBNCs on MSCs in vitro ..... 77

5.2.9 Stem Cell Multipotency Assessment in vitro ..... 78

5.2.10 Statistics ..... 79

**5.3 Results ..... 80**

5.3.1 MSCs Uptake PBNCs ..... 80

5.3.2 PBNC-MSCs Can Be Steered by Magnetic Fields ..... 82

5.3.3 Optimizing Magnetic Field Exposure Time ..... 85

5.3.4 Improving Delivery Efficiency to the Entire TM with PBNCs ..... 89

5.3.5 Histological Assessment of the TM After PBNC-MSC Delivery ..... 92

5.3.6 Toxicity of PBNCs on MSCs in vitro ..... 93

5.3.7 Effect of PBNCs on MSC Multipotency ..... 96

**5.4 Discussion ..... 98**

**5.5 Conclusions ..... 102**

**5.6 Acknowledgements ..... 103**

**Chapter 6. Development of a Porcine Organ-Culture Glaucoma Model Mimicking Trabecular Meshwork Damage ..... 104**

**6.1 Abstract ..... 104**

**6.2 Introduction ..... 105**

**6.3 Methods and Materials ..... 107**

6.3.1 Cell Sourcing ..... 107

6.3.2 Exposure of Cells to Hydrogen Peroxide in vitro ..... 110

6.3.3 pTM Cell Characterization After $H_2O_2$Treatment ..... 111

6.3.4 Porcine Anterior Segment Organ Culture ..... 113

6.3.5 Hydrogen Peroxide Treatment in Organ Culture ..... 114

6.3.6 Organ Culture Characterization ..... 115
6.3.7 Stem Cell Delivery to the TM ..... 118
6.3.8 Statistics ..... 119
**6.4 Results ..... 119**
6.4.1 Effect of $H_2O_2$ on pTM Cell Viability in vitro ..... 120
6.4.2 Functional assessment of $H_2O_2$-treated pTM cells ..... 121
6.4.3 IOP homeostasis after $H_2O_2$ treatment ..... 123
6.4.4 Live-Dead Assessment of Porcine TM After $H_2O_2$ Treatment ..... 126
6.4.5 Histological Assessment of $H_2O_2$-Treated Eyes ..... 127
6.4.6 MSC Delivery to $H_2O_2$-Treated Anterior Segments ..... 129
**6.5 Discussion ..... 130**
**Chapter 7. Conclusions ..... 134**
**References ..... 140**

# LIST OF TABLES

Table 1. Primer Sequences Used in RT-qPCR Experiments. Primers are organized based on different categories (e.g. reference, TM cell marker). Primers were selected from indicated references or designed using Primer-Blast when indicated. Sequences selected from PrimerBank database show corresponding PrimerBank IDs.....23

Table 2. Flow cytometry Primary Antibodies and Respective Isotypes. Dilution, supplier, and catalog numbers for each antibody and isotype used for flow cytometry experiments are shown.....25

Table 3. Primer Sequences Used in RT-qPCR Experiments. Primers were selected using Primer-Blast (NCBI) software following established protocols (Ye et al., 2012). .109

Table 4. Baseline IOP for Control and $H_2O_2$-treated eyes. Baseline IOP values were averaged for 10 hours of IOP reading for each untreated or $H_2O_2$-treated anterior segment (n = 9 for each condition). Average differences between each condition were not significant (p = 0.15) as determined by a paired Student's t-test.....124

# LIST OF FIGURES

Figure 1. IOP Regulation in the Anterior Chamber. Intraocular pressure is determined by the rate of aqueous humor inflow from the ciliary body and by the resistance to outflow of this fluid, primarily through the trabecular meshwork (Goel et al., 2010). ..... 2

Figure 2. The Anterior Chamber and Trabecular Meshwork. (A) The position of the anterior chamber and chamber angle (grey box) in a human eye. (B) The chamber angle and TM (black box), and (C) further magnified view of the TM and Schlemm's canal. (Kempf et al., 2013). ..... 5

Figure 3. Trabecular Meshwork Microstructure. The three different regions of the TM. The direction of aqueous humor flow is from bottom to top in the above micrograph. SC denotes Schlemm's canal, JCT denotes juxtacanalicular tissue, CTM denotes cornealscleral TM, UTM denotes uveal TM, and AC denotes the anterior chamber (Tamm, 2009). ..... 6

Figure 4. Mesenchymal Stem Cell Characterization. (A-B) Surface marker characterization by flow cytometry for MSC markers: (A) shows CD90, a positive marker and (B) shows CD45, a negative marker. Stained samples were compared against unstained and respective isotype controls to properly gate samples, as shown. (C-E) MSCs were stained with oil red O (lipids), alcian blue (glycosaminoglycans) and alizarin red S (free calcium) after treatment with adipogenic (C), chondrogenic (D), and osteogenic (E) differentiation stimuli. Images taken at 1, 2, and 3 week time-points, respectively. .....29

Figure 5. mRNA Transcript Levels in TM cells, Measured by RT-qPCR and Normalized Against MSC Transcript Levels. Fold-difference mRNA expression levels in four TM cell strains (TM 120, TM 123, JCT/TM 129, JCT/TM 086 [denoting higher JCT content in donor strains]) relative to the average expression in 3 MSC strains are shown for: (A) TM cell, (B) Schlemm's canal and JCT cell, and (C) MSC markers. Data was first normalized to the geometric mean of three reference markers (GUSB, TATA BP, and YWHAZ) in each sample, as described in the text. Error bars denote standard deviations (n=3 replicates for each strain). .....31

Figure 6. Western Blot Analysis for Dexamethasone Induction of Myocilin in TM Cells and MSCs. (A) Representative western blot against myocilin (red) and total protein (blue) for TM cells and MSC with and without dexamethasone. Molecular weight markers (labeled "ladder" in the figure) are shown in red. (B) Quantification of myocilin expression changes after dexamethasone treatment for four TM cell and three MSC donor strains (n=3 replicates for each strain). The vertical axis is normalized myocilin band intensity after DEX treatment divided by band intensity in control (vehicle-treated) cells. (C)

Average values for TM cells and MSC ($p < 0.002$). Error bars denote standard deviation throughout. .....32

Figure 7. Flow Cytometric Analysis for Dexamethasone Induction of Myocilin in TM Cells Versus MSCs. (A) Representative histograms for myocilin expression in isotype controls (red), untreated cells (blue), and DEX-treated samples (green). (B) Quantification of myocilin expression (median fluorescence intensity) changes after dexamethasone treatment for four TM cell and three MSC donor strains (n=3 replicates for each strain). (C) Average ratio value for TM cells and MSCs ($p < 0.0001$). Error bars denote standard deviation. .....33

Figure 8. Protein-level Characterization of MSCs and TM Cells. Shown are select protein markers for TM cells and MSCs using flow cytometry. Average fluorescent intensity values for TM cells (n=2 donor strains) and MSCs (n=3 donor strains) are shown for four protein markers. Error bars denote standard deviation, and p-values are shown on the plot. .....34

Figure 9. Comparison of TM Cell and MSC contractility. (A) Schematic diagram of collagen gel contraction assay. (B) Average change in collagen gel area relative to initial gel size for TM cells and MSCs during the first seven hours after release from the well. (C) Percent of original gel area for TM cells and MSCs at equilibrium (>8 hours, $p < 0.0005$). Three TM cell and MSC donor strains were used. Error bars denote standard deviation. .....35

Figure 10. Comparison of TM Cell and MSC Phagocytic Activity. (A) Schematic diagram of phagocytic assay and pHrodo particles' fluorescent properties. Using this assay (B), fluorescent intensity from flow cytometry after four hours' incubation is shown for individual TM cell and MSC donor strains. (C) Average values for TM cells and MSCs ($p < 0.0001$). Error bars denote standard deviation. .....36

**Figure 11. AuNS Labeling of MSCs and Resulting PA Properties. (A)** TEM of AuNS showing uniformity and approximate particle size. **(B, C)** Brightfield micrograph of MSCs following AuNS incubation at 2OD for 24 hours. AuNSs are evident (arrowheads) around hematoxylin stained nuclei. **(D - F)** US-PA signal at 700 nm wavelength from gelatin phantoms for **(D)** AuNS only, **(E)** unlabeled MSCs, and **(F)** AuNS-MSCs. In panels D - F, the top row shows US signal only, the middle row shows the PA signal only, and the bottom row shows the merge. In panel D, the faint PA signal was due to trapped air bubbles in the gelatin inclusion, which were also evident by US imaging. **(G)** PA spectra for AuNS-MSCs compared to melanin, thought to be the main endogenous absorber in the porcine eye. .....54

**Figure 12. Spectroscopic Photoacoustic Imaging of AuNS-MSCs Following Delivery to the Anterior Chamber.** Photoacoustic images (color scale) were analyzed before injection, and then immediately, nine, and fifteen minutes after injection (columns left to right). **(A-D)** Shows single PA wavelength imaging at 700nm, while **(E-L)** show

spectroscopic photoacoustic imaging. **(E-H)** Image pixels classified as endogenous absorbers, primarily melanin-containing ocular tissues. **(I-L)** Image pixels classified as AuNS-MSCs. Scale bar= 3mm. .....56

**Figure 13. Ultrasound-Spectroscopic Photoacoustic (US-PA) Imaging Detects AuNS-MSCs Five Hours After Injection.** Overlay of ultrasound (gray) and spectroscopic photoacoustic (color scale) images in single planes **(A-H)**. Each column separates photoacoustic signals according to melanin (left; "background") and AuNS-MSCs (right). Each row corresponds to different concentration of cell injection: **(A,B)** control, no cells, **(C,D)** 250,000 cells , **(E,F)** 500,000 cells, **(G,H)** 1,000,000 cells. 3D views of the anterior segment of each eye were also captured **(I,J)** to better show cell location around the entire TM circumference. **(I)** shows an eye with only vehicle (no cells) injected, while **(J)** shows a 1 million cell injection, both 5 hours after injection. Signal on the posterior sclera was due to signal spillover from regions of high PA signal. Yellow-pink color scale = labeled MSCs. Green-blue color scale = melanin. Scale bar = 3mm .....58

**Figure 14. Spectroscopic PA and Fluorescent Microscopy Images of Labeled MSCs with Additional Processing to Isolate the TM.** Each row shows one representative sample imaged with both modalities, with the top, middle and bottom rows corresponding to injection of 250k, 500k, or 1000k AuNS-MSCs, respectively. Each column depicts, in order from left to right: **(A, F, K)** the fluorescent signal masked to show only the TM region; **(B, G, L)** a filtered heat map version of the fluorescent signal; **(C, H, M)** the corresponding polar histogram; **(D, I, N)** the heat map for PA signal after masking to isolate the TM and filtering; and **(E, J, O)** the corresponding polar histogram. Scale bar= 3mm. .....59

**Figure 15. Comparison between US-PA and fluorescent imaging modalities for AuNS-MSC signal in the TM region. (A – C)** Scatterplots of photoacoustic signal vs. fluorescent signal arising from AuNS-MSCs. Each data point represents the total signal in the entire TM region. Plots show the different cell injection amounts: **(A)** 250k and no cell, **(B)** 500k, 250k, and no cell, and **(C)** 1000k, 500k, 250k, and no cell ($n = 3$ for each group). Significant linear correlations ($p < 0.05$) were observed for each plot as determined by student's t-distribution. .....60

**Figure 16. TEM Characterization of PBNCs.** Representative transmission electron micrographs for **(A)** 20nm PBNCs and **(B)** 200nm PBNCs to determine approximate shape and size. .....70

**Figure 17. Anterior Segment Organ Culture Setup. (A)** Diagram of porcine anterior segment clamped in organ culture dish. Red label indicates TM region. **(B)** Porcine anterior segment in organ culture after 10 days of perfusion. **(C)** Representative outflow facility traces for three porcine eyes. Outflow facility stabilizes after 1-2 days, after which any eyes with outflow facilities outside of the acceptable range are not considered for injection experiments (such as Eye 3). .....73

**Figure 18. Schematics of Ring Magnets.** Overview **(A, B)** and cross-sectional **(C, D)** views for two ring magnet designs used. **(A, C)** Design I: A 3D-printed ring magnet holder housing 10 cylindrical magnets. **(B, D)** Design II: An axially polarized ring magnet. Arrows denote overall magnetic field direction towards the north pole (N). .....75

**Figure 19. Example of Image Processing for *en face* Micrographs. (A)** Raw fluorescent *en face* micrograph showing CFSE-labeled MSCs in green. **(B)** Brightfield *en face* image used for determining the TM location. **(C)** A 1-mm wide ring around the cornea is used to identify CFSE-labeled MSC signal within **(D)** the TM tissue region. **(E)** Fluorescent debris larger than 100µm was excluded and **(F)** polar histograms were created, showing CFSE-labeled MSC signal (radial coordinate, arbitrary units) within the TM as a function of circumferential location. Scale bars denote 2mm.....76

**Figure 20. MSCs Uptake PBNCs. (A-E)** Representative micrographs of MSCs after incubation with different PBNC sizes and PBNC solution optical densities (OD). MSCs were eosin stained to visualize cytoplasm, while PBNCs appear blue. **(F-J)** Photoacoustic signal at 690nm (20nm PBNCs) or 755nm (200nm PBNCs) excitation wavelength for MSCs in gelatin phantoms (both 690nm and 755nm unlabeled MSC signals were minimal so only 690nm is shown). Uptake of PBNCs was further assessed by light side scatter (SSC). **(K,L)** Representative forward scatter (FSC) vs. SSC density maps collected by flow cytometry for **(K)** unlabeled MSCs or **(L)** MSCs incubated in a solution of 200nm PBNCs at a concentration of 2OD. **(M)** Normalized side scatter vs. optical density of incubating solution for 20nm and 200nm PBNC-MSCs (n=3 technical replicates for each). Error bars denote standard deviation.....81

**Figure 21. Magnetic steering of MSCs labelled with either 20 or 200nm PBNCs.** Representative *en face* micrographs of the TM region after MSC delivery. Bar magnets, diagramed in (B) (to scale), were secured overnight at 0$^{o}$ near the limbal region in PBNC-MSC injections. CFSE-tagged MSCs (Green) were injected **(A)** unlabeled, or after incubation with **(B)** 20nm PBNCs at 2 OD **(C)** 20nm PBNCs at 10 OD, **(D)** 200nm PBNCs at 2OD. Scale bars denote 2mm. .....83

**Figure 22. Quantification of Cell Delivery to the TM for MSCs Labelled with 20 and 200nm PBNCs.** Polar histograms illustrate fluorescence intensity (radial coordinate, arbitrary units) for each 30$^{o}$ region. Note that a bar magnet was placed adjacent to the limbus at 0$^{o}$ overnight (see Figure 21B). Average results for **(A)** no magnet, unlabeled MSCs (n=5 eyes), **(B)** 20nm, 2 OD PBNC-MSCs (n=3 eyes), **(C)** 20nm, 10 OD PBNC-MSCs (n=3 eyes), **(D)** 200nm, 2 OD PBNC-MSCs (n=4 eyes) experiments are shown. p-values were calculated using Kuiper's V test to assess if distribution was non-uniformly skewed towards the center of the magnet location (0$^{o}$).....84

**Figure 23. MSCs incubated with 200 nm PBNCs in a solution with OD=2 are steered to the magnet.** The plotted quantity is total fluorescent signal in the TM in the magnet region, defined as the wedge extending from 45$^{o}$ to -45$^{o}$ (see Figure 21B). For box and whisker data, crosses correspond to mean values while the lower, center and

upper limits of the box are the first, second and third quartile. The upper and lower whiskers denote the maximum and minimum values. (Outliers, defined as 1.5x below or above the first and third quartile, respectively, are shown as single data points beyond the upper and lower whiskers when applicable) Significance ($p < 0.05$) was determined by ANOVA, with post hoc Tukey.....85

**Figure 24. Effect of Magnetic Field Exposure on Steering of 200nm PBNC-MSCs to the TM.** Representative *en face* micrographs of the TM region following MSC delivery with bar magnets placed at 0º near the limbal region for different durations (see Figure 21B). All anterior segments were perfused overnight prior to imaging. CFSE-tagged MSCs (Green) were pre-labeled with 200nm PBNCs at a concentration of 2 OD and exposed to a magnetic field for **(A)** 15 minutes, **(B)** 30 minutes, **(C)** 60 minutes, or **(D)** Overnight. Scale bars denote 2mm. .....87

**Figure 25. Quantification of MSC Delivery After Exposure to Magnetic Fields for Different Durations.** Polar histograms illustrate fluorescence intensity (radial coordinate, arbitrary units) for each 30º region, with a bar magnet placed at 0º (see Figure 21B). Average results for **(A)** 15-minutes (n=4 eyes), **(B)** 30-minutes (n=5 eyes), **(C)** 60-minutes (n=3 eyes), and **(D)** overnight (n=4 eyes) magnet exposures are shown. p-values were calculated using Kuiper's V test to assess if distribution was non-uniformly skewed towards the center of the magnet location (0º).....88

**Figure 26. Quantification of Fluorescence within the Quadrant Adjacent to the Magnet. (A)** Percentage of cell signal in the TM within the region 45º to -45º compared to cell signal around the entire TM. **(B)** Fluorescent signal in the TM region relative to the fluorescent signal not in the TM region at the magnet site. Box plot interpretation is as described in Figure 23.....89

**Figure 27. 360º Delivery of PBNC-MSCs Using Ring Magnets.** 200nm labeled PBNC-MSCs were injected into eyes with several types of ring magnets placed around the circumference for different durations. Representative *en face* micrographs of the TM region for **(A)** no magnet, **(B)** Design I for 30 minutes, **(C)** Design II for 15 minutes, and **(D)** Design II for 30 minutes. Scale bars denote 2mm.....90

**Figure 28. Quantification of MSC Delivery in Ring Magnet Experiments.** Polar histograms illustrate MSC fluorescent intensity (radial coordinate, arbitrary units) for each 30º region. Average results for **(A)** control (n=5 eyes), **(B)** Magnet design I for 30 minutes (n=3 eyes), **(C)** Magnet design II for 15 minutes (n=3 eyes), and **(D)** Magnet design II for 30 minutes (n=3 eyes) experiments are shown. p-values were calculated using Rayleigh's test to assess uniform circumferential delivery ($p < 0.05$ denotes non-uniform delivery).....91

**Figure 29. Further Quantification of MSC Delivery in Ring Magnet Experiments. (A)** Total fluorescence signal in the TM around the entire circumference of the eye. **(B)** Fluorescent signal in the TM region relative to the fluorescent signal not in the TM

region. Box plot interpretation is as described in Figure 23. Statistical significance was determined by ANOVA, with post-hoc Tukey. .....92

**Figure 30. Histological Assessment of PBNC-MSC Delivery to the TM.** Representative sagittal sections of the TM region showing fluorescently labeled PBNC-MSCs for **(A,C)** overnight bar magnet exposure and **(B,D)** Design II, 15 minute ring magnet experiments. **(A,B)** Lower magnification brightfield micrographs are labeled with relevant anatomical features for orientation (AAP = angular aqueous plexus, an analogue of Schlemm's canal in porcine eyes). Approximate zoomed regions are shown as blue and red boxes and magnified in panels **(C,D)**.....93

**Figure 31. Cell Viability Results for MSCs labelled with 200nm PBNCs.** Relative viability **(A)** 1 day after 200nm PBNC labeling for 2 MSC donor strains as determined by flow cytometry (n=3 technical replicates for each OD). **(B,C)** Cell counts relative to unlabeled controls for 2 MSC donor strains as determined by quantification of labelled nuclei using fluorescent microscopy following **(B)** 7 days adipogenic differentiation and **(C)** 21 days osteogenic differentiation (n=3 technical replicates for each OD). Error bars denote standard deviation. Asterisks denote significant difference ($p<0.05$) compared to unlabeled controls as determined by ANOVA, with post hoc Tukey. .....95

**Figure 32. Effect of Magnetic Field Exposure on MSC Viability.** Unlabeled and 200nm PBNC-labeled MSCs were incubated on top of cylindrical magnets for 0, 15, 30, 60 minutes or overnight. Magnetic field exposure reduced viability in an exposure-dependent manner. Individual data points for each group are shown with horizontal lines indicating means (n = 3 or 4 technical replicates for each condition). Cell viability within each group (unlabeled or labelled with PBNCs) was statistically different ($p < 0.05$) compared to their respective controls (no magnetic field exposure), as determined by ANOVA post-hoc Tukey. .....96

**Figure 33. Effect of 200nm PBNCs on MSC Adipogenesis. (A-C)** Oil Red O staining for lipids 7 days after adipogenesis treatment in **(A)** 4OD 200nm PBNC-MSCs, **(B)** 1 OD 200nm PBNC-MSCs, and **(C)** unlabeled MSCs. **(D)** Quantification of ratio of fluorescent Nile Red (lipids) to DAPI (nuclei) signal relative to untreated controls for 2 stem cell lines (n=3 technical replicates for each concentration). Error bars denote standard deviation. Asterisks denote significant difference ($p < 0.05$) compared to unlabeled controls as determined by ANOVA, with post hoc Tukey. .....97

**Figure 34. Effect of 200nm PBNCs on MSC Osteogenic Potential. (A-C)** Alizarin Red O staining for free calcium after 21 day osteogenesis treatment in **(A)** 4OD 200nm PBNC-MSCs, **(B)** 1 OD 200nm PBNC-MSCs, and **(C)** unlabeled MSCs. **(D)** Ratios of fluorescent Alizarin Red (free calcium) to DAPI (nuclei) signal relative to untreated controls for 2 stem cells (n=3 technical replicates for each concentration). Error bars denote standard deviation. .....98

Figure 35. pTM Cell Characterization. pTM cells were treated with 200nM DEX for 7 days, and MYOC mRNA levels were assessed by RT-qPCR. MYOC expression is shown relative to untreated controls for each pTM cell isolation. Note that vertical axis is logarithmic. Error bars denote standard deviation (n = 4 technical replicates). Each bar represents one porcine TM cell line. Significant differences ($p<0.05$) between DEX-treated and control samples was found for all samples as determined by ANOVA, with post-hoc Tukey. .....109

Figure 36. Porcine Anterior Chamber Organ Culture Setup. (A) Schematic diagram of porcine anterior segment clamped in organ culture dish. Red region indicates TM. (B) Porcine tissue in organ culture dish after 10 days of media perfusion. (C) Representative outflow facility for three porcine eyes. Pressures typically stabilize after 1-2 days, at which point any eyes outside of the healthy outflow facility range (0.125 to 0.45 µL/min/mmHg) were discarded. .....115

Figure 37. Schematic of 2x Flow Challenge Paradigm. After IOP stabilizes following $H_2O_2$ or media treatment for treated and control eyes, respectively (“Baseline IOP”), inlet flow rate is doubled (“2X Flow Challenge”). In control eyes, we expect the TM to adapt, so that IOP recovers to baseline IOP levels. In treated eyes, TM function is impaired and IOP does not return to baseline values. .....117

Figure 38. Effects of $H_2O_2$ Treatment on pTM Cells *in vitro.* (A) Effect of $H_2O_2$ concentration on pTM cell viability immediately after 1 hour exposure (n = 4 technical replicates). (B) Extended effects of 2mM $H_2O_2$ treatment for 1 hour on pTM cell viability, for two pTM cell lines (n=12 technical replicates). (C) Summary of effects of 1 hour, 2mM $H_2O_2$ treatment on 3 pTM cell lines (n=12 technical replicates). Box plot interpretation is as described in Figure 23. Error bars denote standard deviation. All viability values were normalized to control conditions (no $H_2O_2$). .....121

Figure 39. Effect of $H_2O_2$ on pTM Cell Function. pTM cells were treated with 2mM $H_2O_2$ for 1 hour. After 24 hours, pTM cells were tested for (A) metabolic activity (n=6 technical replicates), (B) phagocytic activity (n=3 technical replicates), and (C) collagen gel contractility (n=6 technical replicates). Black dashed lines denote untreated control results and error bars denote standard deviation. Box plot interpretation is as described in Figure 23. Significant differences (denoted by asterisks, $p < 0.05$) between $H_2O_2$-treated cells and untreated controls was determined by ANOVA, with post-hoc Tukey. .....122

Figure 40. 2x Perfusion Flow Challenge after $H_2O_2$ Treatment. (A) Average IOP traces for $H_2O_2$-treated and control eyes. IOP traces are shown throughout the 2x perfusion flow challenge until IOP steady-state was reached. IOP was normalized to an eye-specific baseline IOP measured after treatment with $H_2O_2$ (experimental eyes) or media (control eyes); shaded region denotes standard error. N values indicate number of eyes that have been averaged, accounting for different termination times for the experiments. (B) Normalized steady-state (~48 hours after H2O2 treatment) IOP after 2x flow

challenge in $H_2O_2$-treated and control eyes (n=9 eyes for each). Box plot interpretation is as described in Figure 23. Significance between $H_2O_2$-treated and untreated eyes was determined by ANOVA, post-hoc Tukey. .....124

Figure 41. Gelatinase Levels in Effluent Collected from Perfused Anterior Segments. (A) Representative zymogram for effluent from control and $H_2O_2$-treated anterior segments. (B) Total gelatinolytic activity is shown relative to pretreatment activity (N > 7 biological replicates for each). 5 µL of sample was run for each time point, and, after quantifying band intensity, 2x flow results were doubled to reflect the increased flow rate. Individual data points are shown and horizontal bars denote means. Significance between $H_2O_2$ treated and untreated eyes was determined by ANOVA, with post-hoc Tukey.....125

Figure 42. Live-dead Staining in $H_2O_2$-treated Porcine Anterior Segments. Representative *en face* images for the entire TM region of (A) control and (B) $H_2O_2$-treated porcine anterior segments. Calcein-AM (Green) and Ethidium homodimer (Red) denote live and dead cells, respectively. Scale bars are 2mm. (C-D) Quantification of Live and Dead fluorescent label intensities in the TM and cornea regions for $H_2O_2$-treated and control anterior segments (n=9 anterior segments each). (C) Live-dead fluorescent signal intensity ratios relative to controls and (D) Live cell signal intensities relative to controls are shown. Box plot interpretation is as described in Figure 23. Significance between $H_2O_2$-treated and untreated eyes was determined by ANOVA, with post-hoc Tukey. .....127

Figure 43. Histological Assessment of TM After $H_2O_2$ Treatment. Representative toluidine blue stained sagittal sections of the TM region for (A,C) $H_2O_2$-treated organ-culture porcine anterior segments and (B,D) untreated control anterior segments. (A,B) Lower magnification brightfield micrographs are labeled with relevant anatomical features for orientation (AAP = angular aqueous plexus, an analogue of Schlemm's canal in porcine eyes). Approximate zoomed regions are shown as blue and red boxes .....129

Figure 44. MSC Delivery to the TM in $H_2O_2$-Treated Anterior Segments. CFSE-labeled MSCs were injected at 1 million cells per anterior segment and allowed to adhere overnight. Representative *en face* fluorescent micrographs for (A) untreated and (B) $H_2O_2$-treated organ culture anterior segments. .....130

# NOMENCLATURE

| | |
|---|---|
| ANOVA | Analysis of variance |
| AU | Arbitrary units |
| AuNS | Gold nanosphere |
| BCA | Bicinchoninic acid |
| CD45, CD73, CD90, CD105 | Cluster of differentiation |
| cDNA | Clonal deoxyribonucleic acid |
| CFSE | Carboxyfluorescein succinimidyl ester |
| CHI3L1 | Chitinase-3-like protein 1 |
| $C_T$ | Cyclic threshold |
| DAPI | 4',6-diamidino-2-phenylindole |
| DEX | Dexamethasone |
| DF | Dilution factor |
| DMEM | Dulbecco's modified Eagle's medium |
| DNA | Deoxyribonucleic acid |
| DTT | Dithiothreitol |
| ECM | Extracellular matrix |
| EDTA | Ethylenediaminetetraacetic acid |
| FACS | Fluorescence activated cell sorting |
| FBS | Fetal bovine serum |
| FSC | Forward scatter |
| GUSB | Beta-glucuronidases |
| HBSS | Hank's balanced salt solution |
| IOP | Intraocular pressure |

iPSC ..... Induced pluripotent stem cell

JCT ..... Juxtacanalicular

LDL Rec ..... Low-Density Lipoprotein Receptor

MFI ..... Median fluorescent intensity

MGP ..... Matrix gla protein

MIP ..... Maximum intensity projection

MMP ..... Matrix metalloproteinase

MSC ..... Mesenchymal stem cell

Muc1 ..... Mucin 1

MYOC ..... Myocilin

OD ..... Optical density

OHT ..... Ocular hypertension

PA ..... Photoacoustic

PBNC ..... Prussian blue nanocube

PBS ..... Phosphate buffered saline

PFA ..... Paraformaldehyde

POAG ..... Primary open angle glaucoma

pTM ..... Porcine trabecular meshwork

PVDF ..... Polyvinylidene fluoride

RIPA ..... Radioimmunoprecipitation assay

RNA ..... Ribonucleic acid

RT-qPCR ..... Reverse transcription quantitative polymerase chain reaction

SDS-PAGE ..... Sodium dodecyl sulfate polyacrylamide gel electrophoresis

sPA ..... Spectroscopic photoacoustic

SPIONS ..... Superparamagnetic iron oxide nanoparticles

SSC ..... Side scatter

TATA BP ..... TATA-binding protein

TEM ..... Transmission electron microscopy

TM ..... Trabecular meshwork

tPA ..... Tissue plasminogen activator

US ..... Ultrasound

UV ..... Ultraviolet

YWHAZ ..... 14-3-3 protein zeta/delta

# SUMMARY

Glaucoma, a leading cause of blindness, affects over 70 million people worldwide, and its incidence is expected to continue to rise with an aging population. The exact pathology underlying primary open angle glaucoma (POAG), the most prevalent form of glaucoma, is unknown, but an increased intraocular pressure (IOP) is a well-established risk factor for POAG. IOP is largely determined by aqueous humor production rate and outflow through drainage tissues in the anterior eye, specifically through the trabecular meshwork. In POAG, the cellularity of the trabecular meshwork (TM) is significantly decreased in comparison to healthy eyes, which presumably leads to loss of TM function, higher outflow resistance and, thus, increased IOP. As a result, therapies striving to restore TM cellularity could alter glaucoma progression. This research will investigate the use of mesenchymal stem cells (MSCs) to restore trabecular meshwork function.

MSC therapies represent a new, largely unstudied, therapeutic approach for the TM, and, as such, methods and procedures for assessing differentiation, delivering cells to the eye, and assessing these cells' therapeutic potential for treating POAG are not yet established. The overall objective of this thesis was to develop solutions to these essential first steps so that MSC therapies can be properly assessed and implemented. We first established methods to characterize differences between MSCs and TM cells at the RNA, protein, and functional levels for assaying MSC differentiation. For studying delivery of MSCs to the eye, we implemented an ultrasound and photoacoustic imaging platform for tracking MSC delivery to the TM in real time. Next, magnetic nanoparticles were used to label and steer MSC to the TM at high efficiency and uniformity compared to passive delivery approaches. Lastly, an improved *ex vivo* model of POAG was

developed to properly mimic glaucomatous changes in the TM triggered by oxidative stress-induced damage.

Overall, this thesis established methods and procedures needed for developing MSC therapies for POAG. Our results allow MSC differentiation to be properly characterized, MSC location to be monitored in real-time in the eye, MSC delivery to be improved with magnetic nanoparticles, and MSC therapeutic benefit to be assessed using a suitable *ex vivo* model. Future work should assess the potential of MSCs for refunctionalizing the TM as a novel POAG therapy.

# CHAPTER 1. INTRODUCTION

## 1.1 Glaucoma

Currently one of the major causes of blindness, glaucoma impacts more than 70 million people worldwide (Cook and Foster, 2012; Quigley and Broman, 2006). This number is expected to continue to rise with an aging population, reaching approximately 80 million by 2020. While there are different types of glaucoma, all are characterized by optic neuropathy associated with structural damage to the optic nerve and subsequent visual dysfunction (Weih et al., 2001). The most common subset of glaucoma is primary open-angle glaucoma (POAG), representing an estimated 74% of glaucoma cases worldwide (Quigley and Broman, 2006). POAG is a chronic condition that leads to irreversible vision loss. While the pathophysiology of POAG is not yet fully understood, an increase in intraocular pressure (IOP) is a well-established risk factor (Weinreb and Khaw, 2004).

## 1.2 Aqueous Humor Dynamics

IOP is primarily controlled by aqueous humor production and drainage from the anterior segment of the eye. Aqueous humor is produced by the ciliary processes and travels from the posterior chamber to the anterior chamber to provide nutrients for the avascular tissues of the anterior eye (Figure 1) (Goel et al., 2010). Aqueous humor production involves three mechanisms: diffusion, ultrafiltration, and active secretion (Gabelt et al., 1995). Diffusion and ultrafiltration are passive processes in which plasma solutes are transported between the capillaries and the posterior chamber due to concentration and osmotic gradients, respectively (Civan and Macknight, 2004). Active

secretion is responsible for as much as 90% of aqueous humor formation (Gabelt et al., 1995). Active transport of serum solutes against a concentration gradient is facilitated by the non-pigmented epithelial cells of the ciliary body through energy-activated protein transporters in their cellular membrane (Goel et al., 2010).

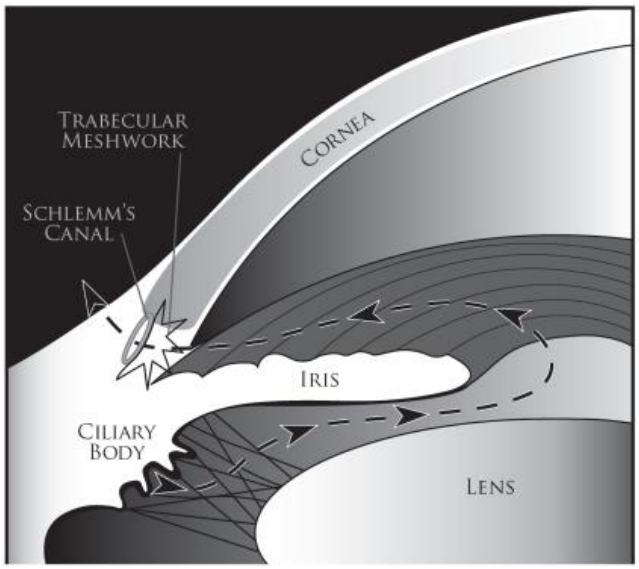


**Figure 1. IOP Regulation in the Anterior Chamber.** Intraocular pressure is determined by the rate of aqueous humor inflow from the ciliary body and by the resistance to outflow of this fluid, primarily through the trabecular meshwork (Goel et al., 2010).

Aqueous humor drainage occurs passively through two pathways located near the anterior chamber angle. The conventional pathway drains through the trabecular meshwork across the inner wall of Schlemm's canal and subsequently into the circulatory system (Goel et al., 2010). In the unconventional pathway (also known as uveoscleral and/or uveovortex outflow), aqueous humor enters the ciliary muscle, passes through the suprachoroidal space, and then either filters across the sclera or is uptaken into choroidal vessels (Bill, 1989; Fautsch and Johnson, 2006). The conventional pathway is generally believed to be the primary source of aqueous humor outflow; however, uveoscleral outflow is difficult to quantify and, while it has been

estimated, its outflow contribution is not fully known (Johnson et al., 2017; Weinreb, 2000).

Production of aqueous humor has been found to be essentially independent of IOP (Acott et al., 2014; Brubaker, 1970, 1991). Further, uveoscleral outflow has been found to be relatively independent of IOP compared to the conventional pathway (Brubaker, 1991). Thus, increased IOP is almost always due to an increase in outflow resistance through the conventional outflow pathway. Conventional outflow resistance is predominantly localized to the trabecular meshwork, accounting for approximately 75% of outflow resistance, suggesting changes to the trabecular meshwork play a key role in IOP elevation seen in glaucoma (Acott and Kelley, 2008; Grant, 1958).

### 1.3 Current Glaucoma Therapeutics

Currently, the primary treatment for POAG is through medication in the form of eyedrops which lower IOP. The most commonly used are prostaglandin analogues, which decrease resistance through the uveoscleral outflow pathway (non-conventional outflow route). Prostaglandin analogues have been associated with intraocular inflammation (Tsai and Kanner, 2005). Alternatively, β-blockers are used to decrease aqueous humor production. Since aqueous humor provides nutrients to anterior segment tissues, lowering production rates could have adverse side effects (Weinreb et al., 2014). Another key drawback for all eyedrop-based therapeutics is the transient nature of changes to IOP, i.e. poor diurnal control of IOP (Weinreb et al., 2014). Transient increases in IOP are hypothesized to lead to glaucoma progression (Asrani et al., 2000). Lastly, daily topical eye drops have poor patient adherence, further increasing transient IOP fluctuations (Gurwitz et al., 1998; Kosoko et al., 1998).

More invasive methods for reducing IOP include laser trabeculoplasty, which damages the TM to stimulate a tissue remodeling response (Barkana and Belkin, 2007), and trabeculectomy filtering surgery, which by-passes the TM by adding new outflow channels (Cairns, 1968; Lee and Higginbotham, 2005). These more invasive methods are associated with high failure rates, need for follow-up operations, and high inflammatory response following surgery (McKinnon et al., 2008; Song et al., 2005). In summary, current therapeutic options are unsatisfactory; thus, novel approaches for IOP control are needed. Since the trabecular meshwork is the tissue predominantly responsible for outflow resistance, this research will focus on trabecular meshwork-based therapies to reduce IOP levels.

## 1.4 Trabecular Meshwork

### *1.4.1 Trabecular Meshwork Structure*

The trabecular meshwork (TM) is located in the iridocorneal angle, the location in the anterior chamber where the iris and cornea meet (Figure 2). Outflow of aqueous humor occurs through the TM's intricate porous structure toward Schlemm's canal (Figure 2). The innermost portion of the TM is called the uveal meshwork; it is composed of beam-like structures containing collagen and elastin fibers, which are covered with a continuous layer of TM cells and their basement membrane (Acott and Kelley, 2008) (Figure 3). The beam-like structures are discontinuous and the uveal meshwork is normally only three beam layers thick in humans, providing a tortuous path for aqueous humor to travel through. Further exterior within the TM, the trabecular beams become thicker with smaller spaces for fluid to travel; this region is known as the corneoscleral meshwork. This denser assortment of beams continues for 8 – 15 layers in humans until the final TM region is reached, namely the juxtacanalicular (JCT) or cribiform region

(Tamm, 2009) (Figure 3). The JCT is adjacent to Schlemm's canal and, unlike the other regions, contains cells embedded in connective tissue as opposed to cell-covered beams (Lutjen-Drecoll, 1999).

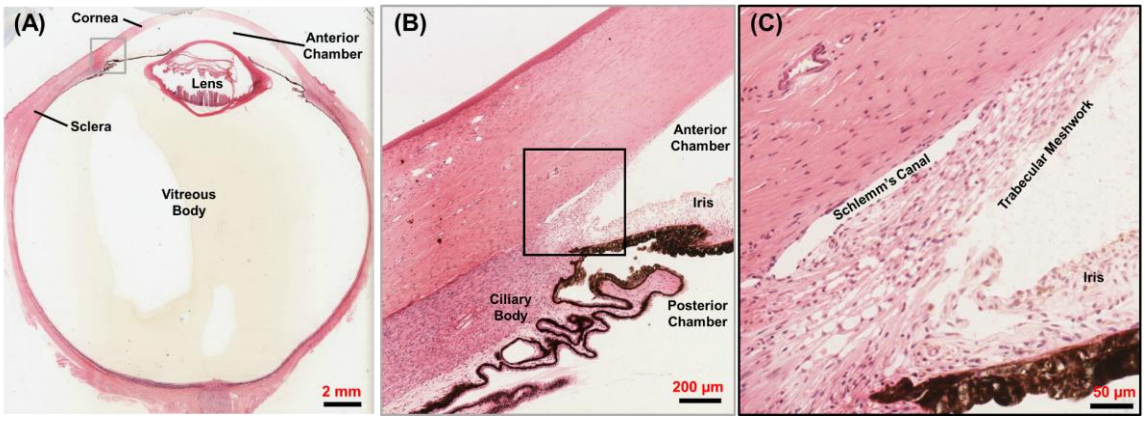


**Figure 2. The Anterior Chamber and Trabecular Meshwork. (A)** The position of the anterior chamber and chamber angle (grey box) in a human eye. **(B)** The chamber angle and TM (black box), and **(C)** further magnified view of the TM and Schlemm's canal. (Kempf et al., 2013).

### *1.4.2 Trabecular Meshwork Tissue Function*

Functionally, the TM is responsible for filtering aqueous humor from the anterior chamber and generating outflow resistance. The innermost uveal and corneoscleral portions of the TM provide little resistance to aqueous humor outflow due to the wide openings between beams (Lutjen-Drecoll, 1999). However, the cells in these inner TM regions are known to be avidly phagocytic (Buller et al., 1990; Johnson et al., 1989; Sherwood and Richardson, 1988). The phagocytic behavior of the inner meshwork is important, since removal of debris and particulates before the aqueous humor reaches the denser, less porous JCT region is thought to prevent plugging of the JCT. The JCT region is where most outflow resistance is believed to be generated. This tissue is thought to experience a rapid, continuous extracellular matrix turnover which may play a role in modulating outflow facility (Keller and Acott, 2013).

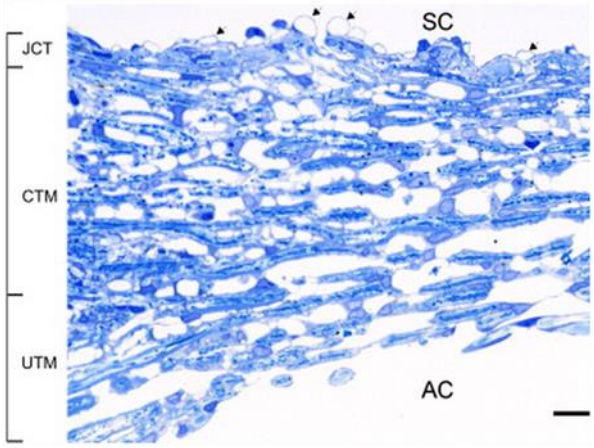


**Figure 3. Trabecular Meshwork Microstructure.** The three different regions of the TM. The direction of aqueous humor flow is from bottom to top in the above micrograph. SC denotes Schlemm's canal, JCT denotes juxtacanalicular tissue, CTM denotes cornealscleral TM, UTM denotes uveal TM, and AC denotes the anterior chamber (Tamm, 2009).

While the human TM is continuous around the anterior chamber circumference, aqueous humor outflow has been found to be non-uniform or segmental (Swaminathan et al., 2014). Studies indicate that as little as one-third of the TM may be actively filtering at any one time (Chang et al., 2014). The cause for segmental outflow is still unknown but evidence suggests extracellular matrix composition in the JCT, location of collector channels, and pores in Schlemm's canal inner wall play a role (Battista et al., 2008; Johnson et al., 1992; Keller et al., 2011; Lu et al., 2011; Overby et al., 2002). Further, active filtering regions are altered at physiological pressure (15mmHg) compared to lower IOP (9mmHg) in human eyes, suggesting segmental outflow is pressure-dependent (de Kater et al., 1989; Hann et al., 2005). Finally, the extent of segmental outflow is greater in glaucoma patients than in normals (de Kater et al., 1989).

### *1.4.3 Trabecular Meshwork Cells*

Although the JCT and inner-TM regions are functionally unique, the resident cells are derived from neural crest mesenchymal stem cells during gestation (Abu-Hassan et

al., 2014a; Stamer and Clark, 2017; Tripathi and Tripathi, 1989). The inner TM cells of the uveal and corneoscleral regions are morphologically endothelial-like but have macrophage-like activity to phagocytose debris and pigment (Stamer and Clark, 2017). This phagocytic function has been observed *in vivo* as well as in isolated, cultured cells (Johnson et al., 1989). Inner-TM cells also play a role in maintaining openings in the TM beam structures by secreting anti-thrombotic factors such as tissue plasminogen activator, similar to an endothelial phenotype (Shuman et al., 1988).

The outer-TM cells, primarily in the JCT region, are morphologically similar to fibroblasts. These cells secrete extracellular matrix and degradation enzymes essential for tissue remodeling at rates similar to fibroblasts found in sites of wound repair (Keller et al., 2009). In addition, the TM cells, primarily in the JCT and corneoscleral regions, have contractile properties similar to smooth muscle cells (Dismuke et al., 2014a; Stamer and Clark, 2017; Stumpff and Wiederholt, 2000). Alterations to the tissue permeability, and, thus, outflow resistance, are related to the cells' contractile capabilities (Llobet et al., 2003).

### *1.4.4 Trabecular Meshwork During Glaucoma*

Studies have assessed structural and functional changes to the TM that may explain the increased outflow resistance and subsequent elevated IOP observed in glaucoma. The cellularity of the TM as a whole has been shown to significantly decrease with age, with up to 60% loss by age 80 (Alvarado et al., 1981; Grierson and Howes, 1987). An even greater decrease in cellularity (approximately an additional 30%) has been noted in glaucomatous eyes compared to age-matched eyes (Alvarado et al., 1984; Liton et al., 2005). The reason for this reduced cell count in glaucoma is not known, but oxidative or mechanical stress may play a role (Abu-Hassan et al., 2014a).

These cellularity changes presumably have important ramifications for the tissue as a whole. Other changes to the TM have also been observed in glaucoma. For example, the extracellular matrix (ECM) of the TM thickens in glaucoma, indicating abnormal ECM maintenance (Tektas and Lutjen-Drecoll, 2009).

### 1.5 Regenerative Medicine Therapies

Due to cell loss in the trabecular meshwork, regenerative medicine approaches could be beneficial for treating the TM in glaucoma. Regenerative medicine is a therapeutic approach that aims to “replace or regenerate human cells, tissue, or organs to restore or establish normal function” (Mason and Dunnill, 2008). One of the primary ways regenerative medicine is implemented is through the use of stem cells, a subset of cells that are capable of self-renewal and differentiation to different mature cell types (Bianco et al., 2001; Kern et al., 2006; Loeffler and Roeder, 2002). Stem cell populations with different regenerative capacities have been isolated from both embryonic and adult tissues. Based on the origin, the cells’ regenerative potential ranges from the ability to differentiate into all adult cell types (pluripotent), to only a limited subset of cell types (multipotent). Depending on the regenerative medicine application, the greater differentiation potential of pluripotent stem cells may be desirable; however, undifferentiated pluripotent stem cells have been found to form teratomas *in vivo* due to uncontrolled proliferation and differentiation (Fong et al., 2010; Hanna et al., 2010). Such issues are much less likely when using multipotent stem cell sources, but their lower differentiation potential can impose practical limitations. Due to this, rational selection of a suitable stem cell population needs to be made for each application.

## 1.6 Stem Cell therapies for the Trabecular Meshwork

Stem cell therapies for the TM, to date, have focused on three different classes of stem cells: native TM stem cells, induced pluripotent stem cells, and mesenchymal stem cells.

### *1.6.1 Native TM Stem Cells*

A fourth region in the TM, called the insert zone, is located at Schwalbe's line and is not involved in aqueous humor outflow per se (Raviola, 1982). A multipotent stem cell-like population has been isolated from this region and characterized (Tay et al., 2012). These cells, termed TM stem cells or "insert" cells, are believed to play a key role in maintaining proper cellularity of the TM as evidenced by laser trabeculoplasty experiments showing the majority of TM regeneration occurs in this insert zone (Acott et al., 1989). As a result, this cell population is an obvious source for regenerative medicine therapies for the glaucomatous TM.

Du *et al*. isolated multipotent TM stem cells from human eyes and assessed whether differentiation to a TM-like phenotype was possible (Du et al., 2012). TM stem cells were treated with bovine aqueous humor or fetal bovine serum for 10 days to induce differentiation, at which point cells were assayed for TM-like properties. Increased phagocytic activity was observed after both aqueous humor and fetal bovine serum treatment, mimicking primary human TM cell activity. Further messenger-level changes were detected that were consistent with a TM phenotype. However, since fetal bovine serum, a commonly used stem cell media reagent, induced differentiation, TM stem cells may be biased toward a TM phenotype (Bieback et al., 2009). Thus, while TM stem cells can be successfully differentiated into functional TM cells, the stimulus used to differentiate them is unlikely to translate to other stem cell types.

A significant drawback to clinical use of therapies based on TM stem cells is the reduced cellularity of the glaucomatous TM, strongly suggesting that the insert region TM stem cells are too depleted or otherwise somehow unable to repopulate the TM. An alternative strategy is to use allogeneic TM stem cells. The TM is immune privileged due to the anterior chamber being avascular and aqueous humor containing immunosuppressants (Niederkorn, 2002; Treacy et al., 2016). However, corneal transplant allografts still suffer from more than 40% rejection rates, suggesting issues with allogeneic cell therapies (Sellami et al., 2007). Further, harvesting allogenic TM stem cells would be extremely challenging and likely infeasible in a clinical setting.

### *1.6.2 Induced Pluripotent Stem Cells*

Alternatively, induced pluripotent stem cells (iPSCs) have been investigated, since they can be created autologously, thus overcoming immune rejection issues. iPSCs were developed by Nobel laureate Shinya Yamanaka by reprogramming fibroblasts through retroviral transduction of 4 genes (Oct3/4, Sox2, c-Myc, and Klf4, also known as the “Yamanaka factors”) to an embryonic-like, pluripotent stem cell phenotype (Takahashi et al., 2007; Takahashi and Yamanaka, 2006).

iPSCs have been differentiated to a phagocytic TM-like phenotype by co-culture with primary TM cells for 21 days (Ding et al., 2014). TM-like iPSCs were able to restore IOP homeostasis in a human organ culture model of glaucoma, demonstrating proof-of-concept for restoring cellularity of the damaged TM (Abu-Hassan et al., 2014b). To induce reduced TM cellularity, saponin, a plant-derived detergent, was perfused into the eye to kill approximately 30 to 40% of TM cells. While the desired reduction in cell numbers was achieved, characterization of the effects of saponin on anterior segment tissues or its effect on the remaining TM cells was not carried out.

Conversely, Zhu *et al*. used a more conventional transgenic mutant myocilin model of glaucoma that leads to endoplasmic reticulum stress and subsequent TM cell death (Zhu et al., 2016b; Zode et al., 2011). TM-like iPSCs injected into the mouse eyes reduced IOP 6 weeks after injection, indicating TM-like iPSCs restored TM function. However, histology revealed that restoration of cellularity was due to increased proliferation of native TM cells rather than integration of TM-like iPSCs into the meshwork. While some TM-like iPSCs remained in the TM after 12 weeks, many more were in off-target tissues such as the cornea (Zhu et al., 2016b). This suggest that the driving factor for TM regeneration was paracrine signaling as opposed to direct repopulation of the TM by TM-like iPSCs.

Summarizing the above, iPSC-derived TM-like cells have been shown to reduce IOP after introduction into the eye in two different glaucoma models. However, this effect may be due to increasing native TM cell proliferation. While these results are promising, iPSC-based approaches may not be suitable for clinical treatment of glaucoma patients, since aged tissue is known to have reduced proliferative ability, a situation that is exacerbated in many disease states. Thus, proliferation of the remaining native TM cells in POAG may be muted or inadequate to restore TM function (Barbero et al., 2004; McCarron et al., 1987). iPSC-based therapies also suffer from practical limitations, e.g. iPSC reprogramming is complex and costly. In addition, iPSCs carry the risk of teratoma formation *in vivo*. These issues impose economic and regulatory hurdles towards eventual clinical translation.

### *1.6.3 Mesenchymal Stem Cells*

Alternatively, mesenchymal stem cells (MSCs) are being investigated to restore TM function. MSCs are multipotent stem cells found in many tissues, e.g. adipose and

bone marrow tissues (Kern et al., 2006; Zuk et al., 2002). MSCs are easily isolated without lengthy reprogramming or purification processes, as for iPSCs. Furthermore, they are already routinely used in clinical application. Based on developmental biology studies, trabecular meshwork tissue is believed to be derived from mesenchymal stem cells, suggesting mesenchymal-based therapies may be able to restore TM function (Cvekl and Tamm, 2004; Gould et al., 2004; Reme and d'Epinay, 1981; Sowden, 2007). Two studies to date have investigated MSC therapies for the TM. MSC differentiation into functional TM cells was not the focus of these studies. Instead, each study looked at MSC paracrine signaling, since paracrine signaling has been shown to play a prevalent role in promoting proliferation and tissue function (Gnecchi et al., 2008). First, Manuguerra-Gagne *et al.* injected bone marrow-derived MSCs into a laser-induced model of glaucoma in rats (Manuguerra-Gagne et al., 2013). IOP was reduced over the course of 20 days following MSC injection, however, stem cells could not be detected in the TM after only 4 days. IOP reduction was believed to be due to increased proliferation of native TM cells, similar to the situation with TM-like iPSCs (Zhu et al., 2016b).

Roubeix *et al*. demonstrated IOP reduction in an episcleral vein cauterization rat model of glaucoma following injection of bone marrow derived MSCs (Roubeix et al., 2015). IOP reduction occurred immediately following delivery, but was not sustained, with IOP increasing again after 15 days. Conversely, stem cells were detectable for at least 23 days in the TM as well as off-target sites such as the cornea and ciliary processes.

These two studies suggest that MSCs may be suitable for TM regenerative medicine therapies. Each study successfully delivered some MSCs to the TM, but delivery needs to be further investigated due to conflicting results about stem cell retention in the TM. Significant off-target delivery (i.e. cell delivery to tissues other than

the TM) was evident in these studies, which could lead to vision-related issues if undesired phenotypic differentiation occurred in other ocular locations, such as the cornea and lens.

Lastly, the models used for studying MSC delivery were not ideal for the intended application. The laser-induced ocular hypertension model involves applying laser irradiation to the TM, which damages the TM and thereby impedes aqueous outflow to raise IOP. This approach is suitable for inducing optic neuropathy and studying optic nerve head pathophysiology in glaucoma (Levkovitch-Verbin et al., 2002), but is entirely unlike the mode of TM damage that occurs in human glaucoma. Loss of intertrabecular spaces and trabecular beam contraction are consistently observed in this model, and may affect MSC delivery (Levkovitch-Verbin et al., 2002). Alternatively, the episcleral vein cauterization model induces elevated IOP by cauterizing multiple episcleral veins to block Schlemm's canal outflow (Shareef et al., 1995). Again, this is unlike what occurs in human glaucoma. Further, since the site of increased outflow resistance is downstream of the TM in this model, it is an inappropriate model for testing strategies to regenerate the TM.

In summary, MSCs represent a promising cell source for trabecular meshwork regeneration; however, to date, few studies have been done with these cells. Additional tools are needed to detect differentiation of MSCs to TM-like cells, monitor MSC dynamics after injection, improve stem cell delivery to the TM, and properly assess TM regeneration in a suitable glaucoma model. This thesis seeks to address these shortcomings so that MSC therapies targeting the glaucomatous TM can be developed.

# CHAPTER 2. SPECIFIC AIMS

Due to reduced cellularity in the trabecular meshwork (TM), with concomitant loss of functionality during glaucoma, stem cells may offer a novel therapeutic route to treat patients with ocular hypertension in glaucoma. Mesenchymal stem cells (MSCs) are of particular interest since they can be obtained autologously from adipose tissue and can be utilized without lengthy differentiation and purification protocols prior to delivery. However, to date, few studies have investigated using MSCs for repairing the TM. Many questions regarding characterizing differentiation, cell delivery to the TM, and assessing the therapeutic benefit of mesenchymal stem cells have yet to be addressed. This thesis seeks to address these current shortcomings so that MSC therapies targeting the glaucomatous TM can be developed.

**Specific Aim 1:** Characterize differences between mesenchymal stem cells and trabecular meshwork cells at the RNA, protein, and functional levels

Before differentiation of MSCs to a TM phenotype is possible, methods for confirming differentiation are needed. Human adipose-derived MSCs were compared to human TM cells to detect differences between the two phenotypes at the messenger RNA (RT-qPCR), protein (western blotting, flow cytometry), and functional (phagocytosis, gel contractility) levels. Each method was optimized for detecting differences and assessing proper TM cell function. As a result, these methods can be utilized to fully define whether MSCs have differentiated to a functional TM-like phenotype.

**Specific Aim 2:** Implement an ultrasound-photoacoustic imaging protocol for visualizing mesenchymal stem cell delivery and retention in the trabecular meshwork

Stem cell delivery to any tissue requires optimization and troubleshooting to improve delivery efficiency while minimizing unwanted delivery to “off-target” tissues. To help optimize cell delivery to the TM, an ultrasound-photoacoustic imaging platform was utilized. Ultrasound imaging was able to identify key anatomical landmarks in the porcine anterior segment. MSCs were labeled with gold nanospheres so that cells could be photoacoustically identified and separated from background signal. With this platform, MSCs could be non-invasively tracked during anterior chamber injection and cell delivery into the TM.

**Specific Aim 3:** Improve mesenchymal stem cell delivery to the trabecular meshwork using magnetic nanoparticles

Aqueous humor outflow through the TM is slow and highly segmental, which is problematic for MSC delivery since many cells injected into the anterior chamber tend to settle on the anterior iris and lens, while those cells that reach the TM tend to accumulate in regions of high flow, which may not be optimal for treating glaucoma. Thus, to enhance delivery, MSCs were labeled with magnetic nanoparticles (Prussian blue nanocubes [PBNCs]). After injection into the anterior chamber, labelled MSCs could be efficiently steered to the TM by a magnetic field in as little as 15 minutes. Further, with a suitable magnetic field, MSCs could be steered to the entire TM circumference, largely overcoming segmental fluid outflow that impacts conventional MSC delivery. Magnetic steering of MSCs thus improves delivery efficiency and distribution to the TM, which may be essential for development of optimal glaucoma therapies.

**Specific Aim 4:** Development of a Porcine Organ-Culture Glaucoma Model Mimicking Trabecular Meshwork Damage

Current glaucoma models are primarily focused on creating ocular hypertension to induce optic neuropathy, with little fidelity to the clinical pathology that occurs in the TM of glaucoma patients. Notably, reduced TM cellularity as seen in glaucoma is not a feature of most such models. Instead, existing models permanently damage or clog the outflow region, which is not suitable for assessing stem cell therapies to repair the TM. Here, we develop a porcine anterior segment organ-culture model using hydrogen peroxide to induce oxidative stress in the TM and thus partially decellularize the TM. Following hydrogen peroxide treatment, eyes were challenged with increased fluid flow to assess the TM's ability to homeostatically maintain IOP. In response to this challenge, control eyes were able to increase outflow through the TM via MMP-mediated remodeling, while hydrogen peroxide-treated eyes were not able to do so. Further, live-dead staining and histology confirmed reduced TM cellularity in treated eyes without extensive structural damage to the TM, similar to the situation in human glaucoma. As a result, this glaucoma model is suitable to assess the use of MSC-based therapies for restoring function to the TM.

# CHAPTER 3. Characterize Differences Between Mesenchymal Stem Cells and Trabecular Meshwork Cells at RNA, Protein, and Functional Levels

This chapter is adapted from an article published in the Journal of Tissue Engineering and Regenerative Medicine:

Snider, E.J., Taylor Vannatta, R., Schildmeyer, L., Stamer, W.D., and Ethier, C.R. (2017). Characterizing differences between MSCs and TM cells: Towards autologous stem cell therapies for the glaucomatous trabecular meshwork. J Tissue Eng Regen Med. 2017; 1-10. https://doi.org/10.1002/term.2488.

---

## 3.1 Abstract

Glaucoma, a leading cause of blindness, is characterized by an increase in intraocular pressure (IOP), which is largely determined by resistance to aqueous humor outflow through the trabecular meshwork (TM). In glaucoma, the cellularity of the TM is decreased, and, as a result, stem cell therapies for the TM represent a potential therapeutic option for restoring TM function and treating glaucoma patients. We here focus on adipose derived mesenchymal stem cells (MSCs) as a potential autologous cell source for TM regenerative medicine applications and describe characterization techniques at the messenger (RT-qPCR), protein (western blotting, flow cytometry), and functional (contractility, phagocytosis) levels to distinguish MSCs from TM cells. We present a panel of 12 transcripts to allow: (i) suitable normalization of RT-qPCR results across cell types and after exposure to potential differentiation stimuli; (ii) distinguishing

MSCs from TM cells; (iii) distinguishing subtypes of TM cells; and (iv) distinguishing TM cells from those in neighboring tissue. At the protein level, dexamethasone-induction of myocilin was a robust discriminating factor between MSCs and TM cells, and was complemented by other protein markers. Finally, we show that contractility and phagocytosis differ between MSCs and TM cells. These methods are recommended for use in future differentiation studies to fully define if a functional TM-like phenotype is being achieved.

## 3.2 Introduction

Glaucoma, a leading cause of blindness, affects over 70 million people worldwide. Its incidence is expected to continue to rise with an aging population (Cook and Foster, 2012; Quigley and Broman, 2006). An increased intraocular pressure (IOP) is a well-established risk factor for glaucoma (Weinreb and Khaw, 2004), and is the only treatable risk factor at present. IOP is largely determined by aqueous humor production rate and outflow through drainage tissues in the anterior eye. Aqueous humor leaves the eye primarily through the trabecular meshwork before entering Schlemm's canal and subsequently the circulatory system (Goel et al., 2010).

The trabecular meshwork (TM), including the inner wall of Schlemm's canal, is known to be the major site of aqueous outflow resistance, and changes in this tissue lead to elevated IOP. Further, alterations to outflow resistance are thought to be related to TM cells' contractile capabilities (Llobet et al., 2003). Additionally, the TM removes debris from aqueous humor by phagocytosis (Buller et al., 1990; Sherwood and Richardson, 1988) to avoid outflow blockage; thus, phagocytosis and contraction are two important functional properties of the TM. Structurally, the TM has three main regions that differ in outflow resistance, with the inner uveal and corneoscleral regions providing

little outflow resistance (Grant, 1963; Tamm, 2009) yet high phagocytic activity (Acott and Kelley, 2008), while the outermost juxtacanalicular tissue (JCT) provides much higher outflow resistance due to its low porosity (Johnson, 2006; Keller et al., 2009).

In glaucoma, the cellularity of the entire trabecular meshwork has been shown to be significantly decreased in comparison to age-matched healthy eyes (Alvarado et al., 1984; Baleriola et al., 2008; Gonzalez et al., 2006; Liton et al., 2005). This loss of cells presumably leads to loss of function in the trabecular meshwork, contributing to higher outflow resistance and, thus, increased intraocular pressure. Evidence supporting this hypothesis was recently demonstrated by Abu-Hassan *et al*. who reduced cellularity of the trabecular meshwork in human eyes maintained in organ-culture, which led to a loss of IOP homeostasis (Abu-Hassan et al., 2015). Thus, therapies seeking to restore the cellularity and function of the trabecular meshwork could potentially have therapeutic benefit for glaucoma patients.

Several studies have investigated the use of fibroblast-derived induced pluripotent stem cells (iPSCs) to create TM-like cells to repopulate the TM (Abu-Hassan et al., 2015; Ding et al., 2014) . However, iPSCs technology is complex and costly and poses challenging regulatory hurdles to bring these therapies into practice (Fong et al., 2010; Neofytou et al., 2015; Reisman and Adams, 2014). Here we consider the alternative approach of using adult-derived mesenchymal stem cells (MSCs). While MSCs are found in many adult tissues (e.g. adipose tissue) and are commonly used in clinical settings with fewer regulatory hurdles than iPSCs, MSCs have less differentiation potential than iPSCs. Fortunately, the trabecular meshwork appears to be derived from mesenchymal stem cells, suggesting MSCs may be capable of reaching a TM lineage (Cvekl and Tamm, 2004; Reme and d'Epinay, 1981). Furthermore, preliminary efforts

have shown evidence that MSCs are capable of differentiating to a TM-like phenotype (Snider et al., 2016; Zhou et al., 2015).

TM cells have been compared to an MSC phenotype previously to determine if TM cells possess stem cell-like characteristics (Morgan et al., 2014). In contrast, for MSC-based regenerative therapies for the trabecular meshwork characterization methods to thoroughly describe the TM phenotype and distinguish undifferentiated MSCs and TM cells are required. TM cells have previously been characterized by their RNA and protein expression profile as well as unique functional attributes; and these characteristics will be used for comparison against MSCs. The ideal characterization methods should: (i) easily and quantitatively distinguish MSCs from TM cells, (ii) be consistent with common methodologies used to characterize TM cells currently, (iii) be relatively high-throughput, and (iv) assess functional outcomes. We here describe a set of characterization assays that meet these criteria.

## 3.3 Materials and Methods

### *3.3.1 Mesenchymal Stem Cell Sourcing and Characterization*

Human adipose derived MSCs (Lonza) were grown in α-minimum essential medium supplemented with 20% fetal bovine serum (FBS), penicillin, streptomycin, and L-glutamine. At 80-90% confluency, MSCs were detached using 0.05% Trypsin/EDTA (w/v) and seeded in fresh cell-culture T75 flasks at a seeding density of 5,000 cells/cm$^2$. In all experiments, MSCs were used at passage numbers five or six. Each MSC donor strain was validated by Lonza for expression of MSC surface markers (CD13, CD29, CD44, CD73, CD90, CD105, and CD166) and minimal expression of negative MSC markers (CD14, CD 131, CD45).

After MSC expansion, stem cells were further characterized two ways. First, each MSC donor strain was exposed to adipogenic, chondrogenic, and osteogenic medium (Life Technologies) for 1, 2, and 3 weeks respectively to test trilineage potential. All samples were fixed at respective time points and stained with Oil Red O (lipids, adipogenic), Alcian Blue (glycosaminoglycans, chondrogenic), and Alizarin Red (calcium, osteogenic), respectively. Each donor strain was also characterized for a known MSC surface marker (CD90) and negative MSC marker (CD45) using flow cytometry (Chamberlain et al., 2007) after resuspending cells in fluorescently conjugated CD90/CD45 or respective isotype solutions for 30 minutes (R&D Systems). Flow cytometry, using an LSR II (BD Biosciences), was performed until at least 10,000 cellular events were recorded for stained, isotype and unstained controls. To quantify flow cytometry data, positive gates were configured on histogram plots so that less than 0.5% of isotype fluorescence gated positively. Stained samples were compared using the same gate configuration to determine the percentage of cells showing a shift in fluorescent intensity, indicating surface marker expression.

### *3.3.2 Trabecular Meshwork Cell Sourcing and Characterization*

Human trabecular meshwork (TM) cells were isolated as previously described (Stamer et al., 1995), and grown in Dulbecco's Modified Eagle Medium (DMEM, 1g/L glucose) with 10% FBS, penicillin, streptomycin, and L-glutamine. At approximately 80-90% confluency, TM cells were detached with 0.05% trypsin/EDTA and seeded onto fresh T75 flasks at 5,000 cells/cm$^2$. TM cells were characterized as previously described through morphological assessment, contact inhibition, and dexamethasone induction of myocilin (Clark et al., 2001; Stamer et al., 2000; Stamer et al., 1995), and used in experiments at passage number five to seven. Based on morphological assessment, TM

cell donor strains with high JCT-like cell content were denoted as JCT/TM cells instead of TM cells, which were more uveal/corneoscleral-like.

### *3.3.3 Reverse Transcription Quantitative PCR (RT-qPCR)*

RNA was isolated from cells using TRIzol reagent (Life Technologies) and further purified using Aurum Total RNA Mini Kit per the manufacturer's protocol (Bio-Rad). RNA concentration and purity were determined using a Nanodrop 2000C spectrophotometer (Thermo-Scientific). Reverse transcription to clonal DNA (cDNA) was performed on 1µg RNA samples per the manufacturer's protocol (Bio-Rad). cDNA samples were analyzed against a panel of twelve primer pairs (Table 1) (Du et al., 2012; Spandidos et al., 2008; Spandidos et al., 2010; Wang and Seed, 2003; Ye et al., 2012). SYBR green reagent (Quantabio) was used to quantify DNA amplification in real time throughout the PCR cycle (StepOnePlus Real Time PCR System, Applied Biosystems). The resulting cyclic threshold ($C_T$) values were normalized to the geometric mean of three reference genes (*GUSB*, *YWHAZ*, and *TATA BP*; see below) and further normalized against untreated MSC samples using the $2^{-\Delta\Delta CT}$ methodology (Livak and Schmittgen, 2001).

**Table 1. Primer Sequences Used in RT-qPCR Experiments**. Primers are organized based on different categories (e.g. reference, TM cell marker). Primers were selected from indicated references or designed using Primer-Blast when indicated. Sequences selected from PrimerBank database show corresponding PrimerBank IDs.

| Primer Name | | Category | Primer Sequence (5' to 3') | Reference |
|---|---|---|---|---|
| Beta-Glucuronidase (*GUSB*) | Forward | Reference/ Housekeeping Markers | GTCTGCGGCATTTTGTCGG | Custom Primer-BLAST [36 |
| | Reverse | | CACACGATGGCATAGGAATGG | |
| TATA Binding Protein | Forward | | CCACTCACAGACTCTCACAAC | PrimerBank [37-39 285026518c1 |
| | Reverse | | CTGCGGTACAATCCCAGAACT | |
| Tyrosine 3/tryptophan 5-monoxygenase activation protein (*YWHAZ*) | Forward | | CCTGCATGAAGTCTGTAACTGAG | PrimerBank 208973243c1 |
| | Reverse | | GACCTACGGGCTCCTACAACA | |
| Alpha-B Crystallin | Forward | Schlemm's Canal Marker | CCTGAGTCCCTTCTACCTTCG | PrimerBank 4503056c1 |
| | Reverse | | CACATCTCCCAACACCTTAACTT | |
| VE-Cadherin | Forward | Juxtacanalicular Marker | AAGCGTGAGTCGCAAGAATG | PrimerBank 166362712c2 |
| | Reverse | | TCTCCAGGTTTTCGCCAGTG | |
| Tissue Plasminogen Activator (*tPA*) | Forward | TM Cell Markers | AGCGAGCCAAGGTGTTTCAA | PrimerBank 132626665c1 |
| | Reverse | | CTTCCCAGCAAATCCTTCGGG | |
| LDL Receptor (*LDL*) | Forward | | ACGGCGTCTCTTCCTATGACA | PrimerBank 307775415c3 |
| | Reverse | | CCCTTGGTATCCGCAACAGA | |
| Chitinase 3-Like 1 (*CHI3L1*) | Forward | | CCTTGACCGCTTCCTCTGTA | Du *et al*, 2012 |
| | Reverse | | GTGTTGAGCATGCCGTAGAG | |
| Matrix GLA Protein (*MGP*) | Forward | | GCCGCCTTAGCGGTAGTAAC | Du *et al*, 2012 |
| | Reverse | | TCTCTGCTGAGGGGATATGA | |
| Myocilin (*MYOC*) | Forward | | AAGCCCACCTACCCCTACAC | Du *et al*, 2012 |
| | Reverse | | TCCAGTGGCCTAGGCAGTAT | |
| Mucin 1 (*Muc1*) | Forward | MSC Markers | CCATTCCACTCCACTCAGGT | Du *et al*, 2012 |
| | Reverse | | CCACATGAGCTTCCACACAC | |
| CD105 | Forward | | TGCACTTGGCCTACAATTCCA | PrimerBank 168693646c1 |
| | Reverse | | AGCTGCCCACTCAAGGATCT | |

### *3.3.4 Dexamethasone Induction of Myocilin*

Isolated TM cells are commonly characterized by measuring the upregulation of myocilin protein following dexamethasone (DEX) treatment (Stamer et al., 2000; Stamer et al., 1995). Compared to other ocular cells, TM cells uniquely, and dramatically upregulate myocilin (MYOC) in response to glucocorticoid treatment (Clark et al., 2001). Thus, the same methodology was applied to characterize MSCs as they differentiated into TM cells. Cells were treated with 100nM DEX (Sigma) in media for 7 days, changing media every three days. Additional control cells remained untreated for 7 days with similar feeding regimen. MYOC levels were detected in two ways: by western blotting and by flow cytometry.

### *3.3.5 Western Blotting*

Protein was isolated from cell monolayers using ice-cold RIPA buffer supplemented with Halt™ Protease Inhibitor Cocktail (Thermo-Scientific) after washing with PBS to remove media protein. Isolated protein was then quantified by micro bicinchoninic acid assay (BCA) per the manufacturer's protocol (Thermo-Scientific). Samples were diluted and 4x Laemmli Sample Buffer (Bio-Rad) with 50µM Dithioethriol (DTT) was added so that protein concentrations were equal across all samples (20µg/sample). To denature proteins, samples were heated at 95$^{o}$C for 5 minutes. Finally, samples were added to Protean-TGX stain-free 8-16% polyacrylamide gels (Bio-Rad) for SDS-PAGE at 150V, 45 minutes.

Following SDS-PAGE, gels were placed on a UV transilluminator plate for 10 minutes to activate the stain-free total protein gel indicator. Stain-free gels contain trihalo compounds which bind to tryptophan residues through a UV-catalyzed reaction, leaving a fluorescent signal where protein exists in the gel (Ladner et al., 2004). After incubation, samples were imaged with an Amersham Imager 600 scanner (GE Healthcare) to confirm total protein staining. Next, gel proteins were transferred to a polyvinyl difluoride (PVDF) membrane using a Trans-blot Turbo Transfer system (Bio-Rad; 3 minutes, 25V). Membranes were blocked in Odyssey® TBS Blocking Solution (LI-COR Biosciences) for 1 hour at room temperature and incubated with MYOC primary antibody (Santa-Cruz Biotechnology N-15, 1:2000 dilution factor [DF] in blocking solution) overnight, 4$^{o}$C. After washing with TBS-Tween20, AlexaFluor 680 conjugated secondary antibody (1:10000 DF) was added for 1 hour at room temperature. Blots were imaged with an Amersham Imager 600 scanner for MYOC labelling and total protein fluorescence. MYOC levels were normalized to the total protein stain using ImageQuant software (GE Healthcare).

### *3.3.6 Flow Cytometry*

#### 3.3.6.1 Intracellular Marker Approach

Adherent cells were detached from tissue-culture plastic using 0.05% Trypsin/EDTA after washing off residual media with PBS. After 5 minute (37ºC) incubation, Trypsin was neutralized and cell samples were collected, centrifuged, and resuspended in 1% paraformaldehyde (PFA) for 10 minutes. Subsequently, samples were washed with FACS buffer (PBS supplemented with 5% FBS and 0.02% Sodium Azide) and resuspended in 100µL antibody solution (antibody information provided in Table 2) containing 0.5% saponin FACS buffer for 30 minutes. Following multiple wash steps in 0.5% saponin FACS buffer, cells were resuspended in AlexaFluor 488 (Life Technologies) or PerCp-Cy5.5 (Santa Cruz) conjugated secondary antibody solution (1:500 DF) for 30 minutes. After additional wash steps, cells were resuspended in 500µL FACS buffer.

**Table 2. Flow cytometry Primary Antibodies and Respective Isotypes.** Dilution, supplier, and catalog numbers for each antibody and isotype used for flow cytometry experiments are shown.

| Name | | Dilution Factor | Supplier | Catalog Number |
|---|---|---|---|---|
| Myocilin | Primary | 1:100 | Santa Cruz | sc-21243 |
| | Isotype | | | sc-3887 |
| Chitinase 3 Like 1 (CHI3L1) | Primary | 1:100 | R&D Systems | af2599 |
| | Isotype | | | ab-108-c |
| Tissue Plasminogen Activator (tPA) | Primary | 1:200 | Santa Cruz | sc-15346 |
| | Isotype | | | sc-3888 |
| CD73 | Primary | 1:200 | BioLegend | 344016 |
| | Isotype | | | 400110 |
| CD90 | Primary | 1:200 | BioLegend | 328118 |
| | Isotype | | | 400150 |

#### 3.3.6.2 Surface Marker Approach

Live cells (not fixed) were resuspended in 100µL fluorescently-conjugated antibody (Table 2) solution in FACS buffer on ice for 30 minutes. Multiple wash steps

with FACS buffer were then performed, followed by resuspension in 500µL FACS buffer. Samples remained on ice until analysis.

#### 3.3.6.3 Flow Cytometry Data Analysis

Data was collected with an Accuri C6 (BD Biosciences) at 35µl/min flow rates until at least 10,000 cellular events were recorded. Median fluorescent intensities (MFI) values for each marker expression were used for comparison between samples. For normalization and assessing non-specific antibody binding, unstained and isotype controls (Table 2) were also run for each sample type. Unstained MFI values were subtracted from all stained samples to account for differences in auto-fluorescence across cell type and donor strain (Overton, 1988). For isotype controls, normalized MFI values were compared against stained samples to confirm higher MFI values in stained samples.

### *3.3.7 Collagen Gel Contractility*

As a functional outcome measure, cell contractility was determined using a collagen gel contraction assay since trabecular meshwork cells have been shown to possess a dynamic contractile range (Dismuke et al., 2014b). Cells were resuspended in DMEM (no FBS) at 9 x $10^5$ cells/mL. Collagen type I (3mg/mL, 1% acetic acid, calf skin, MP Biomedical) was added to cells at a 1:2 volume ratio (collagen:cells) followed immediately by a pretitrated volume of 1M sodium hydroxide to neutralize the acidity. Collagen gels (1mg/ml, 6x$10^5$ cells/mL) were then cast in 96 well plates at 80µL gel solution per well. After 20 minutes to allow gelation, an equal 80µL volume of serum-free media was added to provide nutrients needed for attachment while minimizing proliferation. After 24 hours, gels were released from the walls of the 96-well plate using a pipette tip. Images of each gel were taken every hour for approximately 12 hours after

release; images were also taken the following day to record steady-state gel area. Using ImageJ, gel area was quantified for each image to determine the magnitude of gel contraction.

### *3.3.8 Phagocytosis Assessment*

A second functional property measured was phagocytosis. TM cells have been shown to be actively phagocytic *in vivo*, presumably to remove particulate/cellular debris to avoid clogging the meshwork (Buller et al., 1990; Sherwood and Richardson, 1988). To quantify phagocytosis, pHrodo green *e.coli* BioParticles (LifeTechnologies) were used following previously developed methods (Gagen et al., 2013). pHrodo particles have low fluorescence when at or near neutral pH levels, but increase in fluorescence at low pH, such as in lysosomes. Increases in fluorescence should, thus, be associated primarily with phagocytosed particles instead of particles attached extracellularly to cell membrane. Cells were seeded at 50,000 cells/$cm^2$ onto 48 well plates in Hanks' balanced salt solution (HBSS) supplemented with 5% FBS and 2mM L-glutamine. After 24 hours, pHrodo particles were reconstituted in HBSS media in enough volume to treat 2 million cells per vial. Particles were vortexed, sonicated, and added to cells.

After a 4 hour incubation at 37$^o$C, particles were removed and cells were detached with 0.05% Trypsin/EDTA. Samples were centrifuged and resuspended in 400µL FACS buffer and placed on ice. Data was collected with a BD Accuri C6 flow cytometer at 35µL/min. For normalization and accounting for auto-fluorescence, unstained samples were also run for each donor strain. Unstained MFI values were subtracted from phagocytically-challenged sample MFI values.

### *3.3.9 Statistics*

Triplicate samples were run for each cell donor strain for all experiments. Furthermore, at least three donor strains were tested for MSCs and at least two TM cell donor strains for each characterization approach. Two-way ANOVA was used to test for significant differences between MSCs and TM cells. For all experiments, p-values less than 0.05 were considered as statistically significant.

## 3.4 Results

### *3.4.1 Mesenchymal Stem Cell Characterization*

MSCs after expansion (passage 4 or 5) were characterized for a known MSC surface marker, CD90 (Figure 4a). Each MSC donor strains showed greater than 95% positive staining for CD90 when gated vs. isotype controls, in agreement with MSC characterization standards (Dominici et al., 2006). In addition, a known negative MSC surface marker, CD45, was tested and exhibited minimal expression in all MSC donor strains (Figure 4b). Furthermore, each MSC donor strain showed multi-lineage potential after induction toward adipogenic, chondrogenic, and osteogenic phenotypes (Figures 4c – e).

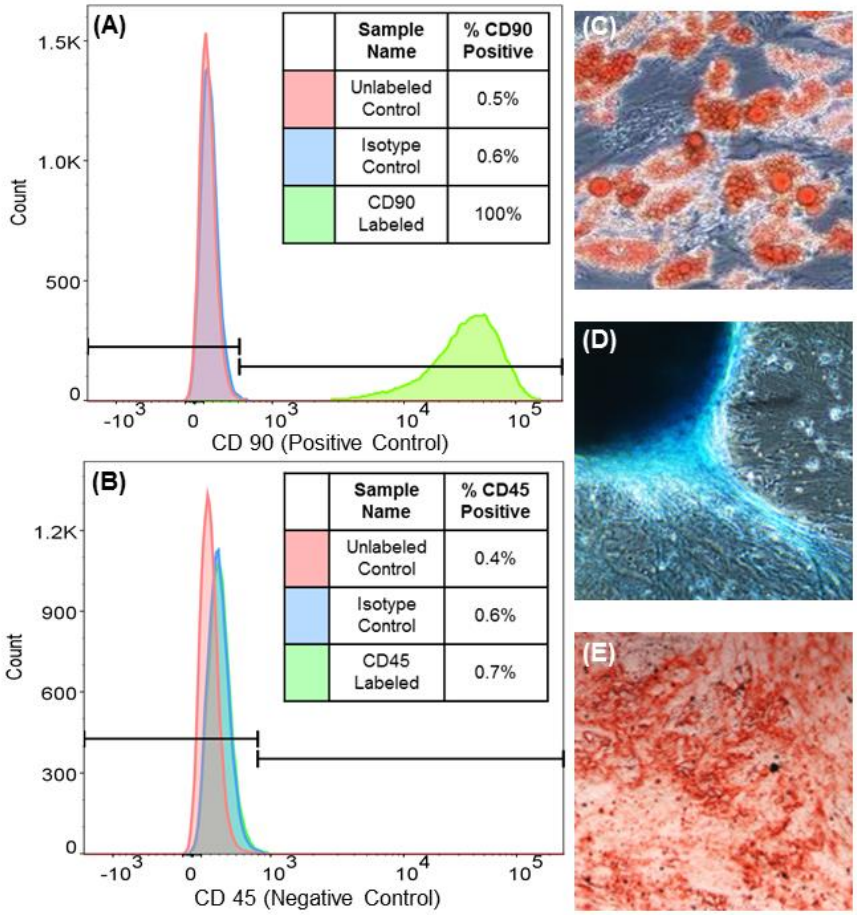


**Figure 4. Mesenchymal Stem Cell Characterization. (A-B)** Surface marker characterization by flow cytometry for MSC markers: **(A)** shows CD90, a positive marker and **(B)** shows CD45, a negative marker. Stained samples were compared against unstained and respective isotype controls to properly gate samples, as shown. **(C-E)** MSCs were stained with oil red O (lipids), alcian blue (glycosaminoglycans) and alizarin red S (free calcium) after treatment with adipogenic **(C)**, chondrogenic **(D)**, and osteogenic **(E)** differentiation stimuli. Images taken at 1, 2, and 3 week time-points, respectively.

### *3.4.2 Reverse Transcription Quantitative PCR*

#### 3.4.2.1 Identifying Suitable Reference Genes

To identify suitable reference (internal control) genes for this study, we used 3 MSC donor strains, 4 TM cell donor strains, and considered the effects of possible differentiation stimuli (such as mechanostimulation and hypoxia). Including all replicates,

33 different experiments were run for 7 potential reference genes (*GUSB, YWHAZ, TATA BP, B-Actin, GAPDH, cyclophilin*, and *18s rRNA*). Based on methods published (Vandesompele et al., 2002) and corresponding GeNorm software, the normalization stability for each reference gene was tested. The geometric mean of three markers (*GUSB, YWHAZ, TATA BP*) was found to provide the most stable normalization (Data not shown). For all subsequent RT-qPCR experiments, the geometric mean of these three genes was used for normalization of message levels.

#### 3.4.2.2 Gene-expression Analysis of MSCs vs TM Cells

To facilitate quantification, transcript expression levels were first normalized to the average of three reference genes as described above, and then further normalized to average expression of the same gene across three undifferentiated MSC donor strains. Based on these studies, five TM markers, *tPA, LDL Receptor, CHI3L1, MGP,* and *MYOC*, were selected to distinguish between TM cells and MSCs, with each expressed more highly in TM cells (Figure 5a). Furthermore, levels of *αB-crystalline*, a known juxtacanalicular tissue (JCT) marker, and *VE-Cadherin*, a Schlemm's canal endothelial cell marker, were assessed as a way to distinguish nearby ocular tissues vs. TM cells (Figure 5b). Lastly, two MSC markers, *Muc1* and *CD105*, were identified which were consistently more highly expressed in MSCs compared to TM cells (Figure 5c). All of these markers were selected as they consistently showed MSC vs. TM cell differences while other markers were heterogeneous across tested donor strains (data not shown).

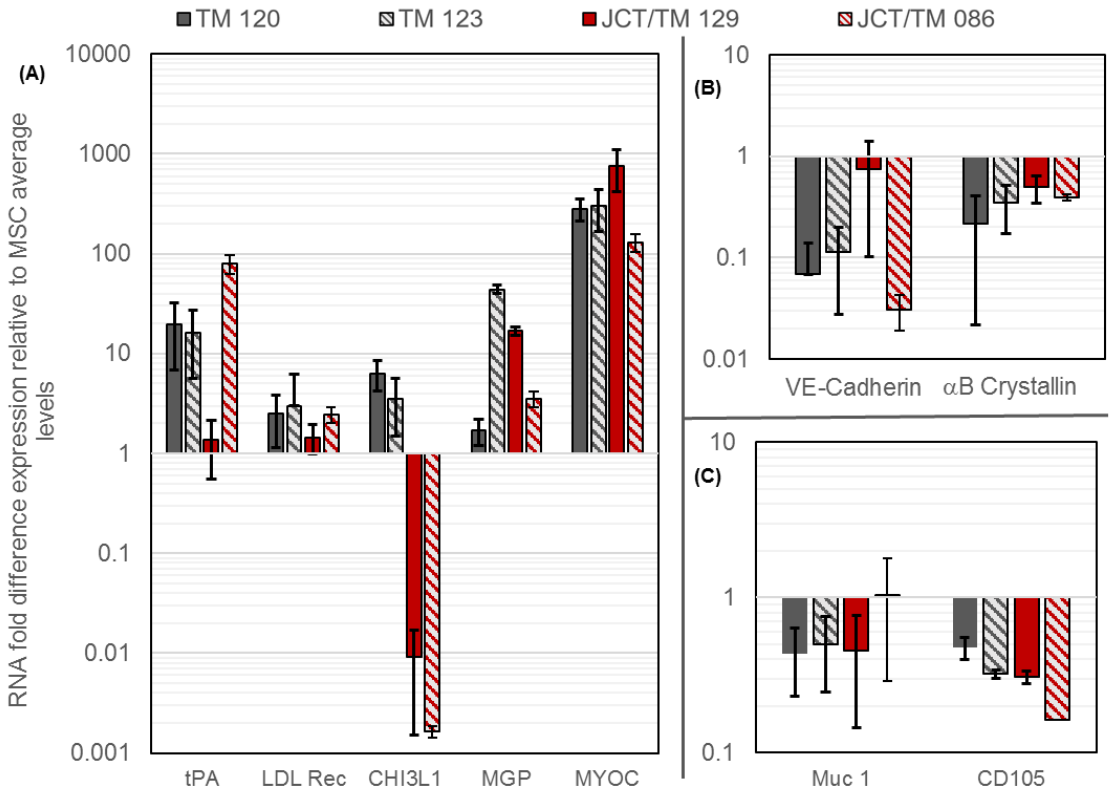


**Figure 5. mRNA Transcript Levels in TM cells, Measured by RT-qPCR and Normalized Against MSC Transcript Levels.** Fold-difference mRNA expression levels in four TM cell strains (TM 120, TM 123, JCT/TM 129, JCT/TM 086 [denoting higher JCT content in donor strains]) relative to the average expression in 3 MSC strains are shown for: **(A)** TM cell, **(B)** Schlemm's canal and JCT cell, and **(C)** MSC markers. Data was first normalized to the geometric mean of three reference markers (GUSB, TATA BP, and YWHAZ) in each sample, as described in the text. Error bars denote standard deviations (n=3 replicates for each strain).

### *3.4.3 Dexamethasone Induction of MYOC*

#### 3.4.3.1 Western Blot Analysis

MYOC protein levels from cell lysates were quantified with and without DEX treatment for three MSC and four TM cell donor strains. For each donor strain, MYOC (55kDa) band intensity was normalized against total protein fluorescent signal to account for loading variability (Figure 6a). Each MSC and TM cell donor strain tested was consistent across their respective groups (Figure 6b), with TM cells showing

approximately 4-fold increased MYOC expression after DEX treatment whereas MSCs showed minimal changes in expression ($p < 0.002$; Figure 6c).

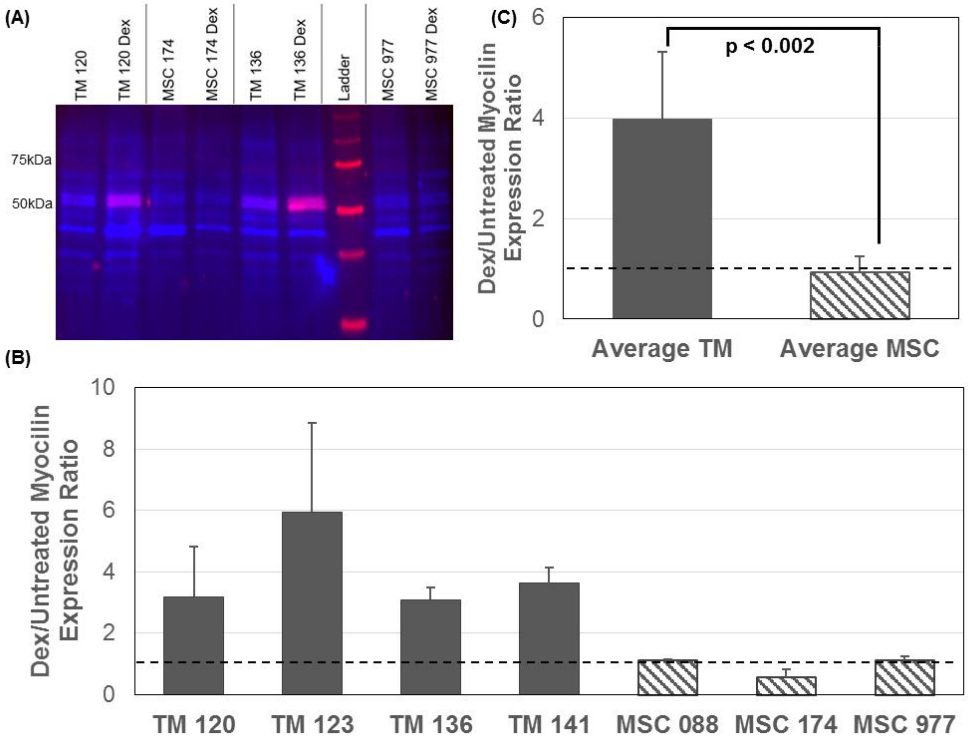


**Figure 6. Western Blot Analysis for Dexamethasone Induction of Myocilin in TM Cells and MSCs. (A**) Representative western blot against myocilin (red) and total protein (blue) for TM cells and MSC with and without dexamethasone. Molecular weight markers (labeled "ladder" in the figure) are shown in red. **(B)** Quantification of myocilin expression changes after dexamethasone treatment for four TM cell and three MSC donor strains (n=3 replicates for each strain). The vertical axis is normalized myocilin band intensity after DEX treatment divided by band intensity in control (vehicle-treated) cells. **(C)** Average values for TM cells and MSC ($p < 0.002$). Error bars denote standard deviation throughout.

3.4.3.2 Flow Cytometric Analysis

Intracellular MYOC protein levels were further quantified within fixed cells by flow cytometry. DEX-treated and untreated samples were prepared in triplicate for each donor strain and compared against unstained and isotype controls to confirm MYOC-specific staining (Figure 7a). Consistent increases in MYOC expression (~1.9 fold) after

DEX in all TM cell donor strains and slight decreases in MSC donor strains (~0.7 fold) were seen (Figure 7b). As was the case for Western blots, these differences were statistically significant (Figure 7c, $p < 0.0001$).

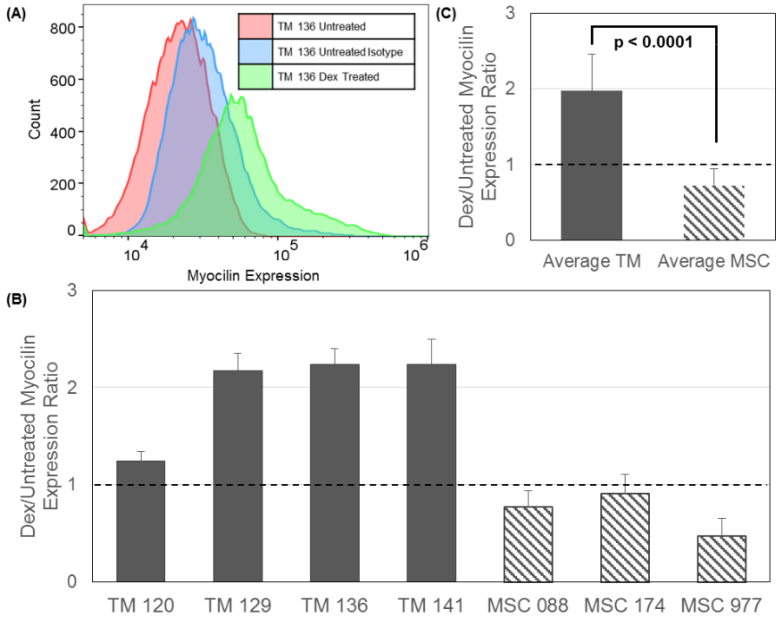


**Figure 7. Flow Cytometric Analysis for Dexamethasone Induction of Myocilin in TM Cells Versus MSCs. (A)** Representative histograms for myocilin expression in isotype controls (red), untreated cells (blue), and DEX-treated samples (green). **(B)** Quantification of myocilin expression (median fluorescence intensity) changes after dexamethasone treatment for four TM cell and three MSC donor strains (n=3 replicates for each strain). **(C)** Average ratio value for TM cells and MSCs ($p < 0.0001$). Error bars denote standard deviation.

### *3.4.4 Additional Protein Markers*

Protein expression of differentially expressed mRNAs were assessed since gene expression analysis by RT-qPCR doesn't necessarily translate to protein expression. 2 TM cell donor strains and 3 MSC cell donor strains were examined for the expression of CHI3L1 and tPA, intracellular markers for TM cells, as well as CD73 and CD90, cell surface markers for MSC cells. (Figure 8). CHI3L1 and tPA were consistently expressed

at higher levels in TM cells while CD73 and CD90 were more highly expressed across tested MSC donor strains.

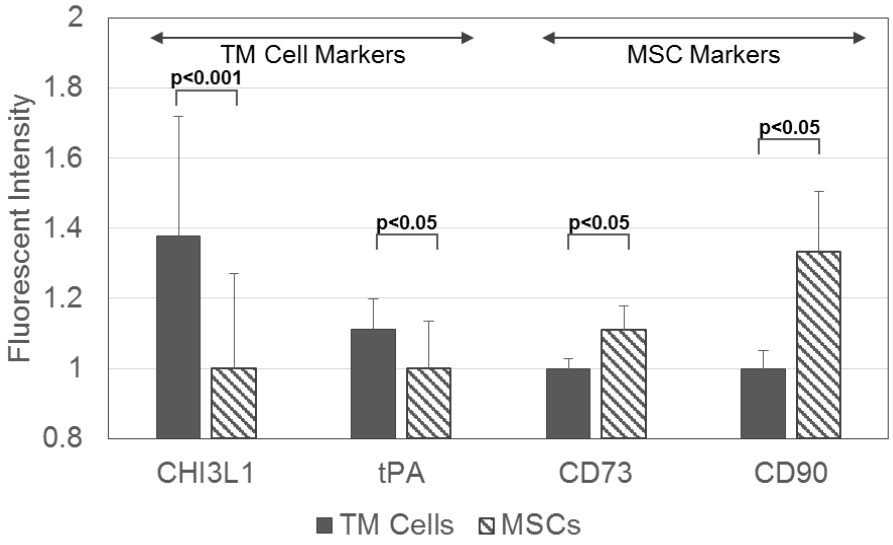


**Figure 8. Protein-level Characterization of MSCs and TM Cells.** Shown are select protein markers for TM cells and MSCs using flow cytometry. Average fluorescent intensity values for TM cells (n=2 donor strains) and MSCs (n=3 donor strains) are shown for four protein markers. Error bars denote standard deviation, and p-values are shown on the plot.

### *3.4.5 Collagen Gel Contractility*

Cells grown in free-floating collagen gels were allowed to reach a homeostatic contraction state to assess cell contractility (Figure 9a). At the point of gel release from sides of culture plate wells, the gel immediately began to contract (Figure 9b). After sufficient time (8+ hours), a steady state gel size was reached. Consistent and significant differences between gels seeded with TM cell and MSC donor strains were observed (55% vs. 15% initial gel area, respectively) after reaching steady state (8+ hours, Figure 9c, $p<0.0005$).

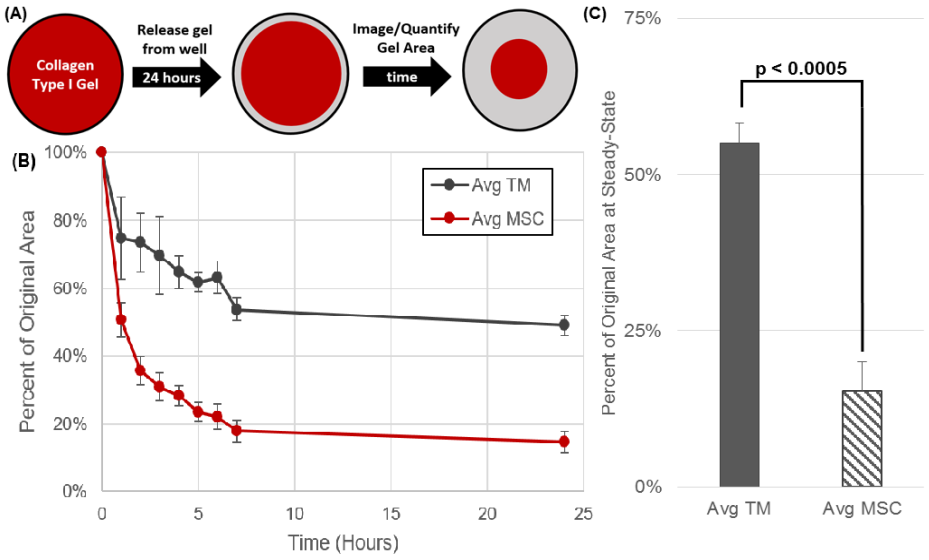


**Figure 9. Comparison of TM Cell and MSC contractility. (A)** Schematic diagram of collagen gel contraction assay. **(B)** Average change in collagen gel area relative to initial gel size for TM cells and MSCs during the first seven hours after release from the well. **(C)** Percent of original gel area for TM cells and MSCs at equilibrium (>8 hours, $p < 0.0005$). Three TM cell and MSC donor strains were used. Error bars denote standard deviation.

### *3.4.6 Phagocytosis*

pHrodo particles were added to densely seeded cell monolayers for 4 hours to allow time for phagocytosis and an increase in fluorescence intensity as particles reached lysosomes (Figure 10a). By flow cytometry, three MSC and TM cell donor strains were quantified for phagocytic activity after 4 hours, showing an approximately 2.25-fold greater fluorescence signal in all TM cell vs. MSC donor strains (Figure 10b). This difference was statistically significant when comparing average TM cell and MSC values across all tested donor strains (Figure 10c, $p < 0.0001$).

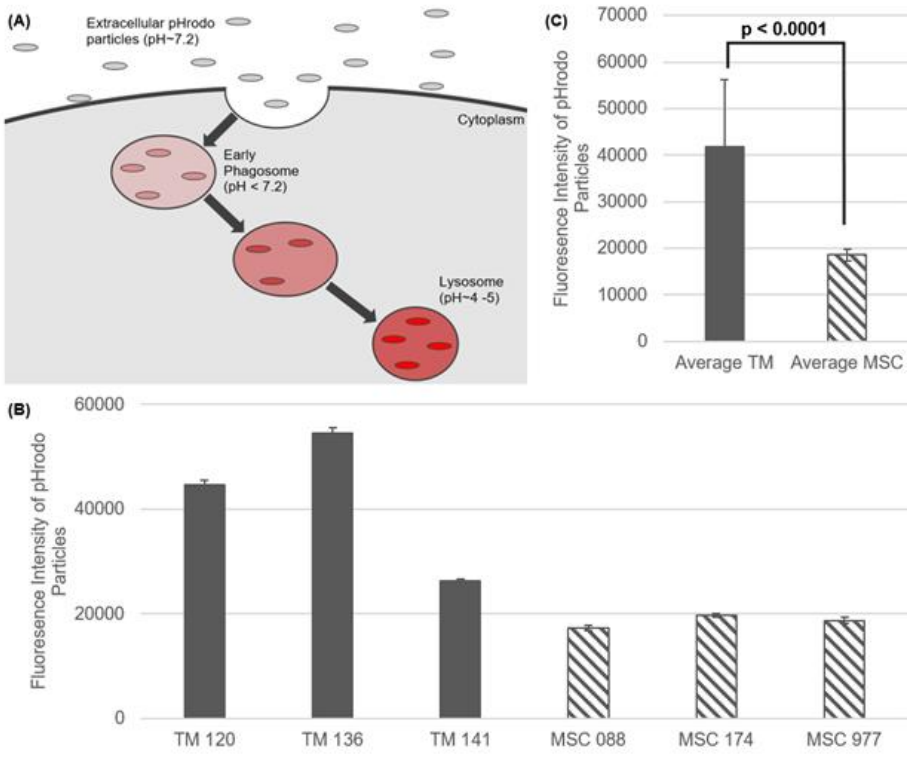


**Figure 10. Comparison of TM Cell and MSC Phagocytic Activity. (A)** Schematic diagram of phagocytic assay and pHrodo particles' fluorescent properties. Using this assay **(B)**, fluorescent intensity from flow cytometry after four hours' incubation is shown for individual TM cell and MSC donor strains. **(C)** Average values for TM cells and MSCs ($p < 0.0001$). Error bars denote standard deviation.

### 3.5 Discussion

MSC-based therapies to restore the cellularity and functionality of the trabecular meshwork represent a viable novel strategy to treat and manage ocular hypertension, a key feature of glaucoma. To confirm MSCs are capable of differentiating to a TM-like phenotype, methods to properly characterize differentiated MSCs for TM-like characteristics are first required. Using a series of characterization approaches, we here present methods that for the first time assess messenger, protein and functional level differences between undifferentiated MSCs and TM cells.

For a robust, high-throughput method, a panel of genetic markers were proposed and tested for message-level differences between MSCs, TM cells, and other neighboring eye phenotypes. DEX induction of MYOC, commonly used to identify TM cells isolated from tissue, was markedly different when comparing TM cells and MSCs, as shown by western blot and flow cytometric analysis. Additional TM cell and MSC protein markers were further characterized by flow cytometry. Finally, functionality was tested using a gel contractility assay and a phagocytosis assay where consistent differences were found between TM cells and MSCs. Overall, this series of assays provides characterization on several levels to broadly assess MSC differentiation to a TM-like phenotype, and is an important step toward developing possible MSC-based glaucoma therapies.

At the message level, RT-qPCR analysis was performed to develop a gene panel of differentially expressed and control mRNAs for MSCs and TM cells. This approach provided a robust characterization of differentiation, since a panel of message-level markers could be assayed across a number of samples at once. For suitable normalization of PCR experiments, we determined reference or internal control genes for our specific application. Since differentiation pathways for MSCs to TM cells are currently unknown, we examined changes in the levels of seven different reference genes across a number of MSC and TM cell donor strains, as well as after exposure of these cells to several possible differentiation stimuli (i.e. mechanostimulation, hypoxia). The geometric average of three markers (*YWHAZ, TATA BP, GUSB*) was found to be most consistent. The geometric mean was used instead of the arithmetic mean since it better controls for outliers and large differences between genes (Vandesompele et al., 2002).

With suitable normalization established, we assessed multiple messages for TM cells, MSCs, and other relevant ocular cell types to identify transcripts consistently expressed in the MSC and TM cell donor strains used. Specifically, a panel of twelve markers was selected: 3 reference, 5 TM cell-specific, 2 MSC-specific, 1 JCT-specific, and 1 Schlemm's Canal endothelial cell-specific. We included a JCT marker, *αB Crystallin*, since even though the JCT region is considered part of the TM, resident JCT cells differ morphologically and functionally from the remainder of the TM, making it relevant to know if a more JCT-like phenotype (myofibroblast) was forming vs. an endothelial-like phenotype characteristic of the inner portion of the TM (Braunger et al., 2015; Stamer and Clark, 2016). Similarly, Schlemm's canal endothelial cells lie immediately adjacent to the TM and, as a result, a marker was selected to distinguish a Schlemm's canal phenotype vs. TM cell phenotype. This panel showed clear expression differences between MSCs and TM cells, and RT-qPCR was attractive for differentiation characterization since assessing multiple markers in a single experiment allowed for high-throughput screening, not possible in standard protein-level characterization methods. Furthermore, messenger level analysis is much more sensitive that standard protein expression assays, capable of detecting signals in very small quantities of cellular RNA (Iscove et al., 2002).

At the protein level, we induced MYOC expression with DEX treatment. As shown first by western blot analysis, differences in MYOC expression following DEX treatment were consistently found between TM cells and MSCs. One issue with western blotting, particularly in differentiation studies, is identifying suitable markers for loading control normalization. Rather than focus on a single protein marker, we normalized using total protein labeling with trihalo compounds, which bind to protein residues after UV activation. This approach has been shown to be more robust and reliable compared to

standard single loading control normalization(Gilda and Gomes, 2013). Compared to other total protein stains, trihalo compounds are loaded in the gel prior to SDS-PAGE meaning no staining steps are needed and total protein signal is obtained quickly by 2.5 minutes of UV activation.

DEX induction of MYOC was also investigated using flow cytometry. Similar to western blot analysis, consistent results were found, with TM cells increasing their MYOC expression after DEX treatment while MSCs decreased their MYOC expression. Although western blotting is more traditional, flow cytometry is attractive for several reasons: it allows for normalization at a single cell level and for simple multiplexing to other possible markers of interest. Also, due to single-cell events, heterogeneity can be separated out in experimental samples, possibly allowing for quantification of cells with higher or lower protein expression as a means of assessing differentiation efficiency.

MYOC is a robust marker for TM cells, but additional rigor was sought by testing other markers. Thus, protein-level detection was performed by flow cytometry on additional MSC and TM cell markers. Specifically, CHI3L1 (Gonzalez et al., 2006) and tPA (Stamer et al., 1995) are both established TM cell markers and were found to be expressed at higher levels in TM cells vs. MSCs. With the multiplex capabilities of flow cytometry, these two markers as well as MYOC could be characterized simultaneously, reducing sample size and increasing throughput. In addition to TM markers, we also studied known stem cell markers, so that loss of stem-phenotype could be monitored as cells were differentiating. Specifically, CD73 and CD90 were found to be expressed at higher levels in MSCs vs. TM cells, providing additional protein-level characterization points for further studies.

While protein and messenger-level changes can show evidence of TM-like phenotype, functional assays are also needed. We thus used a gel contraction assay to test for cell contractility, a characteristic property of the TM (Dismuke et al., 2014b). Alterations to TM permeability, and, thus, outflow resistance, are believed to be related to the cells' contractile capabilities, making this a key functional parameter for TM cells (Llobet et al., 2003). Due to differences in the rate of proliferation between cell types and the impact that cell number has on gel contraction, collagen gels were created and remained in serum-free media for the entire assay. Contrary to our expectation, we consistently observed higher levels of contraction in MSC gels one hour after release and persisting through to steady state for all MSC and TM cell donor strains tested. While not normally thought of as contractile, MSCs share many functional characteristics with fibroblasts, a known contractile cell type, and have also been shown elsewhere to be contractile (MacQueen et al., 2013). Regardless, significant and robust contraction differences were found between TM cells and MSCs, providing a useful functional measure of cell phenotype.

Like contractility, phagocytosis is a vital function for TM cells (Buller et al., 1990; Johnson et al., 1989; Sherwood and Richardson, 1988). Conversely, MSCs have not been reported to be phagocytic, making this parameter a possible further functional difference between cell types. Using pH-sensitive particles, confounding issues in regards to insufficient washing and particles sticking to the extracellular plasma membrane are avoided entirely since fluorescence outside the cell should remain minimal. After four-hour exposure, higher uptake was consistently seen in TM cells vs. MSCs. However, MSCs fluorescence was much greater than the unstained controls, indicating phagocytosis or particle acidification was also occurring in MSCs.

## 3.6 Conclusions

Overall, the methods described here provide multiple approaches to quantify differentiation of MSCs to TM cells. RT-PCR allows for high-throughput analysis of multiple parameters simultaneously, useful in pilot experiments, and we have developed a panel of transcripts that will be useful in further TM differentiation studies. At the protein level, DEX induction of MYOC is essential to differentiation detection since this phenomenon is robust and unique to a TM-like phenotype. We recommend quantifying DEX induction using flow cytometry to allow for multiplexed assays of MYOC plus the other protein markers described herein. Finally, functional-level characterization should be considered in order to truly confirm differentiation to a TM-like phenotype. We specifically suggest that at least one functional parameter, either contractility or phagocytosis, should be used for this purpose. The results described herein will be valuable as glaucoma therapies based on differentiation of MSCs to a TM-like phenotype are developed.

## 3.7 Acknowledgments

This material is based upon work supported by the National Science Foundation (EJS, DGE-114890), Georgia Research Alliance (CRE), and Research to Prevent Blindness (WDS).

# CHAPTER 4. An Ultrasound-Photoacoustic Imaging Platform for Visualizing Mesenchymal Stem Cell Delivery and Retention in the Trabecular Meshwork

This chapter is a manuscript to be submitted to APL Bioengineering with the following author list: Kelsey Kubelick*, Eric J. Snider*, C. Ross Ethier, Stanislav Emelianov (*Denotes co-first author). The co-first authors were responsible for the following aspects of this work:

- **KK** – performed electron microscopy experiments, all US-PA imaging as well as subsequent US-PA image analysis (unmixing, signal distribution, polar histograms)
- **EJS** – maintained and prepared all cells for experiments, injected cells into eyes and processed all porcine tissue, conducted fluorescent imaging, and correlation analysis

---

## 4.1 Abstract

Glaucoma is a major cause of blindness and is associated with elevated intraocular pressure. The trabecular meshwork (TM), the tissue that primarily regulates intraocular pressure, is known to have reduced cellularity and presumably reduced function in glaucoma. Thus, stem cells offer a novel therapeutic route for glaucoma if properly delivered to the TM. Mesenchymal stem cells (MSCs), which are readily isolated from adult tissue, have been delivered to the TM; however, MSC delivery efficiency, as determined by histology at single time points, has been inconsistent. To further study MSC delivery to the TM, improved imaging is needed to track cells non-invasively. Here, we show that ultrasound and photoacoustic (US-PA) imaging has the

potential to monitor stem cell delivery to the TM, in real-time and longitudinally. Gold nanosphere-labeled MSCs (AuNS-MSCs) could be distinguished from background PA signals using spectroscopic PA imaging. AuNS-MSCs were tracked during delivery into the porcine anterior chamber and were also detectable 5 hours post-delivery after retention in anterior segment tissues. Furthermore, US-PA imaging was validated by comparison to fluorescent microscopy results. Overall, this study provides proof-of-concept that US-PA imaging can assess MSC delivery in the anterior eye to monitor and improve cell-based therapies.

## 4.2 Introduction

Glaucoma, a leading cause of blindness, affects over 70 million people worldwide. Its incidence is expected to continue to rise as the population ages (Cook and Foster, 2012; Quigley and Broman, 2006). A well-established risk factor for glaucoma is elevated intraocular pressure (IOP), which is determined by aqueous humor production rate within the eye and the subsequent outflow of aqueous humor through drainage pathways in the anterior eye (Weinreb and Khaw, 2004). The primary aqueous humor drainage route, known as the conventional pathway, consists of the trabecular meshwork (TM), Schlemm's canal, and, eventually, the circulatory system (Fautsch and Johnson, 2006; Goel et al., 2010).

In glaucoma patients, the cellularity of the TM is reduced (Alvarado et al., 1984; Baleriola et al., 2008; Gonzalez et al., 2006; Liton et al., 2005). The TM, along with the inner wall of Schlemm's canal, is known to be the major site of outflow resistance. In a healthy eye, TM cells phagocytose debris from the aqueous humor to prevent outflow blockage, contract to alter outflow resistance, and actively remodel their extracellular matrix to modulate tissue permeability (Bradley et al., 2003; Buller et al., 1990; De Groef

et al., 2013; Llobet et al., 2003; Sherwood and Richardson, 1988). Thus, reduced TM cellularity presumably leads to tissue dysfunction, increased outflow resistance, and subsequent elevated IOP. Therapies focused on restoring TM cellularity and function could thus offer a therapeutic benefit to glaucoma patients.

Towards this end, regenerative medicine therapies are being developed for the glaucomatous TM. Multiple studies have focused on using fibroblast-derived induced pluripotent stem cells (iPSCs) to create functional TM-like cells (Abu-Hassan et al., 2014b; Ding et al., 2014; Zhu et al., 2016a). While iPSCs were shown to be able to differentiate into a TM phenotype, challenges due to teratoma tumor formation *in vivo* and regulatory hurdles make clinical translation difficult for the use of pluripotent stem cells (Fong et al., 2010; Neofytou et al., 2015). Alternatively, adult-derived mesenchymal stem cells (MSCs) can be used. MSCs are commonly used in a clinical setting and are readily isolated from sites such as bone marrow or adipose tissue (Jin et al., 2013).

While few studies to date have used MSCs for recellularizing the TM, two studies have investigated MSC delivery to the TM *in vivo* (Manuguerra-Gagne et al., 2013; Roubeix et al., 2015). Manuguerra-Gagne *et al*. demonstrated, in a laser-induced model of glaucoma in rats, that injected MSCs led to decreased IOP. However, only 11% of MSCs were found in the eye after 24 hours and no cells were found after 96 hours. Similarly, Roubeix *et al.* demonstrated, in an episcleral vein cauterization model of glaucoma in rats, that injected MSCs also reduced elevated IOP. Interestingly, MSCs were observed in many anterior tissues, including the TM, for at least 24 days. However, the majority of MSCs were found on the corneal endothelium, iris, and ciliary processes as opposed to the desired TM location.

While both studies demonstrate potential of MSCs for glaucoma treatment, delivery and retention of MSCs to the TM appears to be a challenge. As is the case for nearly all cellular therapies, studies to date have used histological processing at set time points to evaluate MSC location and study outcomes. Due to the invasive nature and tedious sample preparation of histology, it is impossible to monitor the same sample longitudinally. Thus, a noninvasive imaging modality would greatly benefit development of stem cell therapies in the anterior eye by providing real-time, longitudinal information on cell delivery to target tissues.

Ultrasound and photoacoustic (US-PA) imaging are excellent options for noninvasive, longitudinal stem cell tracking. Ultrasound (US) imaging is based on scattering of high-frequency acoustic waves and has already been used to visualize changes in the anterior segment of glaucomatous eyes (Marchini et al., 1998; Nolan, 2008; Pavlin et al., 1992; Sakuma et al., 1997; Thomas et al., 2014). Because image contrast in ultrasound imaging depends on scattering, it is effective for depicting the overall anatomy of the anterior segment, but is poorly suited to distinguishing a specific signal of interest, such as the presence of stem cells. Fortunately, photoacoustic (PA) imaging has the potential to supplement the anatomical information provided by ultrasound imaging. In PA imaging, pulsed laser irradiation of optical absorbers leads to thermoelastic expansion of the surrounding tissue to produce a pressure wave that is detectable by an ultrasound transducer (Xu and Wang, 2006). PA imaging has sub-millimeter resolution, high contrast, and increased imaging depth compared to purely optical methods. PA signal can be generated by endogenous tissue absorbers, such as melanin and hemoglobin, or exogenous absorbers, such as dyes and nanoparticles (Cook et al., 2011; Galanzha et al., 2009; Kim et al., 2009; Krumholz et al., 2014; Wang and Yao, 2016). Because PA imaging depends on optical absorption, the modality

directly compliments information from ultrasound, and is better suited to tracking a target of interest. By using optical absorbers to label stem cells, US-PA imaging has been applied to assay stem cell delivery in other applications (Jokerst et al., 2012; Nam et al., 2012; Ricles et al., 2014).

Here, we have developed an US-PA imaging scheme for tracking labeled MSCs in the anterior segment of the eye. We previously characterized endogenous PA signal in the porcine anterior segment (Kubelick et al., 2017, in preparation). Using this information, we hypothesized that gold nanospheres would be an effective contrast agent to distinguish labeled stem cells from endogenous absorbers in the anterior segment. Designing a detection protocol based on US/PA imaging for TM regenerative medicine will allow for non-invasive monitoring of stem cell delivery, simplifying optimization and expediting development of novel therapies for glaucoma treatment.

## 4.3 Methods and Materials

### *4.3.1 Mesenchymal Stem Cell Sourcing*

Human adipose derived MSCs (Lonza) were grown in α-minimum essential medium supplemented with 20% fetal bovine serum (FBS), penicillin, streptomycin, and L-glutamine. At 80-90% confluency, MSCs were detached using 0.05% Trypsin/EDTA and seeded in fresh cell-culture T75 flasks at a seeding density of 5,000 cells/cm$^2$. In all experiments, MSCs were used at passage numbers five or six. Each MSC donor strain was validated by Lonza for expression of MSC surface markers (CD13, CD29, CD44, CD73, CD90, CD105, and CD166) and minimal expression of negative MSC markers (CD14, CD 131, CD45). Each MSC donor strain was also previously characterized in our lab for adipogenic, chondrogenic, and osteogenic differentiation as well as CD90 expression following expansion (Snider et al., 2017).

### *4.3.2 Gold Nanotracer Synthesis*

Hydrogen tetrachloroaurate (III) hydrate ($HAuCl_4$ x $H_2O$, Alfa Aesar) and sodium citrate tribasic dihydrate ($HOC(COONa)(CH_2COONa)_2$ x $2H_2O$) Sigma Aldrich), were used as received. Gold nanospheres (AuNS), 20nm diameter, were synthesized via the citrate reduction method (Kimling et al., 2006; Turkevich, 1985; Turkevich et al., 1951). Briefly, 0.5ml of a 1% w/v solution of hydrogen tetrachloroaurate was added to 47ml of deionized ultrafiltered water. The solution was brought to a boil while stirring, then 2.5ml of a 1% w/v solution of sodium citrate was added. After approximately 15 minutes, the solution appeared red and was cooled to room temperature. UV-Vis spectrophotometry (Synergy HT microplate reader, BioTek Instruments) between 400nm to 995nm was used to validate the absorbance spectra and optical density of the particles. Transmission electron microscopy (TEM) (Hitachi HT7700 TEM, IEN/IMAT Materials Characterization Facility, Georgia Institute of Technology) was used to validate particle size and morphology. AuNSs were sterilized under UV light for at least 12 hours prior to stem cell labeling experiments.

### *4.3.3 AuNS and CFSE Stem Cell Labeling*

Gold nanoparticles were incubated for 24 hours with adipose derived MSCs (Lonza) at an optical density of 2, a measure of concentration according to light absorbance, in alpha-minimum essential medium (Mediatech) supplemented with 20% fetal bovine serum, 2mM L-glutamine, and 1x penicillin/streptomycin. AuNS were previously determined to have minimal cytotoxic effects on stem cells (Ricles et al., 2011). Following uptake, gold nanosphere-labeled stem cells (hereinafter referred to as AuNS-MSCs) were collected and used for cell tracking experiments. AuNS-MSCs were washed with PBS to remove excess nanoparticles, detached with Trypsin-EDTA, and

centrifuged (300 x g, 10 minutes) to separate free AuNS from AuNS-MSCs. For fluorescent cell detection, MSCs were also labeled with 5μM carboxyfluorescein succinimidyl ester (CFSE, Affymetrix) for fifteen minutes at 37°C, followed by washing with cell culture media to remove excess CFSE.

We used a Vevo 2100 imaging system, incorporating ultrasound and photoacoustic (US/PA) imaging modalities (VisualSonics, Inc., see section 4.3.6 for further details), to verify that AuNS-MSCs were labeled and produced a photoacoustic signal. AuNS-MSCs were imaged in a tissue-mimicking gelatin phantom (Cook et al., 2011). The base of the phantom consisted of 8% (w/v) gelatin and 0.2% (w/v) silica (Sigma-Aldrich). Inclusions were made by adding 16% (w/v) gelatin to an equal volume of AuNS-MSCs. Each inclusion was imaged over a range of wavelengths (λ=680 nm to 970 nm at 5nm increments), with the US/PA transducer oriented perpendicular to the gelatin base.

### *4.3.4 Stem Cell Delivery in ex vivo Experiments*

For ocular delivery experiments, porcine eyes from a slaughterhouse (Holifield Farms, Covington, GA) were used within 3 to 4 hours of enucleation. To maintain physiological pressures during cell injection, a reservoir containing serum-free, phenol red-free DMEM (supplemented with 1x penicillin, 1x streptomycin, 1x amphotericin, and 2mM L-glutamine) was connected to each eye by cannulating the anterior chamber using a 23-gauge needle passing through the cornea. Reservoirs were placed 10 to 16 cm above the limbus (cornea-sclera transition region) to clamp intraocular pressure (IOP) at 8 to 12 mmHg. 250 μL of a solution containing AuNS-MSCs was injected into the anterior chamber through the central cornea using a 27-gauge needle. We used a variety of cell concentrations so that either 250,000, 500,000 or 1,000,000 (250k, 500k,

and 1000k, respectively) AuNS-MSCs were delivered into the eye. After injection, eyes remained pressure clamped at 8 to 12 mmHg, and were stored in a cell culture incubator for 5 hours. At five hours post-injection, eyes were perfused with 10% formalin overnight at 8 to 12 mmHg IOP, followed by submersion in 10% formalin overnight to fully fix eyes. Some eyes were US-PA imaged for 15 minutes following AuNS-MSC injection as indicated. All eyes (n=3 for each cell concentration) were US-PA imaged after fixation to assess AuNS-MSC delivery.

### *4.3.5 Anterior Segment Dissection*

Fixed eyes were dissected to isolate the anterior segment, similar to previously reported methods (Bachmann et al., 2006; Bhattacharya et al., 2009). Briefly, orbital connective tissue was dissected away, and eyes were hemisected with a razor blade to isolate the front half of the eye. The vitreous humor and lens were removed, the iris was cut radially back to the iris root and pectinate ligaments until the TM was revealed, and the ciliary processes were carefully removed while preserving the TM. Any remaining vascularized or pigmented tissue was removed. Dissected anterior segments (n=4 for each concentration) were again US-PA imaged to confirm TM delivery, as described below.

### *4.3.6 Ultrasound-Photoacoustic Imaging of Porcine Eyes*

The Vevo 2100 (VisualSonics) combined ultrasound and photoacoustic (US/PA) imaging system was used for all US/PA imaging. US/PA images were acquired using 20 MHz (LZ250/LZ550), 256 element transducers at a frame rate of 5Hz with an OPO, Q-switched Nd:YAG laser (λ=680-970nm, PRF=20Hz, 7ns pulse duration). Built-in software was used to calibrate laser energy across all wavelengths at the time of acquisition. A translational motor was used to acquire spatial 3D images as required.

Eyes or dissected anterior segments were secured on top of a tissue-mimicking phantom composed of 1% (w/v) agarose and fully submerged in PBS for imaging. All eyes were imaged with the transducer centered over the cornea, perpendicular to the surface of the tissue-mimicking phantom. During cell injections, US/PA images were continuously acquired at λ=700nm due to the high absorption of AuNS-MSCs and laser stability at that wavelength. Following injection, 2D US/PA images were acquired approximately every 3 minutes for 15 minutes from λ=680 to 970nm in 5nm increments, and again at 5 hours post injection. 3D spectroscopic images were also acquired at 5 hours post injection in whole eyes and dissected eyes. Due to hardware limitations, 3-dimensional images could only be acquired at a subset of wavelengths, and preliminary studies (data not shown) showed that imaging with λ=680nm to 710nm at 10nm increments produced PA signals from labelled cells that could be effectively separated from background signal.

### *4.3.7 Fluorescence Microscopy*

Following US-PA imaging of dissected eyes, scleral tissue posterior to the TM was removed to improve imaging, and dissected anterior segments were placed in PBS on a 50mm glass-bottomed dish so that the TM was in direct contact with the dish surface. Micrographs of the entire TM circumference were captured by confocal microscopy (LSM 700, Carl-Zeiss) to identify delivered CFSE-tagged MSCs in the TM region. Brightfield overlays were also captured to identify the corneal margin and hence the approximate location of the TM. Micrographs were captured as z-stacks of tile scans at 50x to account for TM depth and height differences in the tissue. Maximum intensity projections were created for each *en face* image for use in further image quantification.

### *4.3.8 Image Analysis*

#### 4.3.8.1 US-PA Image Processing

Spectroscopic PA images were unmixed at each pixel using Equation 1:

$$P = \Gamma \mu_a F = k\mu_a = k \sum_{i=1}^{n} C_i \sigma_{a_i} \qquad (1)$$

where P describes the measured PA signal in terms of pressure on the surrounding tissue; F is light fluence at the location of the absorber; and *r* is the Grüneisen parameter, a tissue-dependent efficiency factor describing conversion of light to pressure. The equation is simplified by treating the product of the fluence and the Grüneisen parameter as a constant, *k*. The optical absorption coefficient, $\mu_a$, depends on wavelength and is the product of the concentration of the absorber, C, and the optical cross sections of that absorber, $\sigma_a$, relative to its maximum (Luke et al., 2013). $\sigma_a$ was previously determined by spectroscopic PA analysis of endogenous anterior segment absorbers (Kubelick et al., 2017, in preparation) and AuNS-MSCs *in vitro*. In our case, we assumed that the photoacoustic signal at each pixel was the sum of contributions from melanin and AuNS-MSCs, i.e. n=2. Thus, solving for $C_i$ produced a map of unmixed amplitudes associated with each PA absorber with dimensions (depth x width x number of absorbers). Solutions for $C_i$ were restricted to positive values.

Images were post-processed using MATLAB. Prior to spectroscopic unmixing, PA images were spatially filtered using a 3 x 3 pixel (41µm x 45µm) median filter to remove speckle and large noise fluctuations. In the case of 2-dimensional spatial images, images were low pass filtered using a 6 pixel x 9 pixel x 3 frame moving average filter, approximately corresponding to 252µm x 405µm, three times the axial and lateral resolution, and a wavelength range of λ=15nm. In the case of 3-dimensional

spatial images, images were low pass filtered using only a 6 pixel x 9 pixel x 3 slice moving average filter, i.e. images were only spatially filtered. Signals below the threshold defined in Equation 2 were eliminated:

$$\text{Threshold} = P_{\text{minimum}} + 2.5\% \, (P_{\text{maximum}} - P_{\text{minimum}}) \qquad (2)$$

For dissected eyes, the 3-dimensional matrix of the unmixed PA signal from cells was integrated across the image depth to produce a 2-dimensional map of AuNS-MSC distribution around the circumference of the eye. The TM region was specifically isolated for analysis by producing a ring mask using anatomical landmarks. However, due to differences in imaging modalities, different anatomical landmarks were used for each imaging modality. For PA image analysis, the endogenous PA signal from melanin was used to define the inner (cornea-side, or anterior-most) margin of the TM. The outer (posterior-most) margin of the TM was then defined as 1mm posterior to the inner margin.

For fluorescent image analysis, images were filtered to eliminate noise spikes using the same median filter as used for PA images. The low pass filter was applied by spatially matching the largest dimension of the PA low pass filter, namely 400 µm. To isolate the TM region, the corneal margin was determined from the brightfield image, and the TM was defined as a 1mm wide band adjacent to this margin to match the photoacoustic image processing technique.

A polar coordinate system centered on the cornea was overlaid on all images and polar histograms were produced by integrating unmixed PA and fluorescent intensities from cells over $15^{o}$ wedges. Since the photoacoustic and fluorescent images were taken at different times, small notches were cut in the sclera of each eye to act as landmarks and thus provide approximate image orientation for subsequent alignment.

Notches were positioned at similar cardinal points during image acquisition for both modalities.

Fluorescent signal was summed around the entire 360$^{o}$ TM region for each fluorescent and photoacoustic image to assess agreement between each imaging modality. Signal from fluorescent images was not normalized for this analysis, while signal from PA images, due to fluctuations in laser power, was normalized to average PA signal from the PBS in which eyes were immersed. Signal from no cell, 250k, 500k, and 1000k AuNS-MSC injected eyes were compared using scatter plots of fluorescent signal vs. PA signal.

*Statistics*

For each MSC injected cell number (250k, 500k, and 1000k cells), n = 3 eyes were studied by US-PA imaging and fluorescent microscopy. For assessing correlations between imaging modalities, a Pearson correlation coefficient was calculated for each data set, with $p < 0.05$ denoting statistical significance as determined by Student's t-distribution.

## 4.4 Results

### *4.4.1 Labeling MSCs with AuNS and Their Corresponding Spectra*

AuNS were approximately 20 nm in diameter, as determined by TEM (Figure 11A). After incubating MSCs with AuNS at a concentration of 2 OD for 24 hours to allow cellular uptake of the nanoparticles, there was noticeable particle accumulation in the cytoplasm, as detected by light microscopy (Figure 11B, C). As expected, AuNS alone produced minimal photoacoustic signal at $\lambda$=700nm, since the absorption peak of the nanospheres is at $\lambda$=532nm (Figure 11D). Unlabeled MSCs were detected by ultrasound

but produced no PA signal (Figure 11E). However, AuNS-MSCs produced a PA signal at λ=700nm due to surface plasmon resonance coupling of nanoparticles that had been uptaken, as previously reported in other studies (Nam et al., 2012) (Figure 11F). This was consistent with light microscopy, showing successful labelling of MSCs with AuNS.

The PA spectrum of AuNS-MSCs from λ= 680 to 970nm was compared to measured PA spectra of melanin, expected to be the main endogenous absorber in porcine ocular tissue (Figure 11G). The PA spectral signature of AuNS-MSCs was distinct from melanin, opening the possibility for distinguishing AuNS-MSC signal from background in the eye. Overall, we conclude that AuNS particles can label MSCs, and that the distinct PA spectra of AuNS-MSCs is conducive to cell tracking in the porcine anterior segment using spectroscopic imaging.

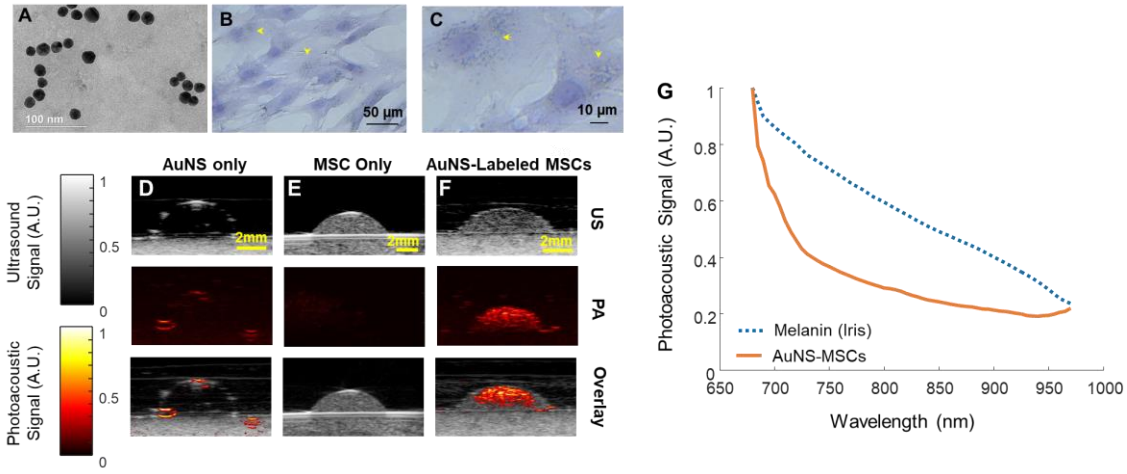


**Figure 11. AuNS Labeling of MSCs and Resulting PA Properties. (A)** TEM of AuNS showing uniformity and approximate particle size. **(B, C)** Brightfield micrograph of MSCs following AuNS incubation at 2OD for 24 hours. AuNSs are evident (arrowheads) around hematoxylin stained nuclei. **(D - F)** US-PA signal at 700 nm wavelength from gelatin phantoms for **(D)** AuNS only, **(E)** unlabeled MSCs, and **(F)** AuNS-MSCs. In panels D - F, the top row shows US signal only, the middle row shows the PA signal only, and the bottom row shows the merge. In panel D, the faint PA signal was due to trapped air bubbles in the gelatin inclusion, which were also evident by US imaging. **(G)** PA spectra

for AuNS-MSCs compared to melanin, thought to be the main endogenous absorber in the porcine eye.

### *4.4.2 US-PA Imaging of AuNS-MSC Injections into the Anterior Segment*

AuNS-MSCs were fluorescently tagged with CFSE and resuspended at 1 million cells/mL in media. While the eye was pressure clamped, 250µL of the MSC-containing solution was injected into the anterior chamber. PA images were acquired at $\lambda$=680 to 970nm. US-PA imaging occurred before, during, and for up to fifteen minutes after the cell injection.

Prior to injection, PA signal due to melanin was visible at the trabecular meshwork (TM) and iris, with additional signal at the site of the injection needle (Figure 12A) at $\lambda$=700nm. MSCs could be visualized by both ultrasound and PA imaging immediately after injection, confirming successful delivery into the anterior chamber (Figure 12B). However, when using only a single PA wavelength (700nm), AuNS-MSCs were difficult to detect at 9 minutes post-injection (Figure 12C), and seemed to have completely disappeared at 15 minutes post-injection (Figure 12D). We hypothesized that cells may have simply moved out of the plane of view, or may have traveled to surrounding tissues, where strong absorption from melanin at the iris and TM may have overpowered PA signal from AuNS-MSCs, making it impossible to visualize AuNS-MSCs with only a single imaging wavelength. Therefore, we carried out spectroscopic PA imaging with unmixing to accurately localize absorbers by detection of distinct spectral signatures of AuNS-MSCs and endogenous absorbers (Figure 12E-L). Prior to AuNS-MSC injection, spectroscopic unmixing accurately localized background signals (Figure 12E), with no AuNS-MSCs being detected (Figure 12F), as expected. Immediately after injection, PA signals from melanin remained separate from AuNS-MSCs (Figure 12F), with AuNS-MSCs being localized to the aqueous humor (Figure 12J). AuNS-MSCs

could still be visualized at 9 and 15 minutes post-injection using spectroscopic unmixing (Figure 12K, L) showing improved detection compared to single-wavelength PA imaging.

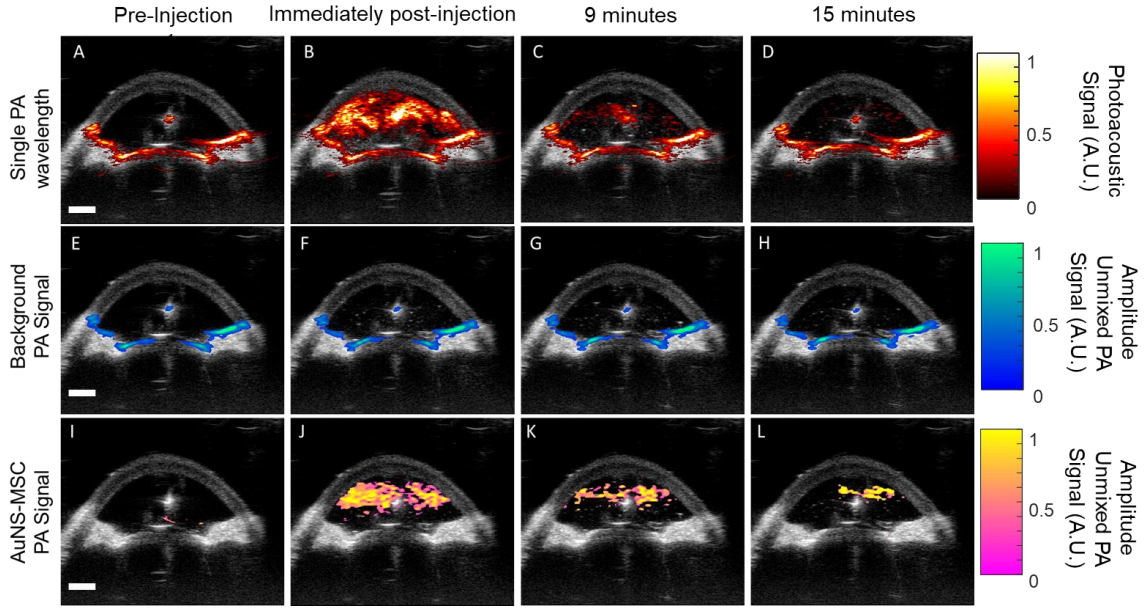


**Figure 12. Spectroscopic Photoacoustic Imaging of AuNS-MSCs Following Delivery to the Anterior Chamber.** Photoacoustic images (color scale) were analyzed before injection, and then immediately, nine, and fifteen minutes after injection (columns left to right). **(A-D)** Shows single PA wavelength imaging at 700nm, while **(E-L)** show spectroscopic photoacoustic imaging. **(E-H)** Image pixels classified as endogenous absorbers, primarily melanin-containing ocular tissues. **(I-L)** Image pixels classified as AuNS-MSCs. Scale bar= 3mm.

### *4.4.3 Detection of AuNS-MSCs in TM, 5 hours Post-Delivery*

Eyes were fixed 5 hours after AuNS-MSC delivery, and US-PA imaging was performed to assess the presence of AuNS-MSCs in the anterior segment. Eyes were injected with media-only (control eye; Figure 13 A, B), 250k (Figure 13 C, D), 500k (Figure 13 E, F), or 1000k AuNS-MSCs (Figure 13 G, H) in 250µL to determine if US-PA imaging was able to detect differences related to cell concentration. In the control eye, spectroscopic PA unmixing correctly identified endogenous background absorbers (Figure 13 A, B), indicating that melanin could be detected and isolated. Increased AuNS-MSC PA signal was qualitatively observed as the number of injected cells

increased (Figure 13 D, F, H). In the 250k cell eye, AuNS-MSCs were largely confined to the anterior surface of the lens (Figure 13D). As the injected cell number increased to 500k (Figure 13F) or 1000k (Figure 134H), cell signal extended to the anterior iris, and was even evident further into the anterior angle, indicative of some TM delivery. However, these images were for only a single sagittal plane through the anterior segment, and thus did not give a complete understanding of injected cell distributions in the anterior segment. We therefore created 3D images (Figure 13 I, J), which were generally consistent with 2D images. For example, greater AuNS-MSC signal was clearly observed when 1000k cells were injected (Figure 13 J) vs. in control eyes (Figure 13 I). Segmental, non-uniform delivery was evident from 3D views, i.e. cell signal was more concentrated in some regions while others contained minimal signal (Figure 13 J). Overall, spectroscopic PA imaging successfully separated PA signals from melanin-containing tissues from that of labelled cells. AuNS-MSCs were detected in anterior segment tissues up to 5 hours post-injection. Further as the number of injected cells increased, cells were more widely spread and the amplitude of unmixed PA signal on the MSC channel increased, as expected.

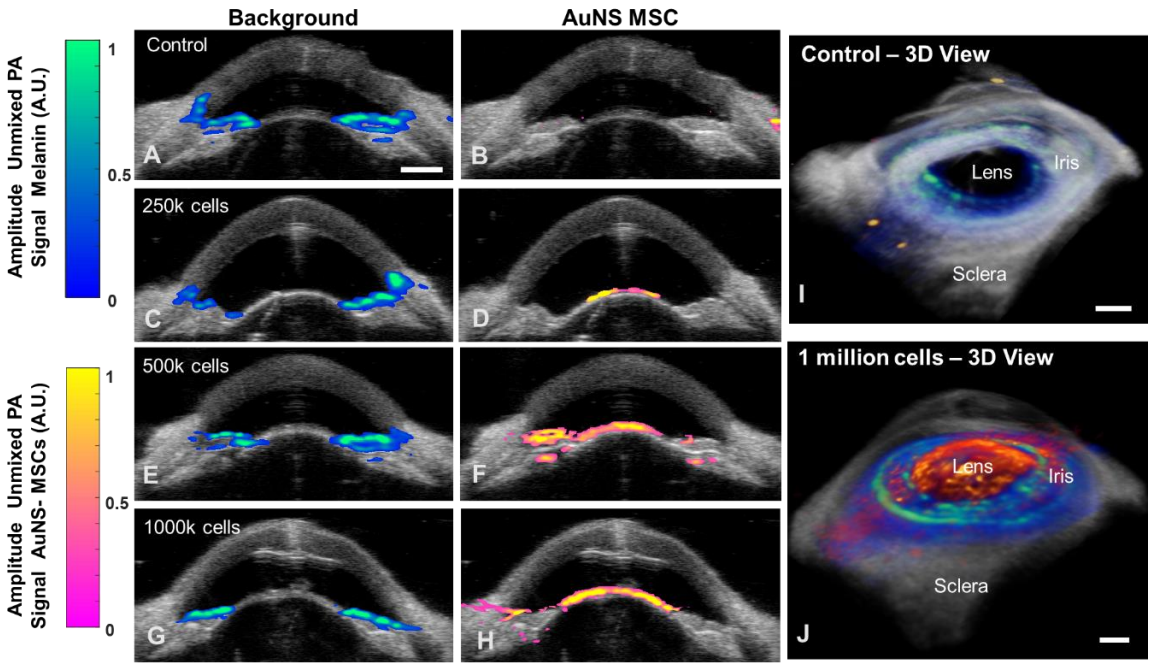


**Figure 13. Ultrasound-Spectroscopic Photoacoustic (US-PA) Imaging Detects AuNS-MSCs Five Hours After Injection.** Overlay of ultrasound (gray) and spectroscopic photoacoustic (color scale) images in single planes **(A-H)**. Each column separates photoacoustic signals according to melanin (left; "background") and AuNS-MSCs (right). Each row corresponds to different concentration of cell injection: **(A,B)** control, no cells, **(C,D)** 250,000 cells , **(E,F)** 500,000 cells, **(G,H)** 1,000,000 cells. 3D views of the anterior segment of each eye were also captured **(I,J)** to better show cell location around the entire TM circumference. **(I)** shows an eye with only vehicle (no cells) injected, while **(J)** shows a 1 million cell injection, both 5 hours after injection. Signal on the posterior sclera was due to signal spillover from regions of high PA signal. Yellow-pink color scale = labeled MSCs. Green-blue color scale = melanin. Scale bar = 3mm

### *4.4.4 Assessment of MSC delivery to the TM*

Eyes were dissected to isolate the anterior corneoscleral shell and thus specifically assess MSC delivery to the trabecular meshwork. These dissected ocular shells were imaged *en face* using fluorescence microscopy (Figure 14, Columns 1 and 2) and spectroscopic PA imaging (Figure 14, Column 4) to benchmark PA imaging against a more established method, namely fluorescence microscopy.

After selecting the TM region, fluorescent micrographs (Figure 14 A – C) were filtered similarly to photoacoustic images and shown as heat maps of AuNS-MSC signal intensity (Figure 14 D – E) for comparison to PA signal intensity (Figure 14 J – L). Heat maps were further used to create polar histograms of relative cell density to more easily visualize and compare cell distribution patterns (Figure 14 F – G and M - O). Fluorescent and PA signal distributions were similar for the 500k cell injection, and some regions in the 250k injection showed consistent signal between the two imaging modalities. However, on balance, the AuNS-MSC signal from PA images did not correlate particularly well with the fluorescent signal. Differences were most pronounced at the 1000k injections, where higher AuNS-MSC signal was evident by fluorescence imaging vs. PA signal.

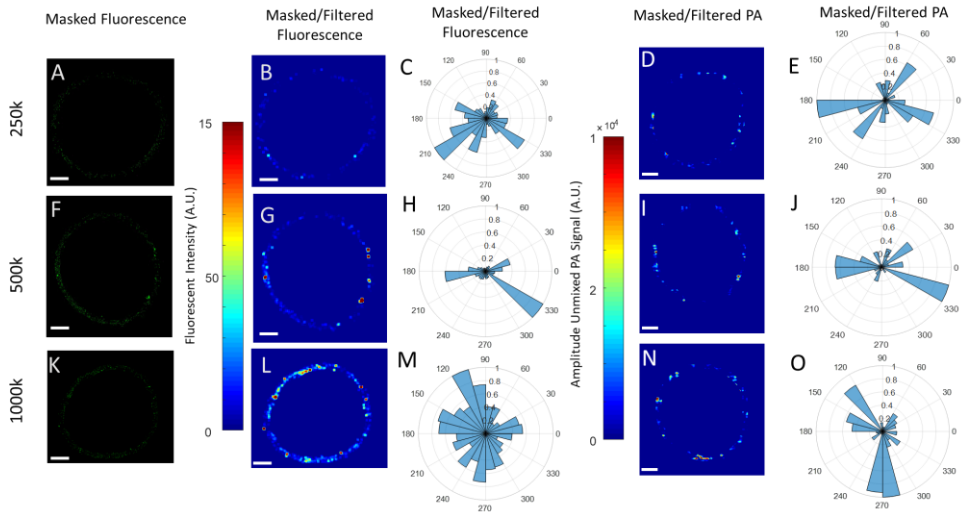


**Figure 14. Spectroscopic PA and Fluorescent Microscopy Images of Labeled MSCs with Additional Processing to Isolate the TM.** Each row shows one representative sample imaged with both modalities, with the top, middle and bottom rows corresponding to injection of 250k, 500k, or 1000k AuNS-MSCs, respectively. Each column depicts, in order from left to right: **(A, F, K)** the fluorescent signal masked to show only the TM region; **(B, G, L)** a filtered heat map version of the fluorescent signal relative to maximum signal intensity; **(C, H, M)** the corresponding polar histogram; **(D, I, N)** the heat map for PA signal after masking to isolate the TM and filtering; and **(E, J, O)** the corresponding polar histogram relative to maximum signal intensity. Scale bar= 3mm.

### *4.4.5 Correlation of MSC Distribution Between US-PA and Fluorescent Images*

We next quantified the overall agreement between AuNS-MSC signal as determined from US-PA and fluorescent images. The US-PA and fluorescent signal intensities in the TM region were summed over the entire 360° circumference of the eyes. We cross-plotted the fluorescent signal against the PA signal in the corresponding eye and performed a linear least-squares regression to determine whether a correlation existed between these two signals (Figure 15).

First, comparing only no cell and 250k (n=3 for each) images, a strong, significant correlation was found ($R^2$ = 0.87, Figure 15A). Second, adding in 500k images (n=3), the $R^2$ value was decreased to 0.70 but the correlation was still significant (Figure 15B). Lastly, when the 1000k images (n=3) were incorporated, US-PA and fluorescent were no longer in agreement, as evident by the low $R^2$ value (Figure 15C). It was clear that lack of correlation between the two imaging modalities only occurred when large numbers of AuNS-MSCs were delivered into the TM.

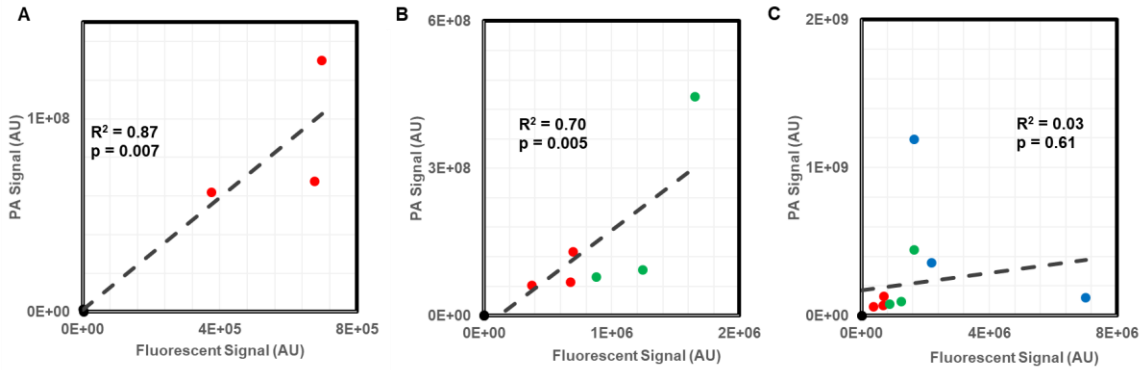


**Figure 15. Comparison between US-PA and fluorescent imaging modalities for AuNS-MSC signal in the TM region. (A – C)** Scatterplots of photoacoustic signal vs. fluorescent signal arising from AuNS-MSCs. Each data point represents the total signal in the entire TM region. Plots show the different cell injection amounts: **(A)** 250k and no cell, **(B)** 500k, 250k, and no cell, and **(C)** 1000k, 500k, 250k, and no cell (n = 3 for each

group). Significant linear correlations ($p < 0.05$) were observed for each plot as determined by student's t-distribution.

## 4.5 Discussion

MSCs have the potential to treat ocular hypertension, i.e. TM dysfunction, in glaucoma patients. Clinical translation of such an approach will require MSCs to be efficiently delivered to the TM. Previous studies in which cells were injected into the anterior chamber and then passively carried to the TM by aqueous humor outflow showed that stem cells were undetectable in the TM after only 4 days, or showed significant stem cell delivery to unwanted sites, such as the cornea and iris (Manuguerra-Gagne et al., 2013; Roubeix et al., 2015). This suggests that MSC delivery in the anterior eye is a complex process.

Understanding the factors controlling stem cell delivery is made more challenging by the fact that delivery can currently only be assessed by histologic preparations at single, set time points. Thus, development of new stem cell-based therapies for ocular hypertension would greatly benefit from improved imaging to assess stem cell delivery longitudinally. One possible option, US-PA imaging, offers the possibility of non-invasive, non-destructive, longitudinal imaging of the same sample, which is simply not possible with standard histology and fluorescent microscopy. Here, we demonstrate the potential of US-PA imaging to track MSCs in the anterior segment.

The movement of injected AuNS-MSCs due to gravity and fluid flow in the anterior chamber could be visualized by single wavelength US-PA imaging during MSC delivery into the anterior chamber and for the first 15 minutes after injection. However, within fifteen minutes after injection, the PA signal of AuNS-MSCs became too low to detect, relative to high background signals from melanin-containing tissues in the anterior segment. AuNS-MSCs may have moved out of view in the anterior chamber,

collected on tissue surfaces, reached the TM, or leaked out of the injection site. However, tracking AuNS-MSC delivery immediately after injection showed cells falling towards the lens, suggesting passive flow of aqueous humor is not sufficient for efficient delivery of cells to the TM.

We therefore turned to spectroscopic photoacoustic (sPA) imaging to distinguish AuNS-MSCs from endogenous absorbers. By using spectral sweeps, the unique spectral signatures of AuNS-MSCs and of melanin allowed the PA signals from these two sources to be separated, which improved the detection of AuNS-MSCs after they traveled to melanin-rich regions. This signal separation (unmixing) approach proved to be feasible in all eyes tested, suggesting it is a robust approach. However, this still needs to be assessed before transitioning to *in vivo* experiment due to hemoglobin from blood in the anterior segment, another endogenous absorber.

Five hours after MSC injection into the anterior chamber, sPA imaging was able to detect MSCs in the anterior segment. As the initial 15-minute delivery results suggested, most MSCs had settled under gravity onto tissue surfaces, primarily the anterior surfaces of the iris and lens. Further, sPA imaging could be used to acquire 3D images of the entire anterior segment, which allowed for non-invasive monitoring of MSC delivery and the distribution of MSCs. Specifically, these images showed extensive coating of the lens by MSCs, while the iris was only coated in certain regions, suggesting segmental outflow. MSCs engrafting onto or into the lens could lead to loss of lenticular optical clarity and reduced vision, a serious complication of stem cell therapy. These results demonstrate the utility of sPA imaging for monitoring and optimizing stem cell delivery to the TM.

A common approach for assessing cell delivery in pre-clinical trials is fluorescence microscopy of labelled cells. Disappointingly, US-PA and fluorescent imaging resulted in generally poor AuNS-MSCs signal distributions in the TM, with dissimilar trends between the two imaging modalities. We need to identify and reduce the sources of this discrepancy before US-PA imaging is used in actual regenerative medicine experiments. One possible source of discrepancy is improper registration of eye orientations between the two imaging modalities. Another possible source is uncertainty in selecting the TM region. In fluorescent imaging, the corneal margin was used as a landmark for selecting the TM, while PA imaging utilized the melanin signal associated with the TM. Since different anatomical landmarks were used, TM selection may not have been consistent, which would lead to variation.

In whole eyes, US-PA imaging of the TM would require signals to pass through the sclera or cornea, whereas we carried out US-PA imaging of the TM on dissected anterior segments in which no intervening tissue was present. We adopted this approach because it was the only viable option for fluorescent microscopy, due to limitations of light penetration into tissue. This approach thus represents a “best case” for US-PA imaging, since photons were not attenuated by the sclera or redirected away from the TM towards the lens by the cornea, as would occur when the exciting light was delivered from outside the eye. In a clinical setting, care would need to be taken to optimally target light to the TM. One approach would be to use a gonio lens, which refracts light toward the iridocorneal angle and which is routinely used for laser trabeculoplasty and visualization of angle structures in the clinic (Barkana and Belkin, 2007; Ho et al., 2009; Masihzadeh et al., 2013). With proper light delivery to the TM by developing a custom system or adopting clinically used technologies, longitudinal, non-invasive imaging for US-PA imaging is a real possibility.

In order to track delivery, MSCs were labeled with AuNS, since they are known to be efficient absorbers for PA imaging. While AuNS do not affect MSC viability and function (Ricles et al., 2011), they are known to accumulate heavily in the kidneys following AuNS intravenous injection *in vivo*, resulting in nephrotoxicity (Aillon et al., 2009; Boisselier and Astruc, 2009; Khlebtsov and Dykman, 2011). This is less of a concern when using a relatively small number of nanoparticle-labeled cells, since the total AuNS burden would be lower than following a systemic injection. Nonetheless, AuNS toxicity is still a possible limitation that needs to be monitored as this work is translated to *in vivo* experiments. Ideally, the PA imaging approach presented herein would be clinically translatable for longitudinal monitoring of stem cell therapies as a routine part of the therapy. If this is not possible, for example due to toxic side-effects, US-PA imaging can still provide a valuable pre-clinical research platform for understanding and optimizing stem cell delivery to the TM.

These initial experiments have highlighted an additional challenge for TM regenerative medicine, namely inefficient delivery of AuNS-MSCs to the TM and non-specific delivery to other anterior segment tissues. To improve TM delivery, we recently began investigating Prussian blue nanocubes (PBNCs), exogenous PA absorbers with an iron oxide core, that allow MSCs to be magnetically steered to the TM with good efficiency and specificity (Snider et al., 2018). Our US-PA imaging results can be combined with these magnetic particles to improve delivery efficiency towards the TM.

## 4.6 Conclusions

US-PA imaging has the potential to image delivery of suitably-labelled stem cells to the TM non-invasively and in real time. Specifically, by using spectroscopic PA imaging, AuNS-MSCs were distinguishable from background PA signals from melanin-

containing tissues up to 5 hours post-delivery. Further, US-PA imaging was generally consistent with MSC distributions obtained by conventional fluorescent microscopy. Next steps include implementing an improved light delivery setup to facilitate *in vivo* imaging, and longitudinal studies to confirm that US-PA imaging can track MSCs in the TM over multiple weeks.

## 4.7 Acknowledgments

This work was supported by the Georgia Research Alliance and performed in part at the Georgia Tech Institute for Electronics and Nanotechnology, a member of the National Nanotechnology Coordinated Infrastructure, which is supported by the National Science Foundation (Grant ECCS-1542174

# CHAPTER 5. Improving Mesenchymal Stem Cell Delivery to the Trabecular Meshwork Using Magnetic Nanoparticles

This chapter is a manuscript that will be submitted to Scientific Reports with the following author list: E.J. Snider, K.P. Kubelick, K. Tweed, R.K. Kim, K. Gao, A. Read, S. Emelianov, C.R. Ethier

---

## 5.1 Abstract

Glaucoma is a major cause of blindness and is associated with elevated intraocular pressure. The trabecular meshwork (TM), the tissue that primarily regulates intraocular pressure, is known to have reduced cellularity in glaucoma. Thus, stem cells offer a novel therapeutic route for glaucoma if properly delivered to the TM. For this purpose, targeted delivery of stem cells to the TM is desired. Here, we used magnetic nanoparticles (Prussian blue nanocubes [PBNCs]) to label mesenchymal stem cells and to magnetically steer them to the TM following injection into the eye's anterior chamber. PBNC-labeled stem cells showed increased delivery to the TM vs. unlabeled cells after as little as a 15-minute exposure to a magnetic field. Further, PBNC-labeled mesenchymal stem cells could be delivered to the entire circumference of the TM, which was not possible without magnetic steering. PBNCs did not affect MSc viability or multipotency. We conclude that this labeling approach allows for a targeted, relatively high efficiency delivery of stem cells to the trabecular meshwork in clinically translatable time-scales, which are necessary steps towards regenerative medicine therapies for control of ocular hypertension in glaucoma patients.

## Introduction

Glaucoma is a leading cause of blindness, affecting over 70 million people worldwide. Its incidence is expected to continue to rise as the population ages (Cook and Foster, 2012; Quigley and Broman, 2006). The best-established risk factor for glaucoma is elevated intraocular pressure (IOP), which is determined by the rate of aqueous humor production within the eye and the subsequent outflow of aqueous humor through drainage pathways in the anterior eye (Weinreb and Khaw, 2004). The primary aqueous humor drainage route is known as the conventional pathway, consisting of the trabecular meshwork (TM), Schlemm's canal, and, eventually, the circulatory system (Fautsch and Johnson, 2006; Goel et al., 2010).

In glaucoma patients, the cellularity of the TM is reduced (Alvarado et al., 1984; Baleriola et al., 2008; Gonzalez et al., 2006; Liton et al., 2005). The TM, along with the inner wall of Schlemm's canal, is known to be the major site of outflow resistance. Further, TM cells phagocytose debris from aqueous humor to prevent outflow blockage and are contractile, which can change outflow resistance (Buller et al., 1990; Llobet et al., 2003; Sherwood and Richardson, 1988). Thus, reduced TM cellularity presumably leads to tissue dysfunction and subsequent increased outflow resistance and elevated IOP. Therapies focused on restoring TM cellularity and function could therefore offer a therapeutic benefit to glaucoma patients.

Towards this end, regenerative medicine therapies are being developed for the glaucomatous TM. Most existing studies have used fibroblast-derived induced pluripotent stem cells (iPSCs) or mesenchymal stem cells (MSCs) (Abu-Hassan et al., 2014b; Ding et al., 2014; Manuguerra-Gagne et al., 2013; Roubeix et al., 2015; Zhu et al., 2016a). While each of these studies show the potential for regenerating the TM,

delivery of cells after injection into the anterior chamber has relied on the stem cells being passively carried by aqueous humor outflow to the TM. Passive delivery of stem cells has led to inconsistent MSC delivery to the TM and non-specific delivery to other anterior ocular tissues (Manuguerra-Gagne et al., 2013; Roubeix et al., 2015). Cell delivery to sites other than the TM is undesirable since stem cells may differentiate to undesired phenotypes in tissues such as the lens or cornea.

Passive delivery is further complicated by aqueous humor outflow dynamics. Outflow from the TM is known to be non-uniform (segmental) around the TM circumference (Swaminathan et al., 2014). Indeed, studies indicate that as little as one-third of the TM is actively filtering at any one time (Chang et al., 2014), suggesting that passively delivered stem cells could integrate into as little as one-third of the TM. Such an outcome is presumably sub-optimal, since active filtering regions may change over time. Further, outflow is more segmental in glaucomatous patients than in unaffected individuals (de Kater et al., 1989), so that this problem is even worse in the target patient population.

To improve on conventional (passive) delivery, we propose to use magnetic nanoparticles to label MSCs and to then steer them to the TM using a magnetic field. Superparamagnetic iron oxide nanoparticles (SPIONs) have previously been used for targeted cell delivery to the retina (Ito et al., 2005; Yanai et al., 2012). For this study, we use Prussian blue nanocubes (PBNCs), which combine Prussian blue pigment with SPIONs (Cook, 2017). The SPION core gives PBNCs magnetic properties that allow magnetic steering, while the Prussian blue pigment makes the particles strong absorbers of near-infrared light. We recently demonstrated that ultrasound-photoacoustic non-invasive imaging can visualize anterior segment tissues, as well as the delivery of cells labelled with PBNCs (Kubelick et al., 2017, in preparation). Here, we ask the question as

to whether PBNCs are suitable for MSC labeling and can improve MSC delivery to the TM.

## 5.2 Methods and Materials

### *5.2.1 Mesenchymal Stem Cell Sourcing*

Human adipose derived mesenchymal stem cells (MSCs, Lonza) were grown in α-minimum essential medium supplemented with 20% fetal bovine serum (FBS), penicillin, streptomycin, and L-glutamine. At 80-90% confluency, MSCs were detached using 0.05% Trypsin-EDTA (w/v, Cellgro, Corning) and seeded in fresh cell-culture T75 flasks at a seeding density of 5,000 cells/$cm^2$. In all experiments, MSCs were used at passage numbers five or six. Each MSC donor strain was validated by Lonza for expression of MSC surface markers (CD13, CD29, CD44, CD73, CD90, CD105, and CD166) and minimal expression of negative MSC markers (CD14, CD 131, CD45). We also previously characterized each MSC donor strain for adipogenic, chondrogenic, and osteogenic differentiation and CD90 expression following expansion (Snider et al., 2017).

### *5.2.2 PBNC Nanoparticle Synthesis and Characterization*

PBNCs were synthesized according to methods described previously (Cook, 2017). 150 mL of 0.04% (w/v) dextran-coated iron oxide ($Fe_3O_4$) nanoparticles (Ocean NanoTech) in deionized ultra-filtered water were vigorously mixed with 5 mL of 5% w/v potassium hexacyanoferrate(II) trihydrate ($K_4Fe(CN)_6 \cdot 3H_2O$, Sigma-Aldrich). After one minute, 2.496 mL of 1.85% (v/v) hydrochloric acid (HCl, Sigma-Aldrich) was added. To alter PBNC size, the diameter of the iron oxide nanoparticles was altered. Dextran-coated iron oxide nanoparticles with a diameter of 10nm produced 200nm PBNCs. Iron

oxide nanoparticles with a diameter of 2nm produced 20nm PBNCs. Transmission electron microscopy (TEM) (Hitachi HT7700 TEM, IEN/IMAT Materials Characterization Facility, Georgia Institute of Technology) was used to visualize particle size and shape (Figure 16). PBNCs were sterilized under UV light for at least 12 hours prior to all experiments.

For estimating iron content in 200 and 20nm PBNCs, particle counts were measured from transmission electron micrographs at a known optical density (as determined by UV-Vis spectrophotometry). Based on the initial iron content used to synthesize particles and assuming particle concentration increases with optical density, it was determined that 200nm PBNCs have 2.8 times the iron content of 20nmPBNCs at the same optical density.

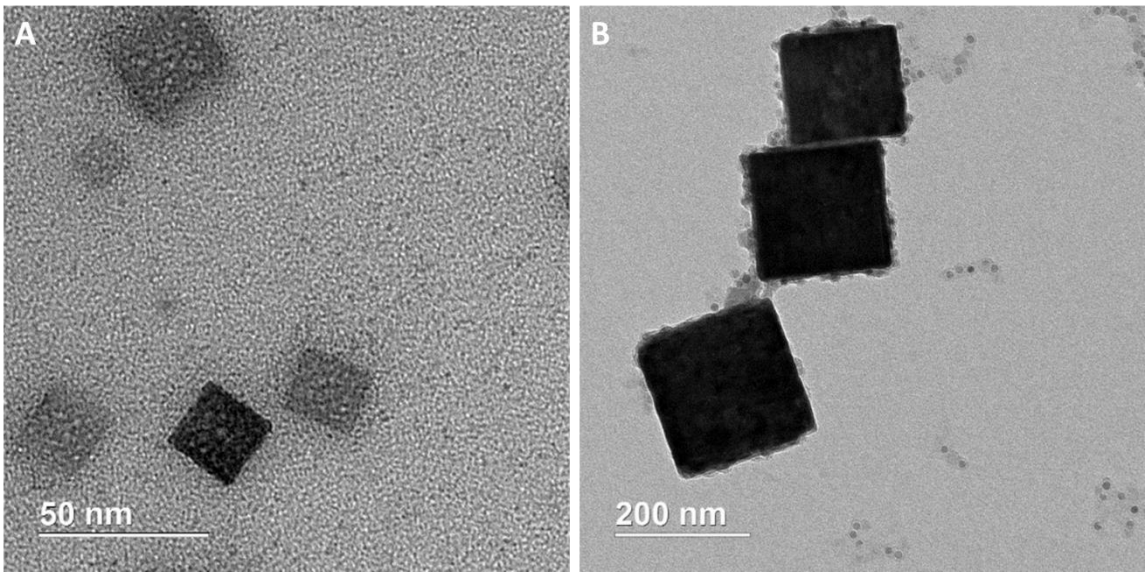


**Figure 16. TEM Characterization of PBNCs.** Representative transmission electron micrographs for **(A)** 20nm PBNCs and **(B)** 200nm PBNCs to determine approximate shape and size.

### *5.2.3 MSC Fluorescent and PBNC Labeling*

MSCs at 80-90% confluence were incubated with PBNCs in cell culture media at PBNC concentrations ranging from 0.25 to 10 optical density (OD) for 24 hours. Unless otherwise noted, 2 OD PBNC concentrations were used in experiments reported herein. Uptake of PBNCs by MSCs was visually detected within cells by light microscopy (EVOS XL, Thermo-Fisher). Prior to imaging, PBNC-labeled MSCs (hereinafter referred to as PBNC-MSCs) were fixed with 10% buffered formalin for 15 minutes followed by cytoplasmic staining with 1% eosin (w/v) for 5 minutes. Triplicate experiments were performed for each PBNC incubating concentration to confirm PBNC uptake, which we defined as PBNC colocalization with eosin-stained cytoplasm. Further characterization of PBNC-MSCs was performed by flow cytometry to assess changes in light scatter known to correlate with nanoparticle uptake (Zucker et al., 2010). Specifically, labeled MSCs were detached from culture dishes with 0.05% trypsin-EDTA (w/v) and side scatter (SSC) properties were analyzed using an Attune NxT (Thermo-Fisher) flow cytometer at 200 µL/min flow rates.

A Vevo 2100 imaging system, which incorporates ultrasound and photoacoustic (US/PA) imaging modalities (VisualSonics, Inc.), was used to verify that PBNC-MSCs could produce a photoacoustic signal. PBNC-MSCs were imaged in a tissue-mimicking gelatin phantom (Cook et al., 2011). The base of the phantom consisted of 8% (w/v) gelatin and 0.2% (w/v) silica (Sigma-Aldrich). Gelatin phantom inclusions were made by adding 16% (w/v) gelatin to an equal volume of PBNC-MSCs. Each inclusion was imaged at 5nm wavelength increments from λ=680 nm to 970 nm with the US/PA transducer oriented perpendicular to the gelatin base.

For MSC injection experiments, MSCs were detached from culture flasks with 0.05% trypsin-EDTA (w/v), centrifuged, and resuspended in 5uM carboxyfluorescein succinimidyl ester (CFSE, affymetrix eBioscience) in PBS after PBNC uptake (for PBNC-MSC samples). After incubating for 15 minutes at 37$^{o}$C, media was added to quench any unreacted CFSE before injection of MSCs into the eye.

### *5.2.4 Organ Cultured Porcine Eyes*

Anterior segment organ culture is a well-established method to maintain trabecular meshwork function *ex vivo* for several weeks, and we adopted this approach for our work here (Bachmann et al., 2006; Bhattacharya et al., 2009; Erickson-Lamy et al., 1991; Johnson and Tschumper, 1987, 1989). Fresh porcine eyes from a slaughterhouse (Holifield Farms, Covington, GA) were dissected within 6-8 hours of enucleation. Eyes were dissected to isolate the outflow tissues and anterior corneoscleral shell, similar to previously reported methods (Bachmann et al., 2006; Bhattacharya et al., 2009). Briefly, orbital connective tissue was dissected away and eyes were soaked in Betadine (Purdue Pharma) solution for 5 minutes, after which eyes were transferred to a sterile laminar flow hood for the remainder of the process. Eyes were washed with sterile PBS, and hemisected with a razor blade to isolate the anterior half of the eye. The vitreous humor and lens were removed. Next, the iris was cut radially back to the iris root and pectinate ligaments until the TM was revealed. The ciliary processes were then carefully removed while preserving the TM. Any remaining vascularized or pigmented tissue was removed from scleral and cornea surfaces with sterile cotton swabs.

Dissected anterior segments were placed in custom-built organ culture dishes and clamped in place (Figure 17). Organ culture dishes were placed in a sterile 37$^{o}$C

humidified incubator and perfused at 2.5 µL/min with serum-free media containing penicillin, streptomycin, and amphotericin while pressure transducer (142pc01g, Honeywell) readings from the anterior segment were recorded every 60 seconds in LabView. Eyes were stabilized for at least 48 hours before conducting any experiments. Any eye which did not demonstrate a stable outflow facility (the ratio of perfusion flow rate over IOP) between 0.45 and 0.125 µL/min/mmHg (pressures of ~6mmHg to 20mmHg IOP) were considered as outliers and not used for MSC delivery experiments (Figure 17).

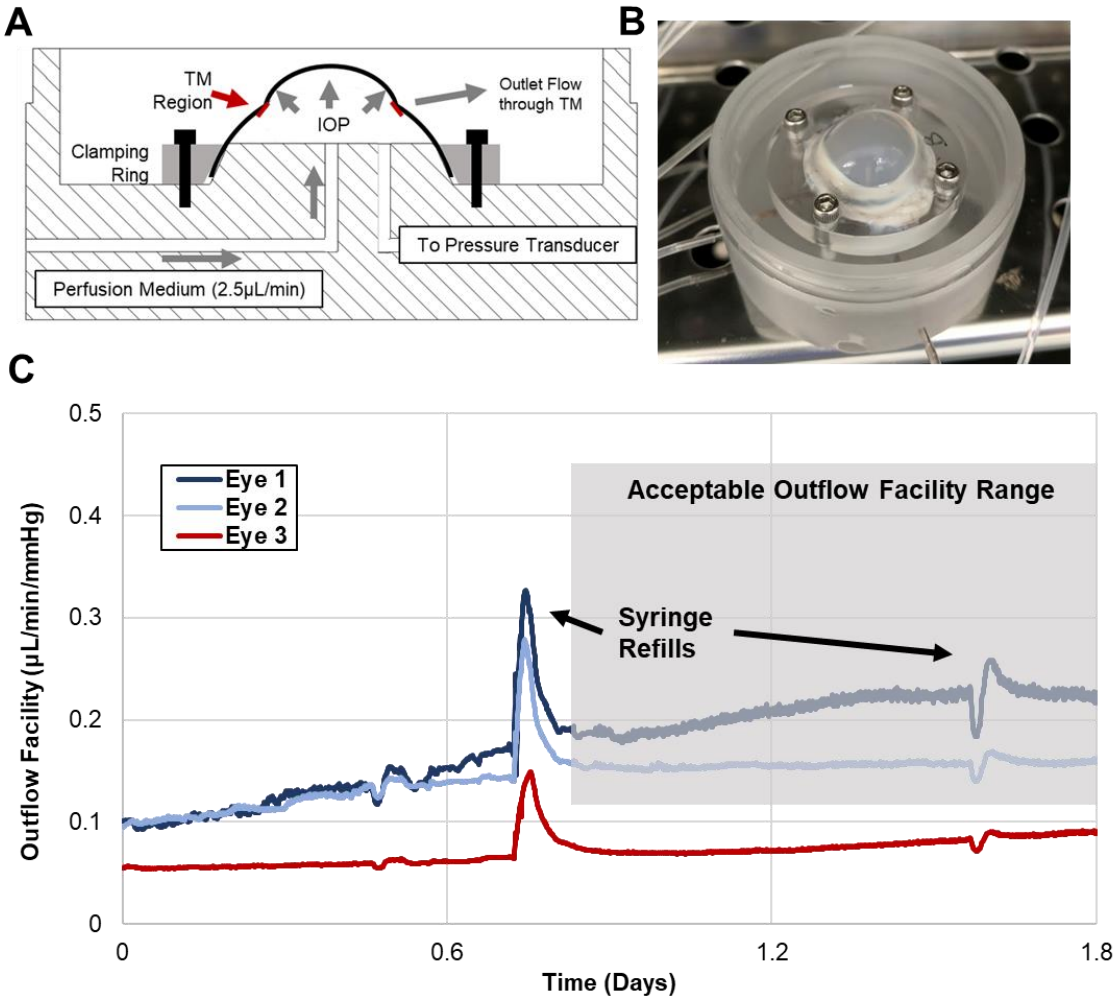


**Figure 17. Anterior Segment Organ Culture Setup. (A)** Diagram of porcine anterior segment clamped in organ culture dish. Red label indicates TM region. **(B)** Porcine

anterior segment in organ culture after 10 days of perfusion. **(C)** Representative outflow facility traces for three porcine eyes. Outflow facility stabilizes after 1-2 days, after which any eyes with outflow facilities outside of the acceptable range are not considered for injection experiments (such as Eye 3).

### *5.2.5 PBNC-MSC magnetically steered delivery*

PBNC-MSCs were detached from culture flasks using 0.05% trypsin-EDTA (w/v) and counted to determine cell number (Attune NxT Flow Cytometer). After fluorescent staining with CFSE, cells were resuspended in serum-free organ culture media at 1 million cells/mL. 250µL of cell suspension was injected with a 31-gauge needle through the cornea (5-10 second injection duration) while anterior segments were pressure clamped at 8 - 12 mmHg. Immediately after injection, anterior segments were again perfused at 2.5µL/min. For magnetic delivery experiments, cells were steered in one of two ways.

1) For initial optimization experiments, neodymium rare earth bar magnets (0.75” length x 0.25” width x 0.25” height) were placed next to one quadrant of the anterior segments near the limbal (corneal-scleral border) region prior to MSC injection.

2) For 360$^{o}$ delivery experiments, two different ring magnets were used (Figure 20). First, a 3D-printed magnet holder containing 10 axially-polarized cylindrical magnets (3/16” diameter x 0.25” height) was created (referred to as Design I). Alternatively, a commercially available axially polarized ring magnet (1.5” outer diameter x 0.75” inner diameter x 0.25” height) was used (referred to as Design II). Ring magnets were placed around the limbus before MSC injections and removed at specified time points.

Following MSC injection, anterior segments were perfused overnight, after which they were removed from organ culture and immersed in 10% buffered formalin overnight (4$^{o}$C) to fix tissue.

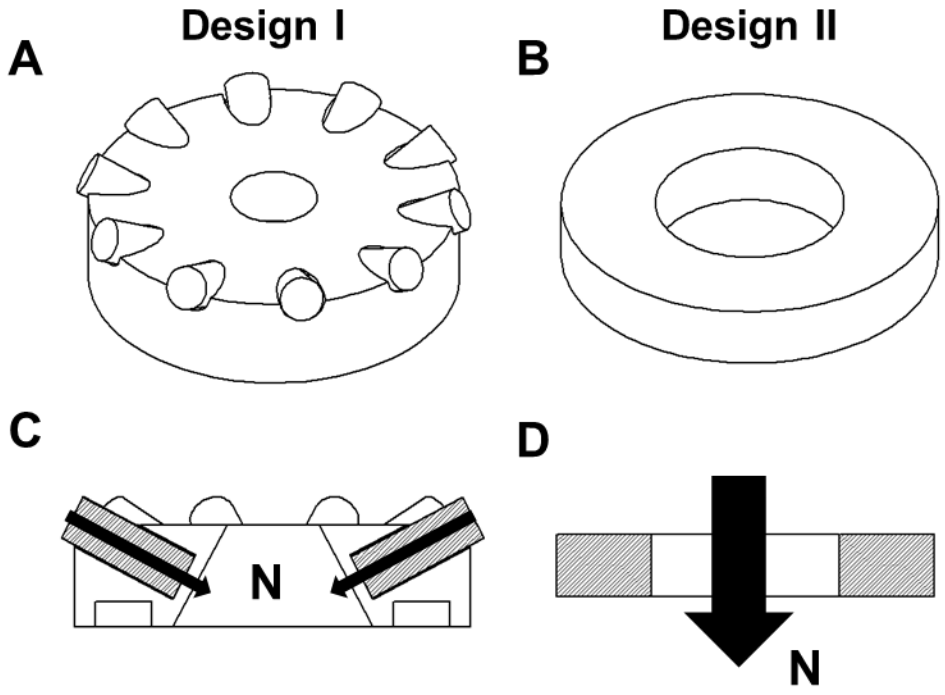


**Figure 18. Schematics of Ring Magnets.** Overview **(A, B)** and cross-sectional **(C, D)** views for two ring magnet designs used. **(A, C)** Design I: A 3D-printed ring magnet holder housing 10 cylindrical magnets. **(B, D)** Design II: An axially polarized ring magnet. Arrows denote overall magnetic field direction towards the north pole (N).

### *5.2.6 Fluorescent microscopy and quantification*

After fixation, the TM region of anterior segments was fluorescently imaged *en face*. Anterior segments were placed in PBS on a 50mm glass bottom dish, after scleral surfaces posterior to the TM were removed so that the TM was in contact with the dish surface to improve imaging. Micrographs of the entire TM circumference were captured by confocal microscopy (LSM 700, Carl-Zeiss) to identify CFSE-tagged MSCs delivered to the TM region. Brightfield overlays were also captured to identify the corneal margin and hence the approximate location of the TM. Micrographs were captured at 50x magnification as z-stack tile scans to account for TM depth and height differences

around the circumference of the anterior segment. Maximum intensity projections were created for each *en face* image for use in further image quantification.

To specify the TM region within which quantification was carried out, masks were created from brightfield images using the corneal margin as a landmark (Figure 19). A 1mm ring from the edge of the cornea was defined, using ImageJ (Schindelin et al., 2015; Schneider et al., 2012), to be the TM region within each image. Images were further processed in Matlab (MathWorks) to remove large fluorescent debris (size greater than 100 µm). To quantify fluorescent intensity around the TM circumference, a polar coordinate system was overlaid onto images and the total CFSE intensity was quantified within each one degree sector. Intensities were then summed over 30$^{o}$ sectors, resulting in 12 intensity values for each image. The process was then repeated, considering only the signal outside the masked region, to determine the cell signal not located in the TM.

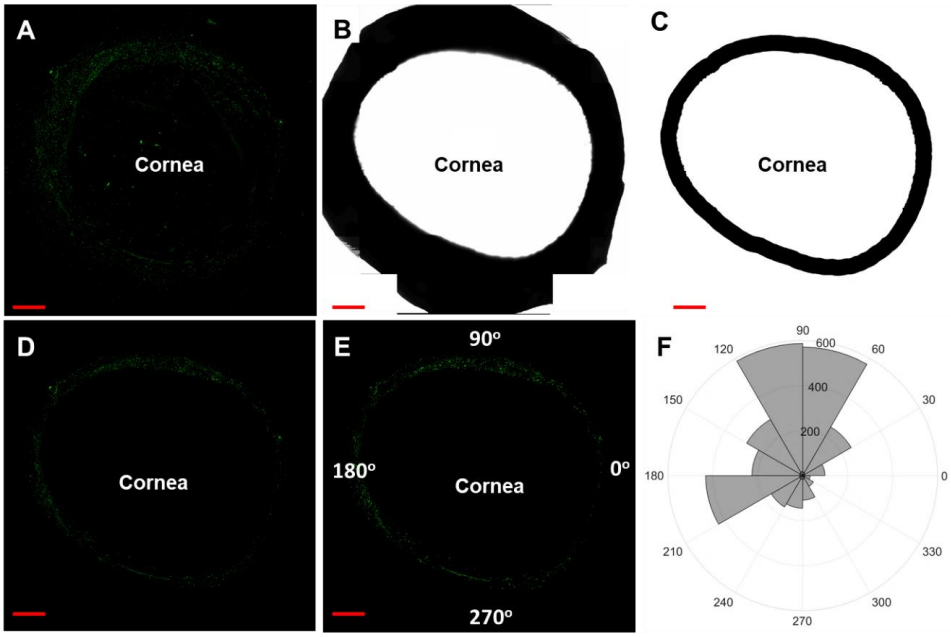


**Figure 19. Example of Image Processing for *en face* Micrographs. (A)** Raw fluorescent *en face* micrograph showing CFSE-labeled MSCs in green. **(B)** Brightfield *en*

*face* image used for determining the TM location. **(C)** A 1-mm wide ring around the cornea is used to identify CFSE-labeled MSC signal within **(D)** the TM tissue region. **(E)** Fluorescent debris larger than 100µm was excluded and **(F)** polar histograms were created, showing CFSE-labeled MSC signal (radial coordinate, arbitrary units) within the TM as a function of circumferential location. Scale bars denote 2mm.

### *5.2.7 Histology*

Anterior quadrants of fixed porcine eyes were cut into 3 mm wide meridional wedges and trimmed to isolate the outflow region. The tissue was dehydrated through an ethanol series, infiltrated and embedded in Histocryl media (Electron Microscopy Sciences). Two micron thick sections were cut on a Leica UC7 ultramicrotome with a glass knife and examined with a Leica DM6 Epifluorescent microscope. Sections were examined to visualize stem cells labeled with PBNCs, using the green fluorescent protein filter cube.

### *5.2.8 Live-Dead Assessment of Effects of PBNCs on MSCs in vitro*

To assess potential acute toxicity due to PBNCs, MSCs were incubated with PBNCs at various concentrations for 24 hours. Media was removed and propidium iodide was added to each sample for 5 minutes to stain dead, adherent cells. Propidium iodide staining solution was removed and 0.05% trypsin-EDTA (w/v) was added for 5 minutes to detach cells. Media containing 20% FBS was added to neutralize trypsin activity and cells were collected in deep-well 96-well plates (Corning). Cell samples were processed by flow cytometry by collecting equal volumes from each sample (Attune NxT). PBNC-labeled living cell counts (propidium iodide negative), were compared to unlabeled, control living cell counts to determine PBNC toxicity 1 day after PBNC incubation. This approach bypassed the issue of tracking detached, dead cells in vitro and determined only how many less living cells were present relative to unlabeled controls.

To assess longer-term toxicity following PBNC incubation, DAPI-stained nuclei were counted from microscopic images 7 and 21 days after PBNC incubation at different PBNC concentrations. These cells were the same ones used in assessment of MSC multipotency (see section 5.2.8). Nuclei counts were compared to counts in cells that had not been exposed to PBNCs.

Finally, we assessed whether magnetic fields might interact with PBNCs to lead to cell toxicity. MSCs in 48 well plates labelled with 200nm PBNCs at a concentration of 2 OD were placed on neodymium rare earth magnets (0.5” length x 0.5” width x 0.25” height) for 15, 30, 60 minutes or overnight. Unlabeled MSCs were also exposed to the same magnetic field to determine the toxicity of the magnetic field alone. After magnet exposure, MSCs were stained with propidium iodide and detached for flow cytometric analysis as described above. PBNC-labeled and unlabeled MSC counts for each magnet duration were compared to counts of control cells that were not exposed to magnetic fields.

### *5.2.9 Stem Cell Multipotency Assessment in vitro*

We also carried out studies to ensure that PBNC labelling did not negatively affect the multipotency of MSCs. After loading with PBNCs, cells were exposed to adipogenic differentiation or osteogenic differentiation media for 1 or 3 weeks respectively, feeding every three days (Gibco). At their respective time points, cells were fixed in 10% buffered-formalin for 15 minutes. Adipogenesis was quantitatively assessed by Nile Red staining (Thermo-Fisher) (Greenspan et al., 1985). Cells were incubated for 5 minutes with 100 ng/mL Nile Red in PBS, washed, and probed with DAPI (Life Technologies). For each cell sample, 16 fluorescent micrographs were captured in a 4 x 4 array across each sample using an imaging plate reader (10x objective, BioTek

Cytation 3). Nile Red average fluorescent intensities were quantified for each image and normalized to DAPI cell counts. Further, adipogenesis was qualitatively assessed by Oil Red O (Sigma-Aldrich) staining and light microscopy (Snider et al., 2017, in preparation).

To assay for osteogenesis, cells were stained with 2% (w/v) Alizarin Red for 2 minutes followed by PBS rinses to remove excess dye. Experiments were qualitatively assessed by light microscopy, followed by counterstaining cell nuclei with DAPI, and 16 fluorescent micrographs were captured in a 4 x 4 array for each sample using an imaging plate reader as described above.

### *5.2.10 Statistics*

For *in vitro* experiments, triplicate technical replicates were run for each set of experimental conditions. Two MSC donor strains were used in assessment of viability and multipotency. Analysis of variance (ANOVA, with post hoc Tukey test) was used to determine if unlabeled, control groups were significantly different from PBNC-labeled groups. For cell delivery experiments, at least triplicate ocular injections were carried out for every experimental condition using a single MSC donor strain. Kuiper's V test was performed to test for non-uniform circumferential cellular distributions in experiments in which cells were steered by a rectangular magnet (Berens, 2009; Kuiper, 1960). Average cell signal distribution results for each group were assessed, with $p < 0.05$ indicating non-uniformity skewed toward the magnet location. For experiments in which cells were steered using a ring magnet, Rayleigh's test for uniform circular distribution was used to test cell signal distributions, with $p < 0.05$ indicating non-uniform cellular distribution around the TM (Berens, 2009).

The use of ANOVA requires three assumptions to be satisfied: the outcome of interest must be continuous and measurements must be independent; the residuals

must be normally distributed; and there must be homogenous variance between groups (“homoscedasticity”). For this study, all experimental variables were continuous. Uniform distribution and equal variances were routinely assessed as part of the ANOVA analysis (XLSTAT). Unfortunately, for situations in which there were small numbers of observations (n < 5), assessment of normality was unreliable. Further statistical analysis should be carried out to confirm the validity of these statistical tests.

## 5.3 Results

### *5.3.1 MSCs Uptake PBNCs*

MSCs were incubated with PBNCs overnight, after which cells were fixed and assessed for PBNC uptake by light microscopy. Prussian blue labelling was visible and colocalized with eosin-stained MSCs after incubation with 20nm or 200nm PBNCs (Figure 20 A-E). PBNCs are known photoacoustic absorbers (Cook, 2017), so PA imaging was performed on labeled MSCs by suspending cells in gelatin and imaging at 690 or 755 nm wavelengths for 20nm or 200nm PBNCs, respectively. PA signal was detectable and increased with the optical density (OD) of the PBNC solution used during cell labelling, i.e. with increasing PBNC concentration (Figure 20 F-J). PBNC uptake was further confirmed by flow cytometry. Specifically, MSC side scatter, a measure of light scatter due to particles inside cells (i.e. nucleus, endosomes, PBNCs), increased following labeling with PBNCs when compared to unlabeled controls (Figure 20 K,L), with increases correlating with PBNC concentration. 200nm PBNCs resulted in larger scattering effects than 20nm PBNCs (Figure 20 M). Overall, we conclude that both 20nm and 200nm PBNCs are suitable for MSC labeling, but side scatter results suggest that 200nm PBNCs yield more labeling than 20nm PBNCs.

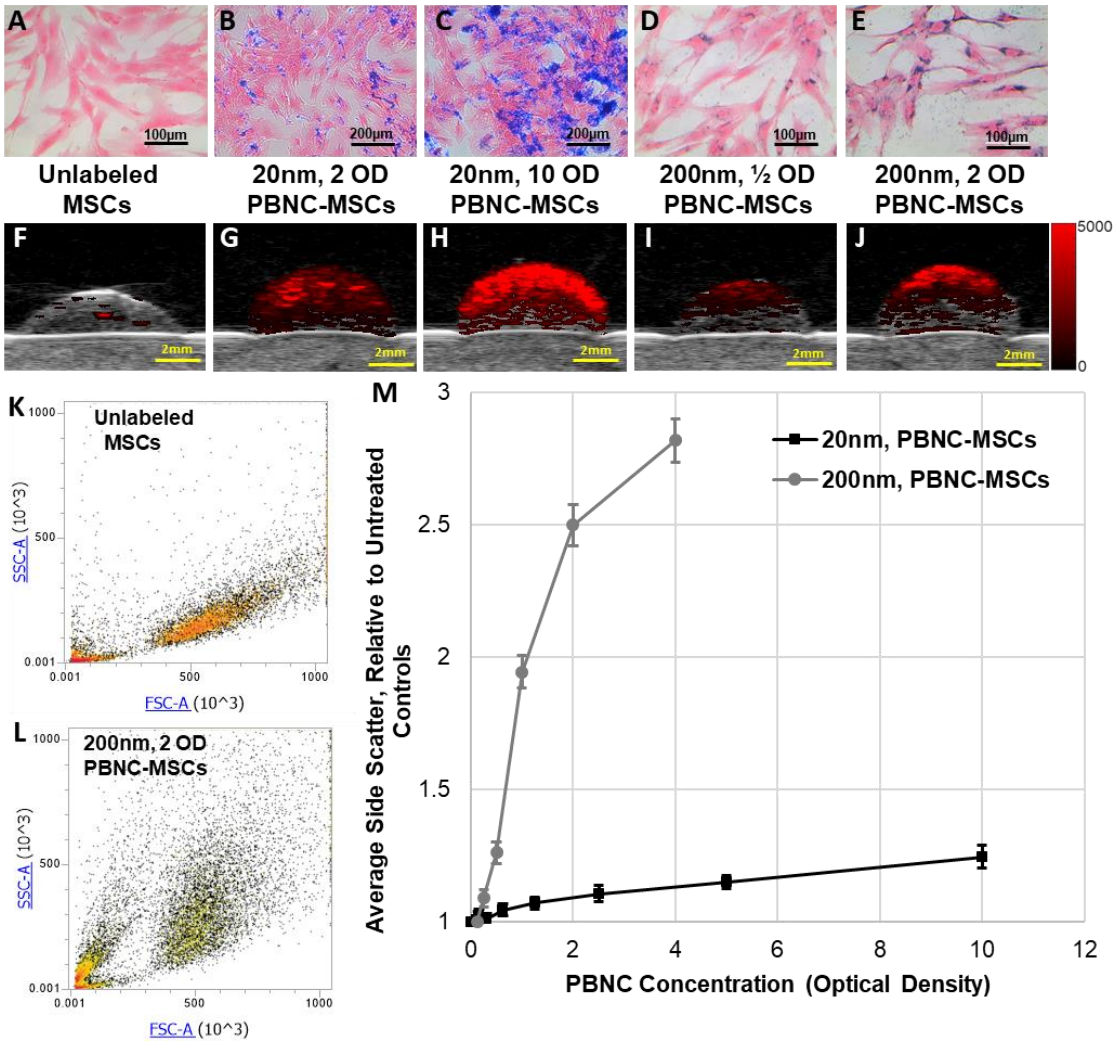


**Figure 20. MSCs Uptake PBNCs. (A-E)** Representative micrographs of MSCs after incubation with different PBNC sizes and PBNC solution optical densities (OD). MSCs were eosin stained to visualize cytoplasm, while PBNCs appear blue. **(F-J)** Photoacoustic signal at 690nm (20nm PBNCs) or 755nm (200nm PBNCs) excitation wavelength for MSCs in gelatin phantoms (both 690nm and 755nm unlabeled MSC signals were minimal so only 690nm is shown). Uptake of PBNCs was further assessed by light side scatter (SSC). **(K,L)** Representative forward scatter (FSC) vs. SSC density maps collected by flow cytometry for **(K)** unlabeled MSCs or **(L)** MSCs incubated in a solution of 200nm PBNCs at a concentration of 2OD. **(M)** Normalized side scatter vs. optical density of incubating solution for 20nm and 200nm PBNC-MSCs (n=3 technical replicates for each). Error bars denote standard deviation.

### *5.3.2 PBNC-MSCs Can Be Steered by Magnetic Fields*

Either 20 or 200nm PBNCs were used to label MSCs, and 250,000 labelled cells were injected into perfused porcine anterior segments maintained in organ culture. To establish a baseline for comparison, unlabeled MSCs were injected without an external magnet, which resulted in very few cells in the TM region (Figure 21A). It was expected that cells would be attracted to a neodymium rectangular magnet placed near the limbus in one quadrant of the anterior segment. However, when MSCs were labeled with 20nm PBNCs at a concentration of 2 OD, few cells preferentially accumulated in this quadrant (Figure 21B) when compared to the distribution of unlabeled MSCs. On the other hand, when the PBNC concentration in the incubation solution was increased to 10 OD, more MSC accumulation was detected near the magnet (Figure 21C). Finally, if cells were incubated with 200nm PBNCs at a concentration of 2 OD, a much higher number of MSCs accumulated near the magnet (Figure 21D).

The distribution of fluorescent signal from labelled MSCs around the entire TM circumference was quantified for at least 3 injection experiments for each condition and averaged, as shown in polar histograms (Figure 22). Kuiper's V tests for non-uniform cell distribution at the site of the magnet ($0^o$) demonstrated that only 20nm PBNC-MSCs incubated at a PBNC concentration of 10 OD and 200nm PBNC-MSCs incubated at a PBNC concentration of 2 OD resulted in significant cell accumulation at the magnet. While 20nm PBNC-MSCs at a PBNC concentration of 10 OD were steered to the magnet location, total cell signal at the magnet site was similar to control eyes (Figure 23). Only 200nm PBNC-MSCs at a concentration of 2 OD resulted in significantly higher fluorescent cell signal at the magnet site compared to the other experimental groups (Figure 23). Therefore, we conclude that 200nm PBNCs are optimal for improving cell delivery to the TM.

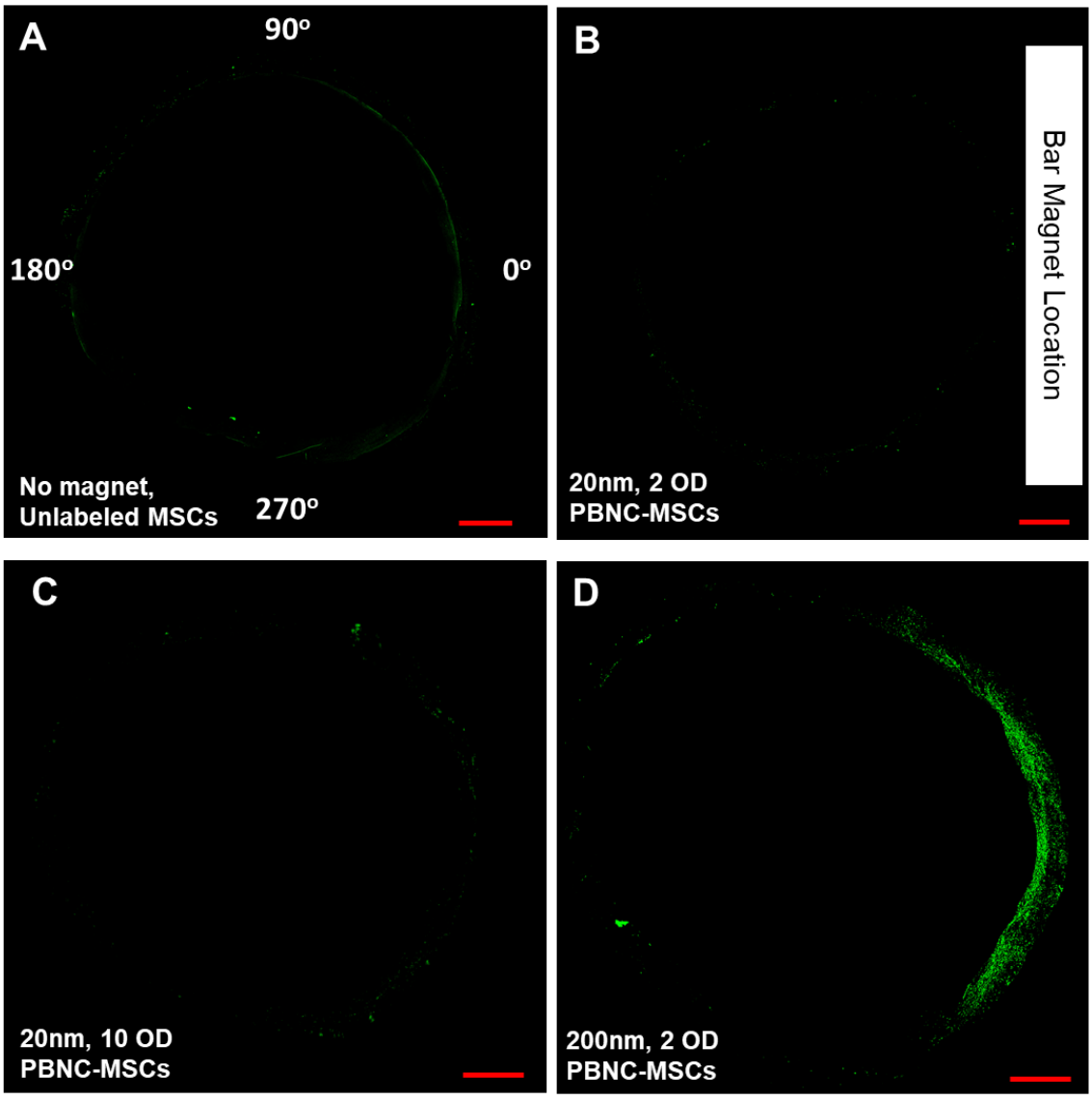


**Figure 21. Magnetic steering of MSCs labelled with either 20 or 200nm PBNCs.** Representative *en face* micrographs of the TM region after MSC delivery. Bar magnets, diagramed in (B) (to scale), were secured overnight at 0° near the limbal region in PBNC-MSC injections. CFSE-tagged MSCs (Green) were injected **(A)** unlabeled, or after incubation with **(B)** 20nm PBNCs at 2 OD **(C)** 20nm PBNCs at 10 OD, **(D)** 200nm PBNCs at 2OD. Scale bars denote 2mm.

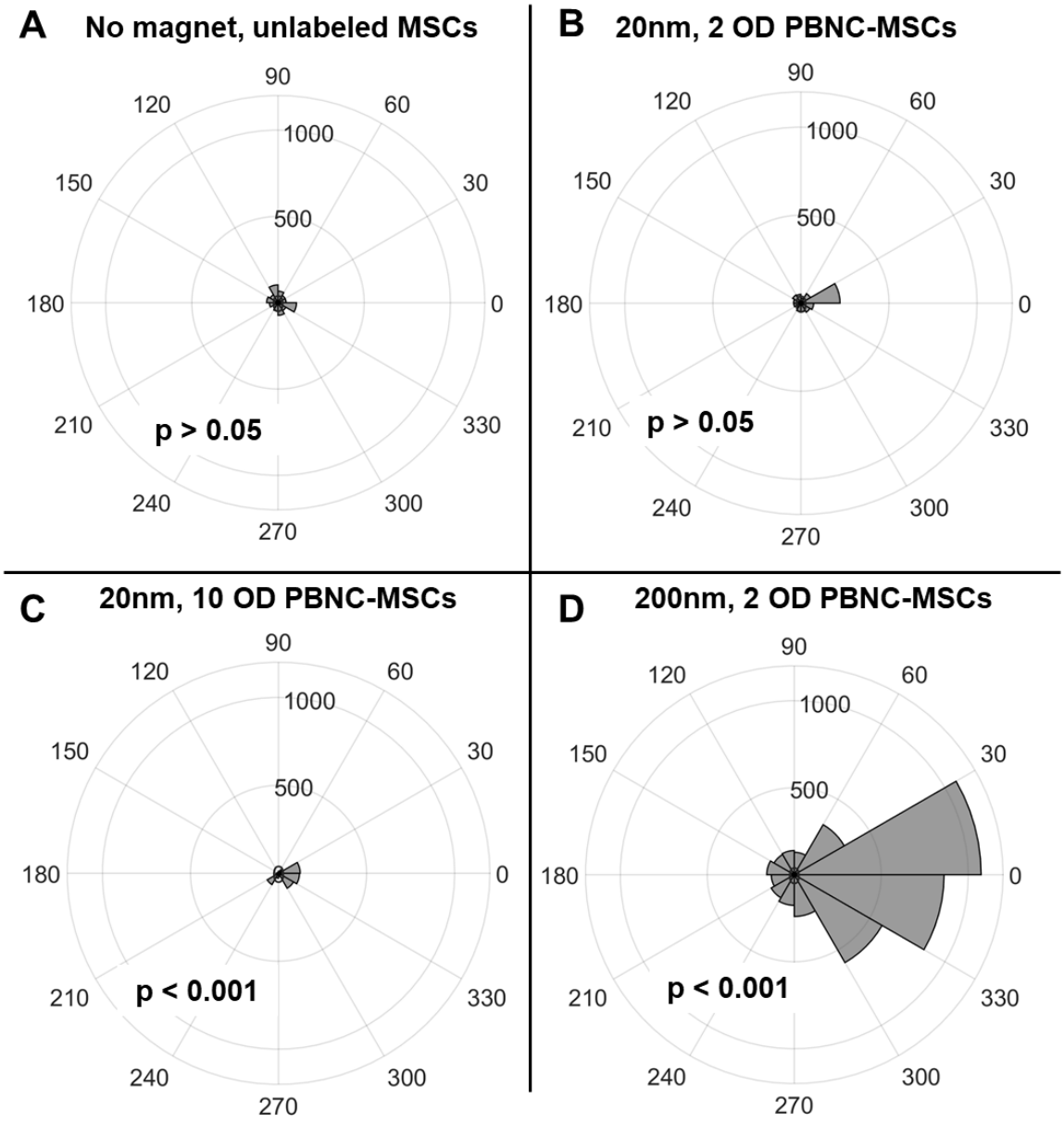


**Figure 22. Quantification of Cell Delivery to the TM for MSCs Labelled with 20 and 200nm PBNCs.** Polar histograms illustrate fluorescence intensity (radial coordinate, arbitrary units) for each 30$^{o}$ region. Note that a bar magnet was placed adjacent to the limbus at 0$^{o}$ overnight (see Figure 21B). Average results for **(A)** no magnet, unlabeled MSCs (n=5 eyes), **(B)** 20nm, 2 OD PBNC-MSCs (n=3 eyes), **(C)** 20nm, 10 OD PBNC-MSCs (n=3 eyes), **(D)** 200nm, 2 OD PBNC-MSCs (n=4 eyes) experiments are shown. p-values were calculated using Kuiper's V test to assess if distribution was non-uniformly skewed towards the center of the magnet location (0$^{o}$).

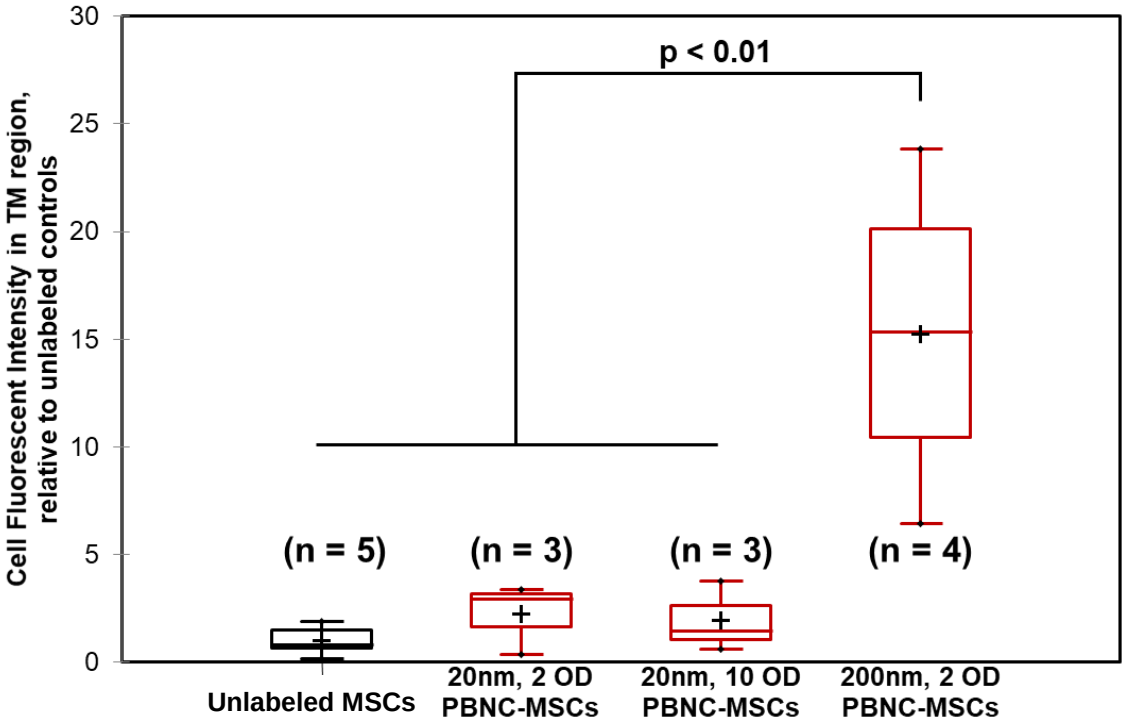


**Figure 23. MSCs incubated with 200 nm PBNCs in a solution with OD=2 are steered to the magnet.** The plotted quantity is total fluorescent signal in the TM in the magnet region, defined as the wedge extending from 45º to -45º (see Figure 21B) relative to unlabeled MSCs (mean = 1) for MSCs labeled with 20nm PBNCs at 2 OD (mean = 2.2), MSCs labeled with 20nm PBNCs at 10 OD (mean = 1.8), and MSCs labeled with 200nm PBNCs at 2 OD (mean = 14). For box and whisker data, crosses correspond to mean values while the lower, center and upper limits of the box are the first, second and third quartile. The upper and lower whiskers denote the maximum and minimum values. (Outliers, defined as 1.5x below or above the first and third quartile, respectively, are shown as single data points beyond the upper and lower whiskers when applicable) Significance ($p < 0.05$) was determined by ANOVA, with post hoc Tukey.

### *5.3.3 Optimizing Magnetic Field Exposure Time*

Next, the effect of magnet placement time was assessed using MSCs labelled with 200nm PBNCs at a concentration of 2 OD. Specifically, a bar magnet was placed adjacent to the limbus for either 15 minutes, 30 minutes, 60 minutes, or overnight (representative micrographs, Figure 24). The cell distributions near the magnet were

similar for all durations, each resulting in significant PBNC-MSC accumulation adjacent to the magnet (Figure 25).

To further quantify cell steering, total fluorescent signal in the TM within a 90$^{o}$ sector (45$^{o}$ on both sides of the magnet center at 0$^{o}$) was quantified and compared to fluorescent signal in the entire TM (Figure 26A). We found that 50 to 75% of MSCs were steered to the magnet site and that no significant differences were observed between the durations tested. Similarly, to assess how many cells were delivered to non-target tissues in the magnet region, total fluorescent signal outside of the TM was quantified, and ratios of TM to non-TM fluorescence were calculated. Higher TM specificity was observed for longer durations, with overnight magnetic exposure having the highest TM to non-TM delivery ratio (Figure 26B). However, differences in specificity between different magnetic exposure durations were not found to be statistically significant. We conclude that cell steering occurs rapidly, i.e. a 15-minute magnet placement is sufficient to steer many cells to the TM.

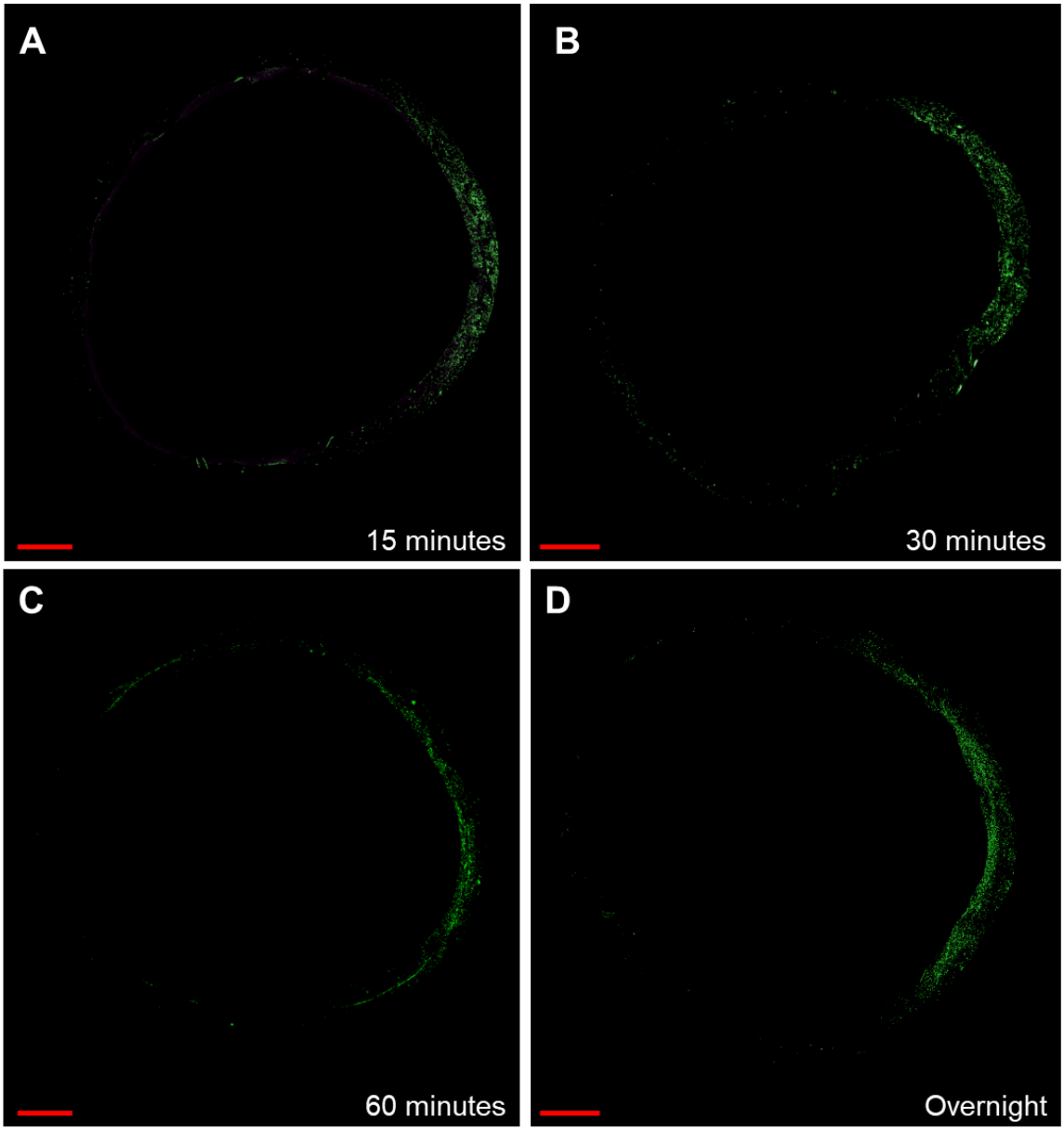


**Figure 24. Effect of Magnetic Field Exposure on Steering of 200nm PBNC-MSCs to the TM.** Representative *en face* micrographs of the TM region following MSC delivery with bar magnets placed at 0$^{o}$ near the limbal region for different durations (see Figure 21B). All anterior segments were perfused overnight prior to imaging. CFSE-tagged MSCs (Green) were pre-labeled with 200nm PBNCs at a concentration of 2 OD and exposed to a magnetic field for **(A)** 15 minutes, **(B)** 30 minutes, **(C)** 60 minutes, or **(D)** Overnight. Scale bars denote 2mm.

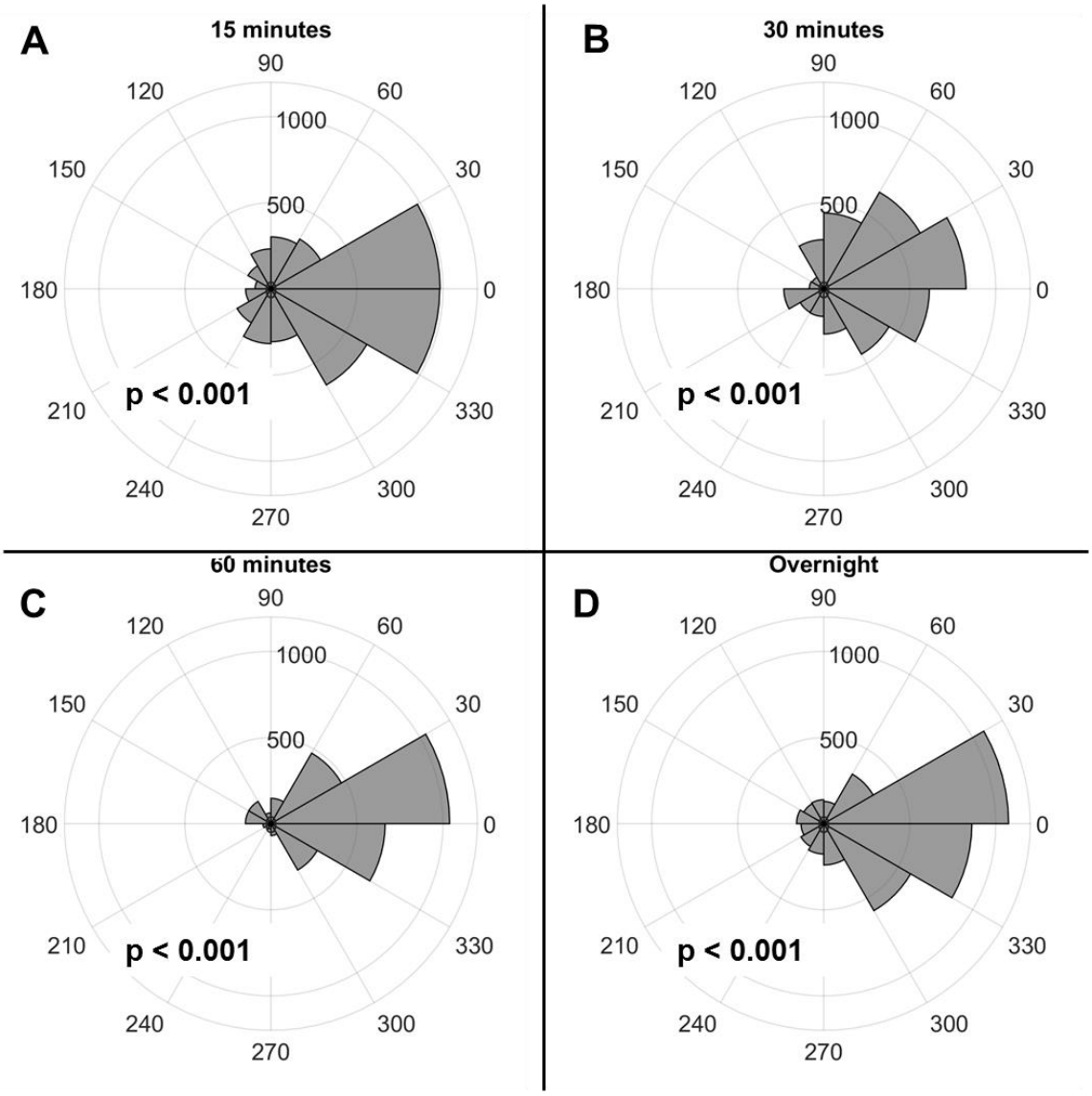


**Figure 25. Quantification of MSC Delivery After Exposure to Magnetic Fields for Different Durations.** Polar histograms illustrate fluorescence intensity (radial coordinate, arbitrary units) for each 30º region, with a bar magnet placed at 0º (see Figure 21B). Average results for **(A)** 15-minutes (n=4 eyes), **(B)** 30-minutes (n=5 eyes), **(C)** 60-minutes (n=3 eyes), and **(D)** overnight (n=4 eyes) magnet exposures are shown. p-values were calculated using Kuiper's V test to assess if distribution was non-uniformly skewed towards the center of the magnet location (0º).

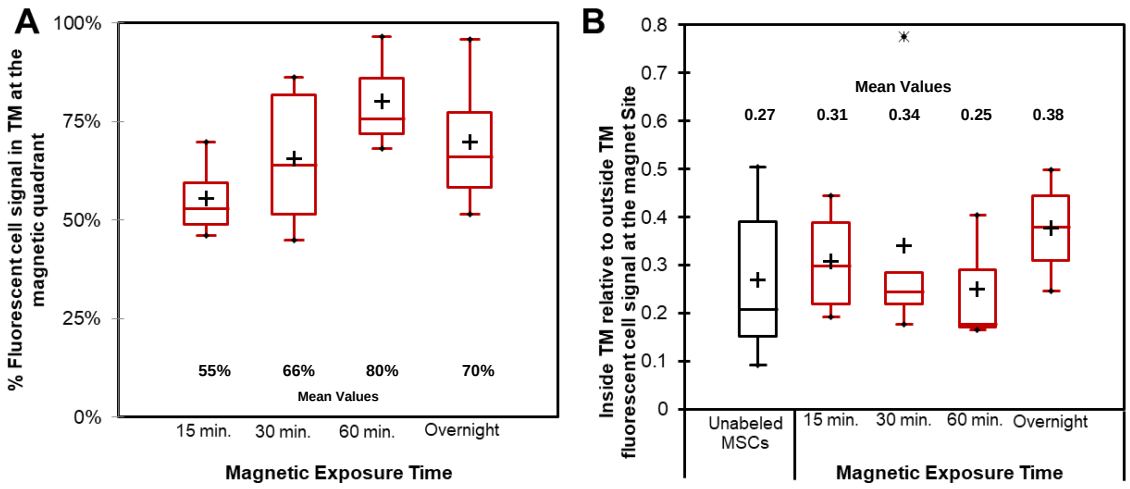


**Figure 26. Quantification of Fluorescence within the Quadrant Adjacent to the Magnet. (A)** Percentage of cell signal in the TM within the region 45$^{o}$ to -45$^{o}$ compared to cell signal around the entire TM. **(B)** Fluorescent signal in the TM region relative to the fluorescent signal not in the TM region at the magnet site. Box plot interpretation is as described in Figure 23. Mean values for each experimental group are shown in each plot.

### *5.3.4 Improving Delivery Efficiency to the Entire TM with PBNCs*

The above results show that PBNC-MSC delivery to a single quadrant of the eye can be improved by use of a magnet. We then considered whether delivery could be improved to the entire circumference of the eye. 250,000 MSCs were injected as before, and steered using one of two different ring magnet designs: Design I, a 3D printed magnet holder, and Design II, an axial polarized ring magnet (Figure 18). Design I was tested for a 30-minute magnet exposure, while Design II was assessed for 15- and 30-minute exposures (representative micrographs shown in Figure 27). Each configuration resulted in increased cell signal around the TM circumference compared to control injections (Figure 28 A - D). However, only Design II with exposures of 15 and 30 minutes resulted in a statistically uniform distribution, as determined by Rayleigh's test for uniform circular distribution. The greatest cell delivery was observed for Design II, 15-minute exposure, which resulted in as much as a 10x increase in cell delivery compared

to controls (Figure 29 A). Design II had lower ratios of cell signal inside the TM to signal outside the TM compared to Design I, indicating improved TM specificity. We conclude that PBNC-MSCs can be steered to the entire TM circumference in as little as 15 minutes, and optimization of the magnetic field placement can result in increased delivery specificity to the TM.

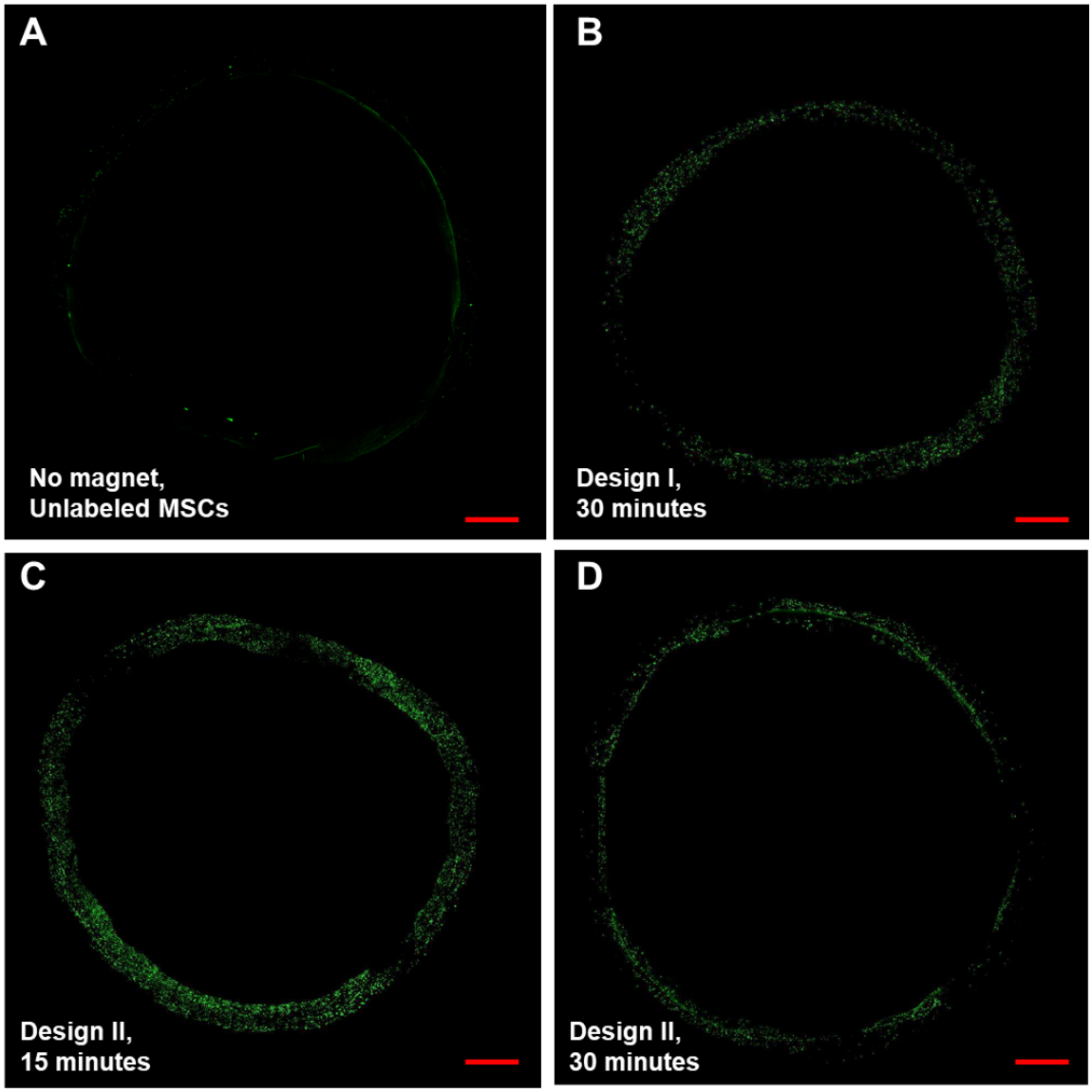


**Figure 27. 360º Delivery of PBNC-MSCs Using Ring Magnets.** 200nm labeled PBNC-MSCs were injected into eyes with several types of ring magnets placed around the circumference for different durations. Representative *en face* micrographs of the TM

region for **(A)** no magnet, **(B)** Design I for 30 minutes, **(C)** Design II for 15 minutes, and **(D)** Design II for 30 minutes. Scale bars denote 2mm.

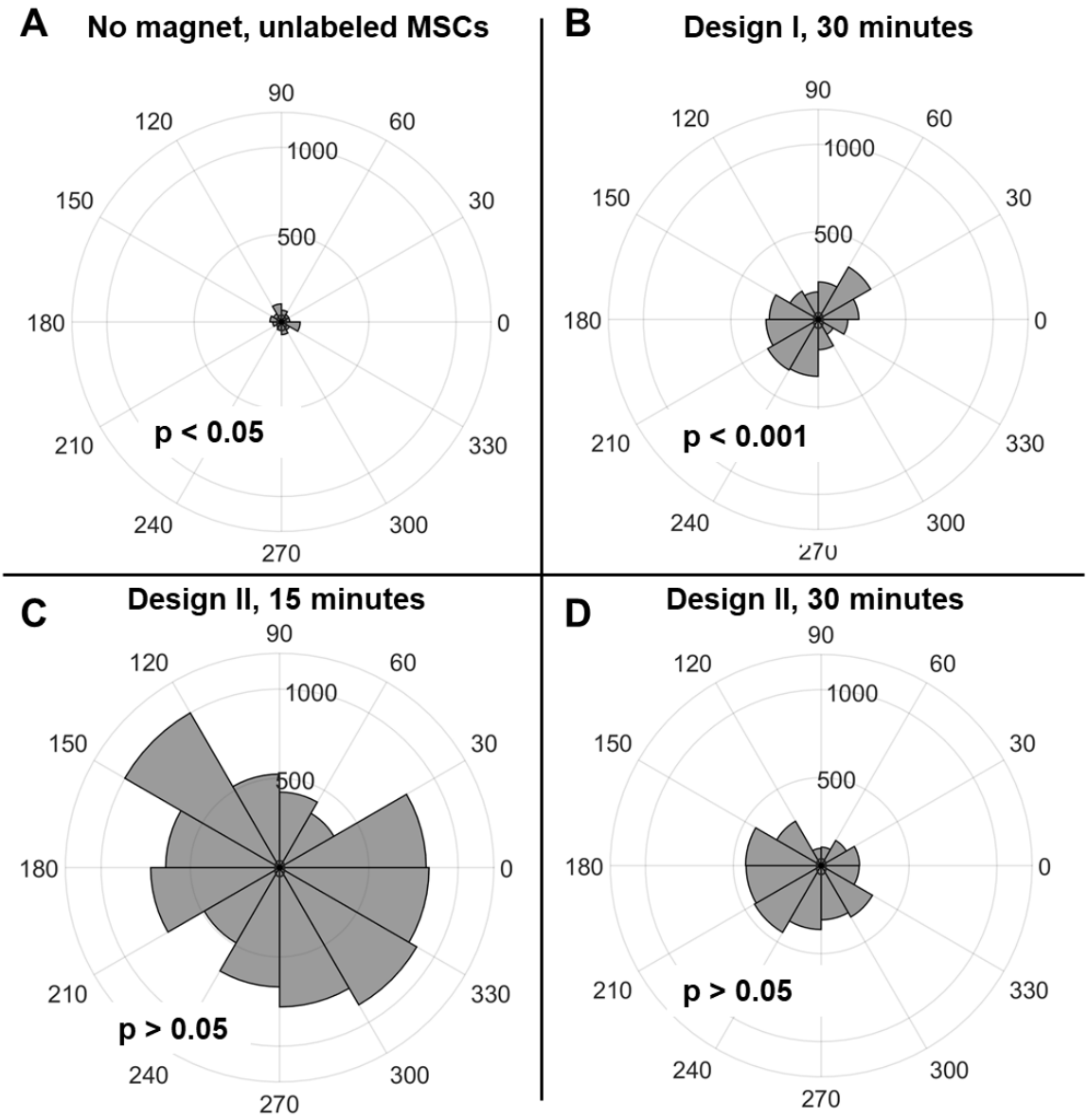


**Figure 28. Quantification of MSC Delivery in Ring Magnet Experiments.** Polar histograms illustrate MSC fluorescent intensity (radial coordinate, arbitrary units) for each 30$^{o}$ region. Average results for **(A)** control (n=5 eyes), **(B)** Magnet design I for 30 minutes (n=3 eyes), **(C)** Magnet design II for 15 minutes (n=3 eyes), and **(D)** Magnet design II for 30 minutes (n=3 eyes) experiments are shown. p-values were calculated using Rayleigh's test to assess uniform circumferential delivery ($p < 0.05$ denotes non-uniform delivery).

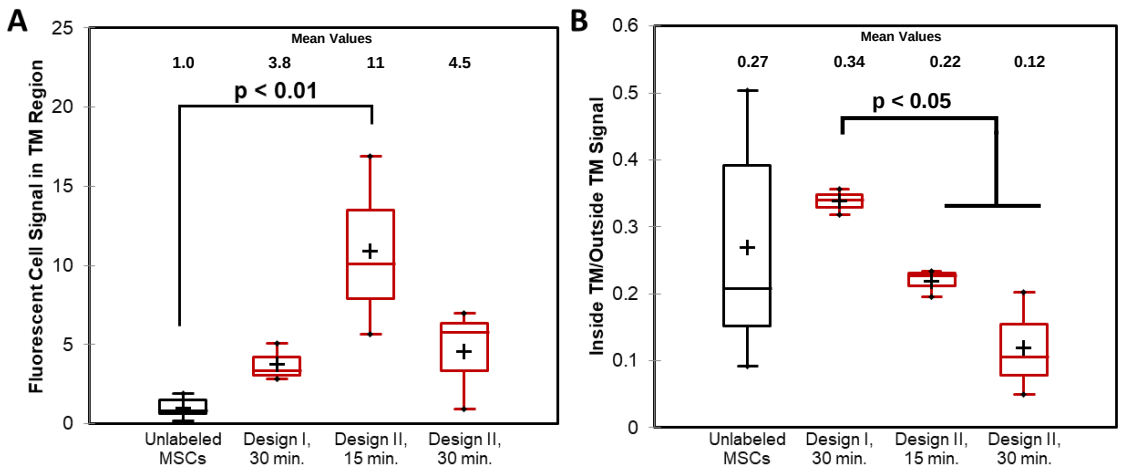


**Figure 29. Further Quantification of MSC Delivery in Ring Magnet Experiments. (A)** Total fluorescence signal in the TM around the entire circumference of the eye. **(B)** Fluorescent signal in the TM region relative to the fluorescent signal not in the TM region. Box plot interpretation is as described in Figure 23. Mean values for each experimental group are shown in each plot. Statistical significance was determined by ANOVA, with post-hoc Tukey.

### *5.3.5 Histological Assessment of the TM After PBNC-MSC Delivery*

*En face* micrographs lack the detail required to properly identify where cells are delivered within the TM. Thus, anterior segments were processed and resin-embedded, and 2 µm thick sagittal sections through the TM were cut. Representative images for overnight bar magnet and 15-minute Design II ring magnet exposures show 200nm PBNC-MSCs in the TM, as noted by the porous tissue structure and anatomical landmarks (Figure 30 A – D). Most of the cells remained on the inner TM structures as opposed to penetrating deeper into the tissue. We conclude that PBNC-MSCs are delivered to the TM.

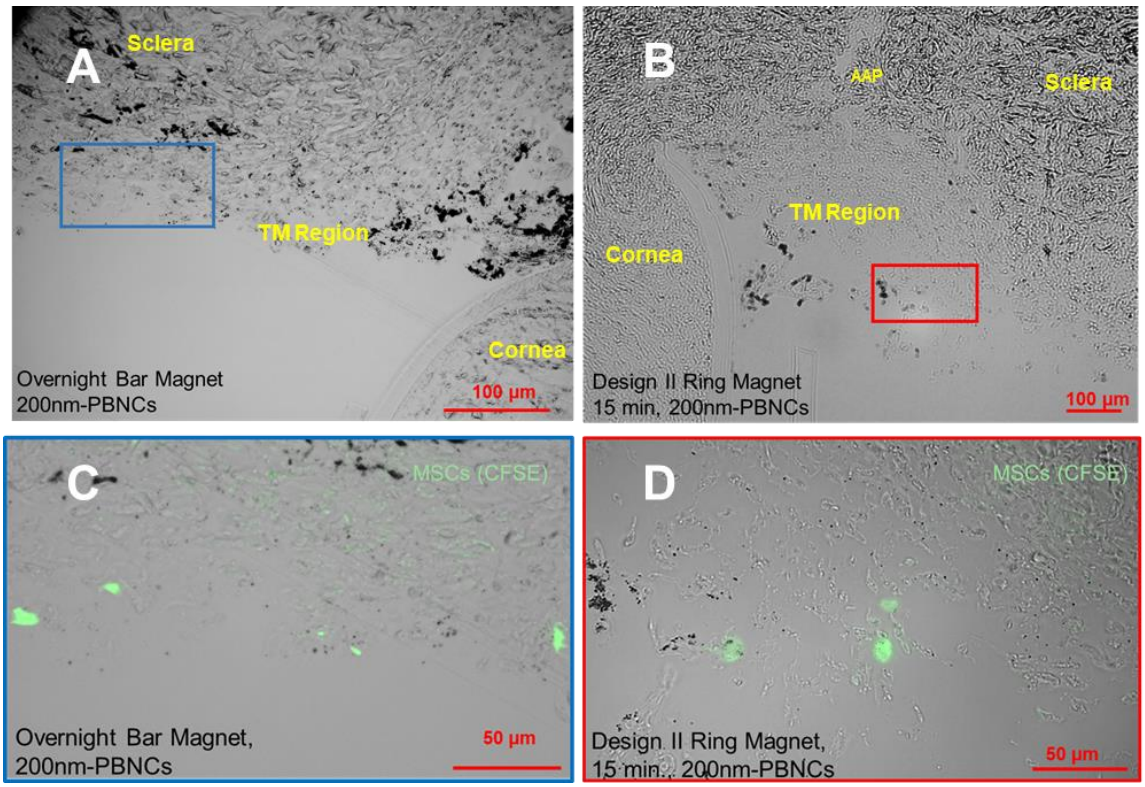


**Figure 30. Histological Assessment of PBNC-MSC Delivery to the TM.** Representative sagittal sections of the TM region showing fluorescently labeled PBNC-MSCs for **(A,C)** overnight bar magnet exposure and **(B,D)** Design II, 15 minute ring magnet experiments. **(A,B)** Lower magnification brightfield micrographs are labeled with relevant anatomical features for orientation (AAP = angular aqueous plexus, an analogue of Schlemm's canal in porcine eyes). Approximate zoomed regions are shown as blue and red boxes and magnified in panels **(C,D)**.

### *5.3.6 Toxicity of PBNCs on MSCs in vitro*

MSCs were incubated with different concentrations of 200nm PBNCs overnight. Cellular viability was then tested 1 day post-PBNC incubation to determine acute toxicity effects. To assess viability, cells were stained with propidium iodide and analyzed by flow cytometry. Minimal PBNC toxicity was observed after 1 day for both MSC donor strains (Figure 31A). To then assess cytotoxicity over longer terms, MSC nuclei were counted from micrographs 7 and 21 days after PBNC labeling in experiments testing MSC multipotentency. Cell counts were unaffected by PBNC labeling, suggesting these

particles were not toxic to MSCs (Figure 31 B,C), at least out to 21 days after PBNC exposure.

Finally, MSC viability after magnetic field exposure was assessed. Unlabeled and 200nm PBNC-labeled MSCs were maintained in 48 well plates and exposed to cylindrical magnets under each well for 0, 15, 30, 60 minutes or overnight. Labeled MSCs had similar viability to unlabeled controls at each time point (Figure 32), indicating that PBNCs did not interact with the applied magnetic field to reduce cell viability. However, and surprisingly, exposure of MSCs to a magnetic field for any duration resulted in significantly ($p < 0.05$) reduced viability compared to controls without magnetic exposure (Figure 32). While unexpected, magnetic exposure has been reported to reduce cell viability in certain types of mammalian and bacterial cells (Cellini et al., 2008; El May et al., 2009; Raylman et al., 1996; Strašák et al., 2005). Less toxicity was found with 15-minute magnetic exposure, further motivating the use of shorter magnet exposures.

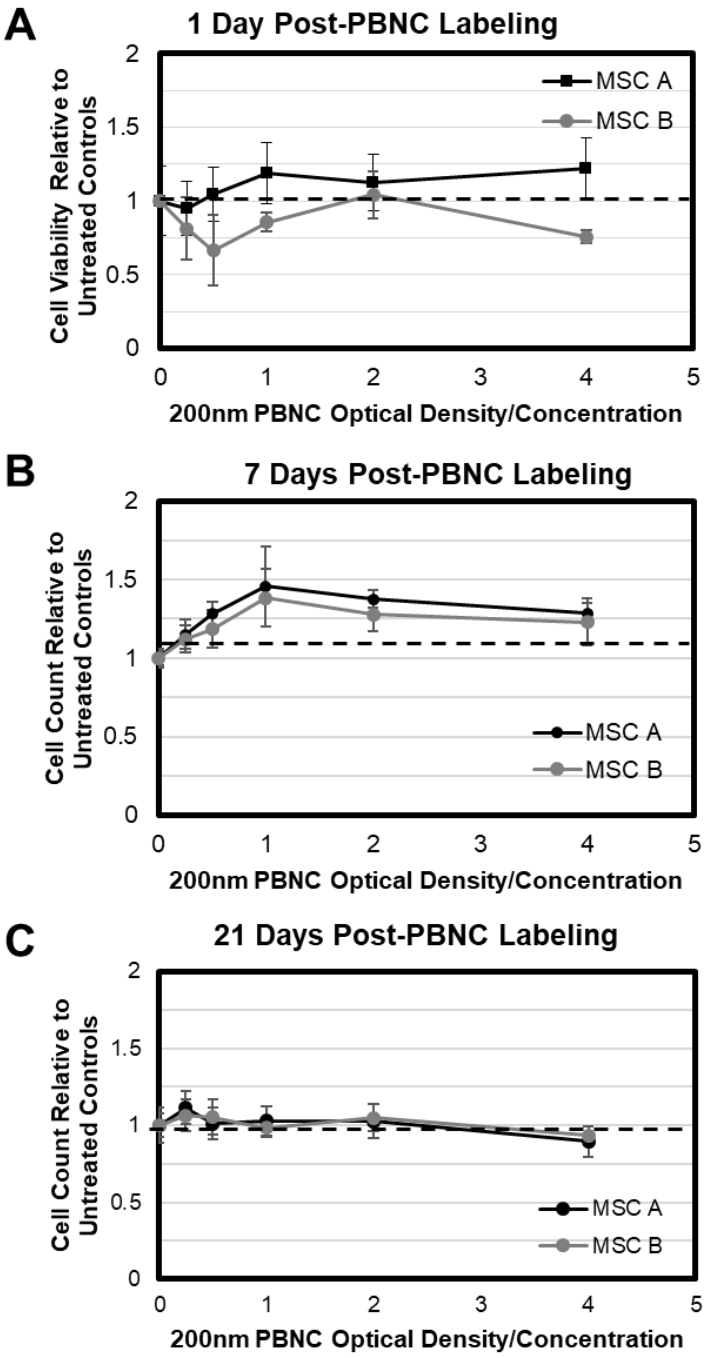


**Figure 31. Cell Viability Results for MSCs labelled with 200nm PBNCs.** Relative viability **(A)** 1 day after 200nm PBNC labeling for 2 MSC donor strains as determined by flow cytometry (n=3 technical replicates for each OD). **(B,C)** Cell counts relative to unlabeled controls for 2 MSC donor strains as determined by quantification of labelled nuclei using fluorescent microscopy following **(B)** 7 days adipogenic differentiation and **(C)** 21 days osteogenic differentiation (n=3 technical replicates for each OD). Error bars denote standard deviation. Asterisks denote significant difference ($p<0.05$) compared to unlabeled controls as determined by ANOVA, with post hoc Tukey.

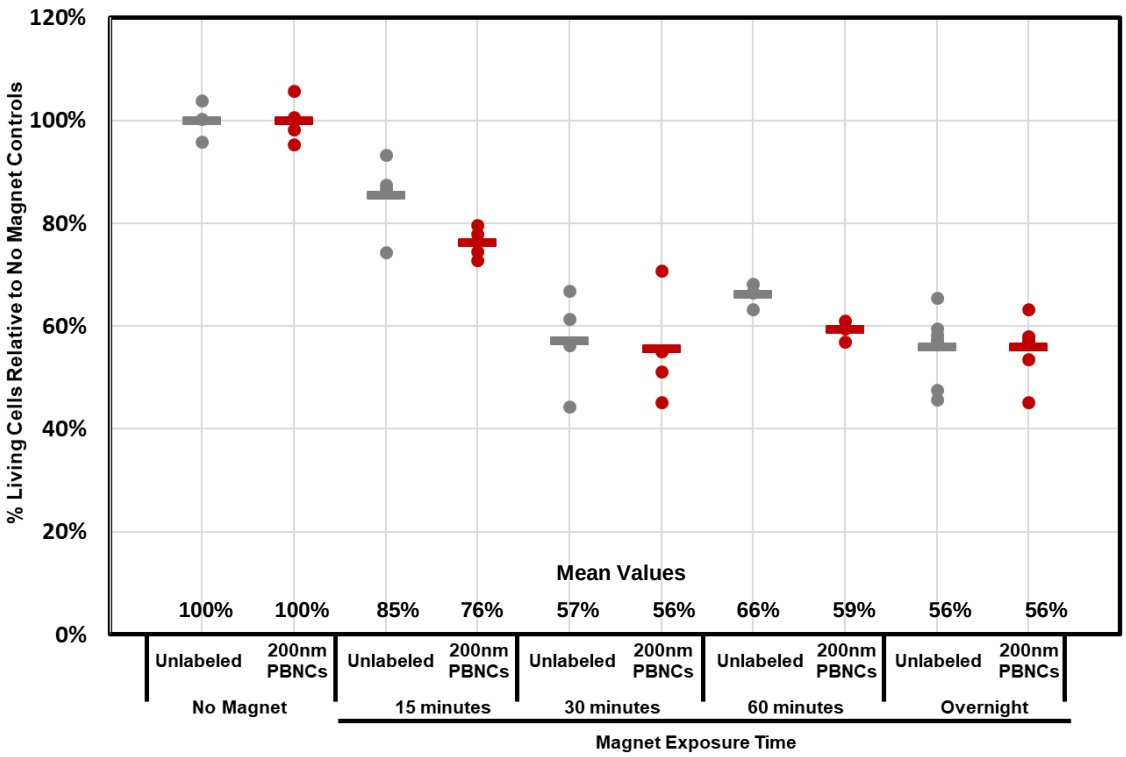


**Figure 32. Effect of Magnetic Field Exposure on MSC Viability.** Unlabeled and 200nm PBNC-labeled MSCs were incubated on top of cylindrical magnets for 0, 15, 30, 60 minutes or overnight. Magnetic field exposure reduced viability in an exposure-dependent manner. Individual data points for each group are shown with horizontal lines indicating means (n = 3 or 4 technical replicates for each condition). Cell viability within each group (unlabeled or labelled with PBNCs) was statistically different ($p < 0.05$) compared to their respective controls (no magnetic field exposure), as determined by ANOVA post-hoc Tukey. Mean values for each experimental group are shown in plot.

### *5.3.7 Effect of PBNCs on MSC Multipotency*

MSCs were treated with adipogenic medium for 7 days after PBNC labeling and qualitatively assessed for differentiation to adipocytes by Oil Red O staining (Figure 33 A-C). Positive lipid staining was found for all PBNC concentrations for 2 MSC donor cell lines. Further, cells were stained with Nile Red fluorescent stain and DAPI nuclei stain. Nile Red signal normalized to DAPI intensity resulted in similar ratios for each donor strain and PBNC concentration, indicating minimal effect of PBNCs on adipogenesis (Figure 33D).

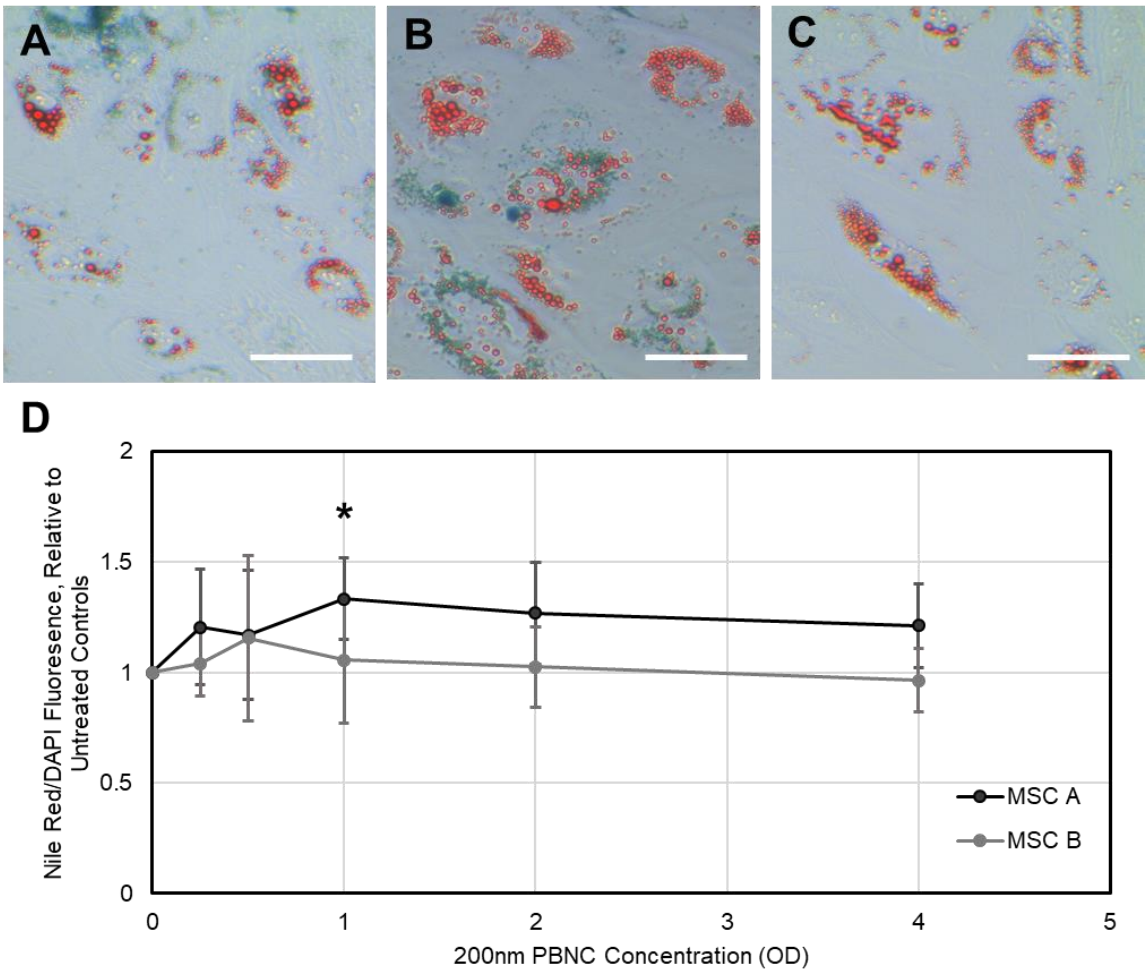


**Figure 33. Effect of 200nm PBNCs on MSC Adipogenesis. (A-C)** Oil Red O staining for lipids 7 days after adipogenesis treatment in **(A)** 4OD 200nm PBNC-MSCs, **(B)** 1 OD 200nm PBNC-MSCs, and **(C)** unlabeled MSCs. **(D)** Quantification of ratio of fluorescent Nile Red (lipids) to DAPI (nuclei) signal relative to untreated controls for 2 stem cell lines (n=3 technical replicates for each concentration). Error bars denote standard deviation. Asterisks denote significant difference ($p < 0.05$) compared to unlabeled controls as determined by ANOVA, with post hoc Tukey.

MSCs were also differentiated towards an osteogenic phenotype for 21 days, followed by staining with Alizarin Red to detect free calcium (Figure 34 A-C). Alizarin Red staining was detected consistently in all experimental conditions. Alizarin Red fluorescent intensity normalized to DAPI fluorescent intensity was similar for all PBNC concentrations and for both MSC donor strains, indicating minimal effect of PBNCs on osteogenesis (Figure 34D).

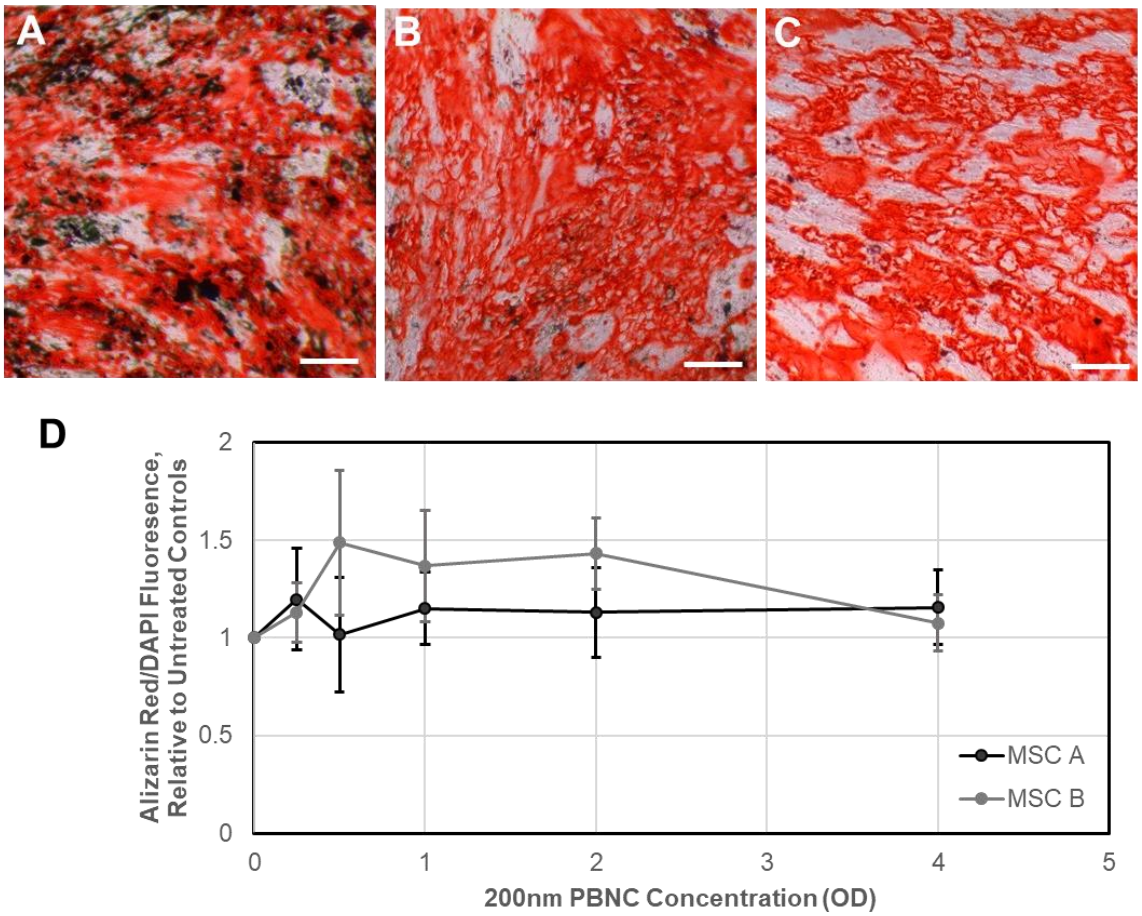


**Figure 34. Effect of 200nm PBNCs on MSC Osteogenic Potential. (A-C)** Alizarin Red O staining for free calcium after 21 day osteogenesis treatment in **(A)** 4OD 200nm PBNC-MSCs, **(B)** 1 OD 200nm PBNC-MSCs, and **(C)** unlabeled MSCs. **(D)** Ratios of fluorescent Alizarin Red (free calcium) to DAPI (nuclei) signal relative to untreated controls for 2 stem cells (n=3 technical replicates for each concentration). Error bars denote standard deviation.

## 5.4 Discussion

Stem cells have the potential to repair the damaged TM in glaucoma and thus restore IOP homeostasis. To achieve this goal, it is highly desirable to optimize cell delivery to the TM. Previous studies in which cells were injected into the anterior chamber and then passively carried to the TM by aqueous humor flow showed that stem cells were undetectable in the TM after only 4 days, or showed significant stem cell delivery to unwanted sites, such as the cornea and iris (Manuguerra-Gagne et al., 2013;

Roubeix et al., 2015). In addition, segmental flow to the TM makes delivery to the entire TM circumference impossible if cells are driven by passive aqueous humor outflow, a problem that is exacerbated in glaucoma patients. We thus investigated active stem cell delivery to the TM. Specifically, we assessed whether magnetic nanoparticles could be utilized to steer MSCs to the TM in the presence of a magnetic field.

We tested two PBNC sizes for cell steering, since particle size was hypothesized to impact cell steering. We observed that both PBNC sizes were capable of labeling MSCs, but that 200nm PBNCs were more effective at steering MSCs to the TM than 20nm PBNCs. This is consistent with the fact that 200nm PBNCs have a larger SPION core than 20nm PBNCs and should thus be more responsive to a magnetic field.

We wondered whether the increased steering effectiveness of 200 nm PBNCs was simply a matter of the total amount of iron loaded into the cell. We tested this by comparing MSC steering in cells incubated with very high concentrations of 20 nm PBNCs vs. cells incubated with a lower concentration of 200 nm PBNCs. Our data show that 20nm PBNCs at 10 OD concentration had only a modest benefit on cell delivery, while 200nm PBNCs at 2OD concentration markedly improved cell steering efficiency, even though there was more iron present per cell volume in the former case than in the latter. We conclude that iron content per cell was not the sole factor influencing MSC steering efficiency, and that the larger iron oxide core in 200nm PBNCs must play a role beyond just iron content.

Regenerative medicine therapies rely on MSCs to restore tissue function through paracrine signaling or cellular differentiation, so it is important that PBNCs not adversely affect MSC function if they are to be used in practice. Fortunately, 200nm PBNCs did not reduce MSC viability out to 21 days, nor did they adversely affect multipotency. One goal

of MSC therapies for the TM is for MSCs to differentiate into TM cells after delivery. While differentiation of labelled MSCs to a TM-like phenotype has not been established, evidence that PBNCs do not alter traditional differentiation pathways suggests that MSC to TM cell differentiation will also not be affected.

Although PBNCs were not toxic to MSCs, we were surprised to find that exposure to a magnetic field did alter MSC viability, with or without PBNC labeling. The time-dependence of this effect suggests that short magnetic exposure times will be necessary for future translational developments. It is possible that the magnets used in this study were too strong for translational use, and weaker magnet strengths or even shorter durations may be needed as this labeling technology is further developed.

For *in vivo* usage and eventual clinical translation, it is advantageous to have a magnet exposure time that is as short as possible. We observed that 200nm PBNC-MSCs could be steered to the TM in as little as 15 minutes, with additional exposure time resulting in little net benefit. Further, since the shortest exposure tested was still effective, it is possible that even shorter durations may be effective. This point is particularly important in view of the observation that exposure of MSCs to a magnetic field results in a time-dependent loss of viability, implying that the shortest possible magnetic exposure is preferred.

Another aspect to consider when optimizing magnet exposure time was non-specific delivery to other anterior segment surfaces. Interestingly, overnight magnet exposure resulted in approximately 25% less non-specific delivery, compared to 15-, 30- and 60-minutes exposure times, indicating better TM-targeted delivery with long duration exposures. It is unclear why overnight exposure times would reduce non-specific delivery. One possibility is increased MSC death due to prolonged magnet exposure

which could reduce signal in the TM and non-specific anterior tissues. Further, MSCs could have been pulled “deeper” in the tissue so that they were not visible by fluorescent confocal microscopy due to light penetration limitations into tissue. Overall, however, differences in non-specific delivery were not significant between any magnet exposure time, suggesting shortest possible magnetic exposure is still preferred.

Excitingly, MSCs labelled with 200nm PBNCs could be magnetically steered to the entire TM circumference. We observed some degree of uniform cell delivery for both ring magnet configurations tested, with Design II at 15 and 30 minute exposures resulting in more cell signal in the TM compared to Design I at 30 minutes. However, Design I had higher specificity for the TM region compared to Design II. The differences between these two ring-magnet designs can help inform magnetic field design for future work. Design II was a commercially-available, axially-polarized ring magnet, meaning most of the pulling force was in the axial direction, which would not be effective at steering MSCs to the TM, which primarily required forces on injected cells in the radial direction. Indeed, a radially-directed magnetic force was present only near the top and bottom faces of the magnet, and, while one of the faces was near the limbus, the other was not since the magnet height was much greater than the TM height. As a result, this likely led to undesired cell delivery near the second magnet face.

However, one advantage of the Design II ring magnet was that the magnet was in direct contact with the limbus, presumably creating high field strengths near the TM. This was unlike Design I, in which 10 smaller magnets were positioned in a 3D-printed holder. Although the overall magnetic pulling force was directed towards the TM, the plastic holder resulted in a gap between the magnet and eye surface, reducing the magnetic field strength at the TM and, presumably, reducing cell delivery efficiency. Conversely, with the overall magnetic pull force focused at the TM region, higher

delivery specificity was obtained. This discussion highlights the benefits of optimizing the magnetic field, which presumably will be useful in delivering labelled cells efficiently to the entire TM with minimal delivery to unwanted tissue targets.

## 5.5 Conclusions

This study demonstrates the potential for steering MSCs magnetically to the TM. PBNCs were found to be suitable for MSC labeling, resulting in minimal toxicity effects in MSCs and no detectable impact on their ability to differentiate toward adipogenic or osteogenic lineages. To magnetically steer labelled MSCs to the TM, 200nm PBNCs were found to be more effective than 20 nm PBNCs. Further, magnetic steering was rapid, with magnetic exposure times of as little as 15 minutes showing large effects on MSC delivery. One key issue in passive, conventional MSC delivery to the TM is segmental delivery to active flow regions of the TM. Magnetic steering of MSCs using a ring magnet resulted in relatively uniform delivery around the entire TM circumference. This labeling technology for delivering cells to the entire TM at higher efficiencies compared to passive delivery has the potential to improve MSC therapies for the TM as regenerative medicine therapies for glaucoma are developed.

For small animal models and eventual clinical translation, the magnetic field placement and PBNC labelling should be further optimized. Specifically, by adjusting the magnetic field and, potentially, altering the PBNC concentration for MSC labeling, more precise delivery of MSCs to the TM region with minimal unwanted delivery to other ocular tissues should be possible. It will be important to minimize the magnetic field-associated toxicity that we observed, which implies a need for using shorter magnet field exposures. Next steps will use ultrasound-photoacoustic imaging of the PBNC-labeled MSCs to track delivery and engraftment of MSCs into the TM region, simplifying

optimization of this technology in animal models of glaucoma for eventual therapeutic experiments.

## 5.6 Acknowledgements

This work was supported by the Georgia Research Alliance (CRE, SE).

# CHAPTER 6. Development of a Porcine Organ-Culture Glaucoma Model Mimicking Trabecular Meshwork Damage

This chapter is a manuscript to be submitted to Investigative Ophthalmology & Visual Science with the following author list: Eric J. Snider, Rebecca Hardie, Yinglin Li, Richard K. Kim, Fiona Splaine, C. Ross Ethier

---

## 6.1 Abstract

Glaucoma, the second leading causes of blindness, impacts over 70 million people worldwide. A well-established risk factor is elevated intraocular pressure (IOP); IOP is primarily determined by the inner wall of Schlemm's canal and the trabecular meshwork (TM), a tissue located in the anterior segment which drains aqueous humor from the eye. In glaucoma, TM cellularity is reduced. This loss of cellularity presumably leads to loss of TM function and hence elevated IOP. Stem cells, if suitably differentiated, could offer a potential therapy for glaucoma. To test such regenerative medicine therapies, glaucomatous damage in the TM needs to be modeled properly *in vivo* or *ex vivo*. Using a porcine anterior segment organ culture preparation, we here show that oxidative stress, induced by hydrogen peroxide, can reduce TM cellularity to glaucomatous levels, which in turn resulted in loss of IOP homeostasis. Damage from hydrogen peroxide was not destructive to the TM, an essential characteristic of a glaucoma model for use in TM regenerative medicine testing. Stem cell delivery to the TM in this model resulted in proper cell engraftment which was not consistently observed in untreated controls. In conclusion, this porcine organ culture model offers an improved

platform for assessing regenerative medicine therapies for the trabecular meshwork in glaucoma.

## 6.2 Introduction

Primary open angle glaucoma (POAG), responsible for an estimated 74% of glaucoma cases worldwide, is a leading cause of irreversible blindness (Quigley and Broman, 2006). The best-established risk factor for POAG is elevated intraocular pressure (IOP), which is determined by the aqueous humor production rate and the outflow of aqueous humor (Weinreb and Khaw, 2004). The primary aqueous humor drainage route, known as the conventional pathway, consists of the trabecular meshwork (TM), Schlemm's canal, and the distal vessels (Fautsch and Johnson, 2006; Goel et al., 2010).

The cellularity of the TM is reduced in POAG patients (Alvarado et al., 1984; Baleriola et al., 2008; Gonzalez et al., 2006; Liton et al., 2005). The TM, along with the inner wall of Schlemm's canal, is the major site of aqueous outflow resistance. TM cells phagocytose debris from aqueous humor to prevent outflow blockage, are contractile to alter outflow resistance, and are active remodelers of their extracellular matrix to alter TM extracellular matrix characteristics (Bradley et al., 2003; Buller et al., 1990; De Groef et al., 2013; Llobet et al., 2003; Sherwood and Richardson, 1988). Thus, reduced TM cellularity presumably leads to tissue dysfunction and subsequent increased outflow resistance and elevated IOP. Therapies that focus on restoring TM cellularity and function using stem cells could offer therapeutic benefit to POAG patients.

To test such therapies, a model that mimics TM dysfunction, including ocular hypertension (OHT) and reduced cellularity, is needed. However, most current glaucoma models are focused on studying optic neuropathy secondary to OHT, and thus alter the

outflow pathway in ways that do not replicate the situation in human glaucoma (Gaasterland and Kupfer, 1974; Ishikawa et al., 2015; Morrison et al., 1997; Shareef et al., 1995; Weber and Zelenak, 2001). There are several exceptions, in which reduced TM cellularity has been achieved without severe TM damage. In one study, Zhang *et al*. ablated TM cells in rat eyes using a cytotoxic vector (Zhang et al., 2014); interestingly, they observed a reduced IOP after this procedure. Senatorov et al. expressed mutant myocilin in mice, which led to reduced TM cellularity and elevated IOP (Senatorov et al., 2006; Zode et al., 2011). Unfortunately, mutations in myocilin are only associated with 3 to 4% of POAG cases, and may not translate to other POAG varieties (Tamm, 2002). Abu-Hassan *et al.* used saponin, a plant-derived detergent, to reduce TM cellularity in organ-cultured human and porcine anterior segments (Abu-Hassan et al., 2014b). They reported that IOP homeostasis was altered in human anterior segments after saponin treatment. Unfortunately, the saponin model does not appear to work in porcine eyes, either in our hands or in the lab of the original publication (M. Kelley, personal communication).

Anterior segment organ culture is a well-established method for studying TM function, in which TM cell viability and function can be maintained for several weeks. Ideally, all organ culture experiments would use human tissue. However, poor availability and high cost makes this option infeasible for many labs. Thus, anterior segment organ culture experiments have used monkey, porcine, bovine, or human eyes (Bachmann et al., 2006; Bhattacharya et al., 2009; Erickson-Lamy et al., 1991; Johnson and Tschumper, 1987, 1989; Mao et al., 2011).

Our goal was to create a model of graduated TM cell loss and dysfunction using readily available porcine anterior segments in organ culture. For this purpose, we chose to utilize oxidative stress-induced damage to the TM. Here, we show that hydrogen

peroxide ($H_2O_2$) can be used to reduce TM cellularity, leading to tissue dysfunction in the form of reduced IOP homeostasis. This organ-culture TM dysfunction model offers an attractive platform for assessing stem cell therapies and their potential for refunctionalizing the TM.

## 6.3 Methods and Materials

To determine the effects of $H_2O_2$ exposure on cell viability, we first used isolated, cultured porcine TM (pTM) cells. Cells were treated with different $H_2O_2$ concentrations and viability was assessed until cellularity was reduced by ~50%. pTM cells were further assessed for phenotypic function after $H_2O_2$ treatment. We next implemented $H_2O_2$ treatment in porcine anterior segments maintained in organ culture. Finally, functional, viability and histological assessments were used to determine the effect of $H_2O_2$ treatment on the TM.

### *6.3.1 Cell Sourcing*

#### 6.3.1.1 Porcine TM Cell Isolation and Characterization

Porcine TM cells were isolated from fresh porcine eyes obtained from a slaughterhouse (Holifield Farms, Covington, GA) within 6-8 hours of enucleation. Eyes were dissected to isolate the anterior chamber similar to previously reported methods (Bachmann et al., 2006; Bhattacharya et al., 2009). Briefly, orbital connective tissue was dissected away and eyes were soaked in Betadine solution (Purdue Pharma) for 5 minutes. Following Betadine immersion, eyes were washed 3 times with sterile PBS containing 5x penicillin, 5x streptomycin, and 1x amphotericin and transferred to a sterile laminar flow hood for the remainder of the process. Eyes were hemisected with a razor blade to isolate the front half of the eye. The vitreous humor and lens were removed, the

iris was cut radially back to the iris root and pectinate ligaments until the TM was revealed, and the ciliary processes were carefully removed with Vannas microscissors (World Precision Instruments) while preserving the TM. Any remaining vascularized or pigmented tissue was removed.

Next, the TM was removed from the corneoscleral shell with curved, fine forceps (Fine Science Tools) and placed in 10 mg/mL Collagenase IV digestion solution for 30 minutes at 37$^{o}$C as previously described (Stamer et al., 1995). Collagenase IV was neutralized by addition of 10% FBS media and the tissue digest was centrifuged at 1000 rpm for 10 minutes. The pellet was resuspended in 3 mL 10% FBS-containing Dulbecco's modified Eagle's media (DMEM) supplemented with penicillin, streptomycin, and 2mM L-glutamine (TM Cell media) and placed on a 0.1% (w/v) gelatin-coated 6 well plate for 48 hours to allow cells to attach. At ~90% confluency, pTM cells were detached with 0.05% trypsin-EDTA (w/v) and plated in new culture flasks at 5,000 cell/cm$^2$ (~3:1 split ratio). Cells were expanded and used between passage 4 and 6 for all experiments.

To confirm cells had TM-like properties, cells were plated at 10,000 cells/cm$^2$ in 6 well plates and were assessed for myocilin expression following dexamethasone (DEX) treatment. 100nM DEX was added in TM cell media for 7 days to cultured cells, replacing the media every 3 days. After 1 week of treatment, RNA was isolated from cells using TRIzol reagent (Life Technologies) and further purified using Aurum Total RNA Mini Kit per the manufacturer's protocol (Bio-Rad). RNA concentration and purity were determined using a Nanodrop 2000C spectrophotometer (Thermo-Scientific). Reverse transcription to clonal DNA (cDNA) was performed on 1µg RNA samples following the manufacturer's protocol (Bio-Rad). cDNA samples were analyzed for porcine myocilin and reference genes (Table 3). SYBR green reagent (Quantabio) was used to quantify DNA amplification in real time throughout the PCR cycle (StepOnePlus

Real Time PCR System, Applied Biosystems). The resulting cyclic threshold ($C_T$) values were normalized to the geometric mean of three housekeeping messengers (GUSB, TATA Binding Protein, GAPDH) and further normalized against untreated pTM samples using the $2^{-\Delta\Delta CT}$ methodology (Livak and Schmittgen, 2001). We observed significant increases in myocilin message levels after DEX treatment in all pTM cell lines tested, confirming the TM phenotype (Figure 35).

**Table 3. Primer Sequences Used in RT-qPCR Experiments**. Primers were selected using Primer-Blast (NCBI) software following established protocols (Ye et al., 2012).

| Porcine Primer Name | | Primer Sequence (5' to 3') |
|---|---|---|
| Myocilin (MYOC) | Forward | CAGGCTCACAGCATGTCTCA |
| | Reverse | CCACATCCACTGCCTCCTTC |
| Glyceraldehyde-3-Phosphate Dehydrogenase (GADPH) | Forward | ACCAGGTTGTGTCCTGTGAC |
| | Reverse | AGCTTGACGAAGTGGTCGTT |
| TATA Binding Protein (BP) | Forward | AATCCCAAGCGATTTGCTGC |
| | Reverse | CGTGCACACCATTTTCCCAG |
| Beta-Glucuronidase (GUSB) | Forward | GACGGACACCTCCAAGTACC |
| | Reverse | CATCGATGTAGGCGGTAGGC |

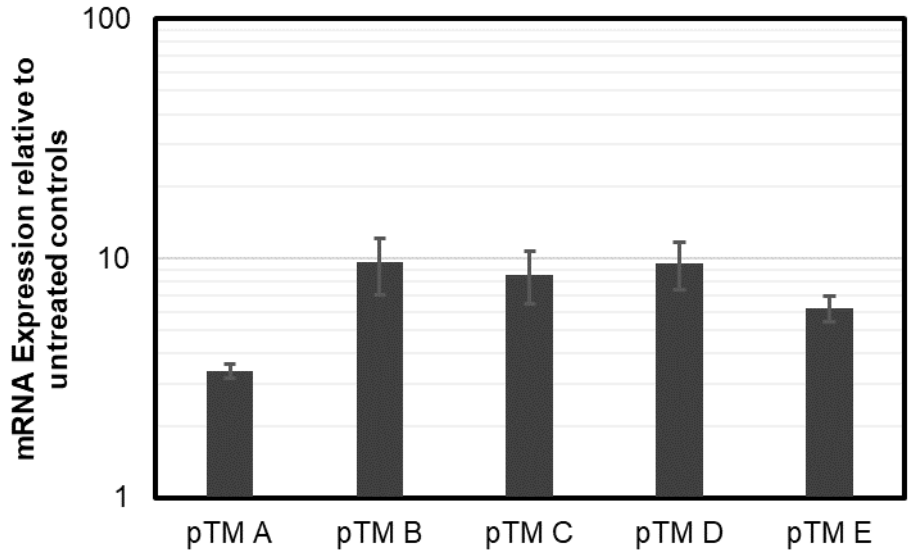


**Figure 35. pTM Cell Characterization.** pTM cells were treated with 200nM DEX for 7 days, and MYOC mRNA levels were assessed by RT-qPCR. MYOC expression is shown relative to untreated controls for each pTM cell isolation. Note that vertical axis is

logarithmic. Error bars denote standard deviation (n = 4 technical replicates). Each bar represents one porcine TM cell line. Significant differences ($p<0.05$) between DEX-treated and control samples was found for all samples as determined by ANOVA, with post-hoc Tukey.

#### 6.3.1.2 Mesenchymal Stem Cell Sourcing and Characterization

Human adipose-derived mesenchymal stem cells (MSCs, Lonza) were grown in α-minimum essential medium supplemented with 20% FBS, penicillin, streptomycin, and L-glutamine (MSC Media). At 80-90% confluency, MSCs were detached using 0.05% Trypsin-EDTA (w/v, Cellgro, Corning) and seeded in fresh cell-culture T75 flasks at a density of 5,000 cells/cm$^2$. In all experiments, MSCs were used at passage numbers five or six. Each MSC donor strain was validated by Lonza for expression of MSC surface markers (CD13, CD29, CD44, CD73, CD90, CD105, and CD166) and minimal expression of negative MSC markers (CD14, CD 131, CD45). We also previously characterized each MSC donor strain for adipogenic, chondrogenic, and osteogenic differentiation and CD90 expression following expansion (Snider et al., 2017).

### *6.3.2 Exposure of Cells to Hydrogen Peroxide in vitro*

Porcine TM cells were plated at 10,000 cells/cm$^2$ in TM cell media and allowed to deposit extracellular matrix and proliferate for at least 48 hours. For viability assessment (see section 6.3.3.1), pTM cells were plated in 24 well plates while 6 well plates were used for functional experiments (see sections 6.3.3.2 – 6.3.3.4). Cell media was aspirated, and cells were washed once with phosphate-buffered saline (PBS). Commercially-available hydrogen peroxide obtained fresh from a local pharmacy ($H_2O_2$, 3% w/v) was 0.22µm sterile filtered and prepared at specified concentrations in serum-free DMEM supplemented with 2mM L-glutamine and 1x penicillin, streptomycin, and amphotericin (Organ culture media). After $H_2O_2$ addition, cells were incubated at 37$^o$C for

1 hour. $H_2O_2$-containing media was then removed, and cells were washed once with PBS. pTM cells were assessed immediately when indicated, or organ culture media was added for further cell culture.

### *6.3.3 pTM Cell Characterization After $H_2O_2$Treatment*

#### 6.3.3.1 Cellular Viability Assessment *in vitro*

To determine cell viability *in vitro*, media was replaced with propidium iodide in PBS, followed by incubation at 37°C for 5 minutes to stain dead, adherent cells. Propidium Iodide was removed and 0.05% Trypsin-EDTA (w/v) was added for 5 minutes to detach cells. TM cell media was then added to neutralize trypsin activity, and cell suspensions were collected in deep-well 96-well plates (Corning). Cell samples were processed by flow cytometry (Attune NxT). Living cell counts were compared to control, untreated cell counts to determine viability after $H_2O_2$ treatment. Viability was assessed immediately, 24 hours, and 48 hours following $H_2O_2$ treatment as indicated.

#### 6.3.3.2 Metabolic Activity Assessment

To determine the effect of $H_2O_2$ on metabolic activity, pTM cells were seeded 24 hours after $H_2O_2$ treatment at 10,000 cells/cm$^2$ in 96 well plates in Hanks' balanced salt solution (HBSS) supplemented with 5% FBS and 2mM L-glutamine. The following day, Alamar blue (resazurin) in fresh media 10% (v/v) was added to each cell sample (O'Brien et al., 2000). The increase in Alamar blue fluorescence was detected by using a plate reader (Cytation 3, Bio-Tek) incubated at 37°C in a 5% $CO_2$ atmosphere, with readings (Excitation 545nm, Emission 590nm wavelengths) taken every 10 minutes for at least 2 hours. Fluorescence was plotted vs. time for each cell sample and the slope of

the linear region was found. Slopes were compared between treated and untreated cell samples to determine the effects of $H_2O_2$ on metabolic activity.

#### 6.3.3.3 Phagocytic Activity Assessment

TM cells have been shown to be actively phagocytic *in vivo*, removing particulate/cellular debris from the aqueous humor to avoid clogging the meshwork (Buller et al., 1990; Sherwood and Richardson, 1988). To quantify phagocytosis, pHrodo *e.coli* BioParticles (Life Technologies) were used following previously developed methods (Gagen et al., 2013; Snider et al., 2017). 24 hours after $H_2O_2$ treatment, cells were seeded at 50,000 cells/cm$^2$ onto 96 well plates in Hanks' balanced salt solution (HBSS) supplemented with 5% FBS and 2mM L-glutamine. Cells were allowed to attach overnight before assessing phagocytosis. pHrodo particles (2 million cells/vial) were reconstituted in HBSS media, sonicated for 5 minutes, and added to experimental samples. Control samples remained in HBSS media.

After a 4-hour incubation at 37$^o$C, HBSS media was removed and cells were detached with 0.05% Trypsin-EDTA. Detached cells were transferred to 96 well plates and data was collected with a flow cytometer (Attune NxT, Thermo-Fisher Scientific) at 100µL/min. Unstained median fluorescent intensity (MFI) values were subtracted from MFI values measured in phagocytically-challenged samples. Ratios of MFI values in $H_2O_2$ treated cells to MFI values in control, untreated cells were calculated to determine $H_2O_2$ effect on phagocytic activity.

#### 6.3.3.4 Gel Contractility Assessment

Cell contractility was determined using a collagen gel contraction assay, since trabecular meshwork cells are contractile (Dismuke et al., 2014b). 24 hours after $H_2O_2$

treatment, cells were resuspended in serum-free DMEM at 9 x $10^5$ cells/mL. Collagen type I (3mg/mL, 1% [v/v] acetic acid, calf skin, MP Biomedical) was added to cells at a 1:2 volume ratio (collagen:cells) followed immediately by a pretitrated volume of 0.1M sodium hydroxide to neutralize the acidity. Collagen gels (1mg/ml, 6x$10^5$ cells/mL) were then cast in 48 well plates at 240µL gel solution per well. After 20 minutes to allow gelation, an equal 240µL volume of serum-free media was added to provide nutrients needed for cell attachment while minimizing proliferation. After 24 hours, gels were released from the walls of the 48-well plate using a pipette tip. Gels were incubated for a further 24 hours to allow time for gel size to reach steady state. Images of each gel were taken immediately following release from the walls and at 24 hours (ChemiDoc MP, Bio-Rad). Using ImageJ, gel area was quantified for each image to determine the magnitude of gel contraction by comparing initial gel size to steady-state size. Percent gel contraction was compared between $H_2O_2$-treated and control (untreated) cell samples to determine $H_2O_2$ effects on gel contractility.

### *6.3.4 Porcine Anterior Segment Organ Culture*

Dissected anterior segment, prepared as described earlier, were placed in custom-built organ culture dishes and clamped in place (Figure 36). Organ culture dishes were placed in a sterile 37$^o$C humidified incubator and perfused at 2.5 µL/min with organ culture media, while pressure was measured every 60 seconds (142pc01g, Honeywell) and recorded in LabView. Eyes were stabilized for at least 48 hours before adding $H_2O_2$ or other agents. Any eyes which did not demonstrate a stable outflow facility (a ratio between perfusion flow rate and IOP) between 0.125 and 0.45 µL/min/mmHg (pressures of ~6mmHg to 20mmHg IOP) were considered as outliers and discarded (Figure 36).

### *6.3.5 Hydrogen Peroxide Treatment in Organ Culture*

After IOP stabilization, 4.5mM $H_2O_2$ in organ culture media was perfused into eyes for 1 hour. To rapidly expose the anterior segments to $H_2O_2$, the perfusion flow rate was increased to 2.5mL/min until approximately 7-10mL of 4.5 mM $H_2O_2$ had been infused. During this exchange period, anterior segments were open to hydrostatic reservoirs to maintain constant pressure (6-12 mmHg) and for media outflow while the perfusion flow rate was increased. After the exchange had been completed, anterior segments were returned to the normal perfusion flow rates of 2.5 µL/min for 1 hour and the valve connecting the culture dish to the hydrostatic reservoirs was closed, during which time the perfusate consisted of media with added 4.5mM $H_2O_2$. At the conclusion of this one hour period, anterior segments were again exchanged with an additional 7-10mL of organ culture media at 2.5mL/min to flush $H_2O_2$–containing media from the anterior segment. Finally, anterior segments were perfused for an additional 24 hours at 2.5µL/min to allow IOP stabilization following treatment with $H_2O_2$. For control anterior segments, the same protocol was followed except that no $H_2O_2$ was added to the organ culture media.

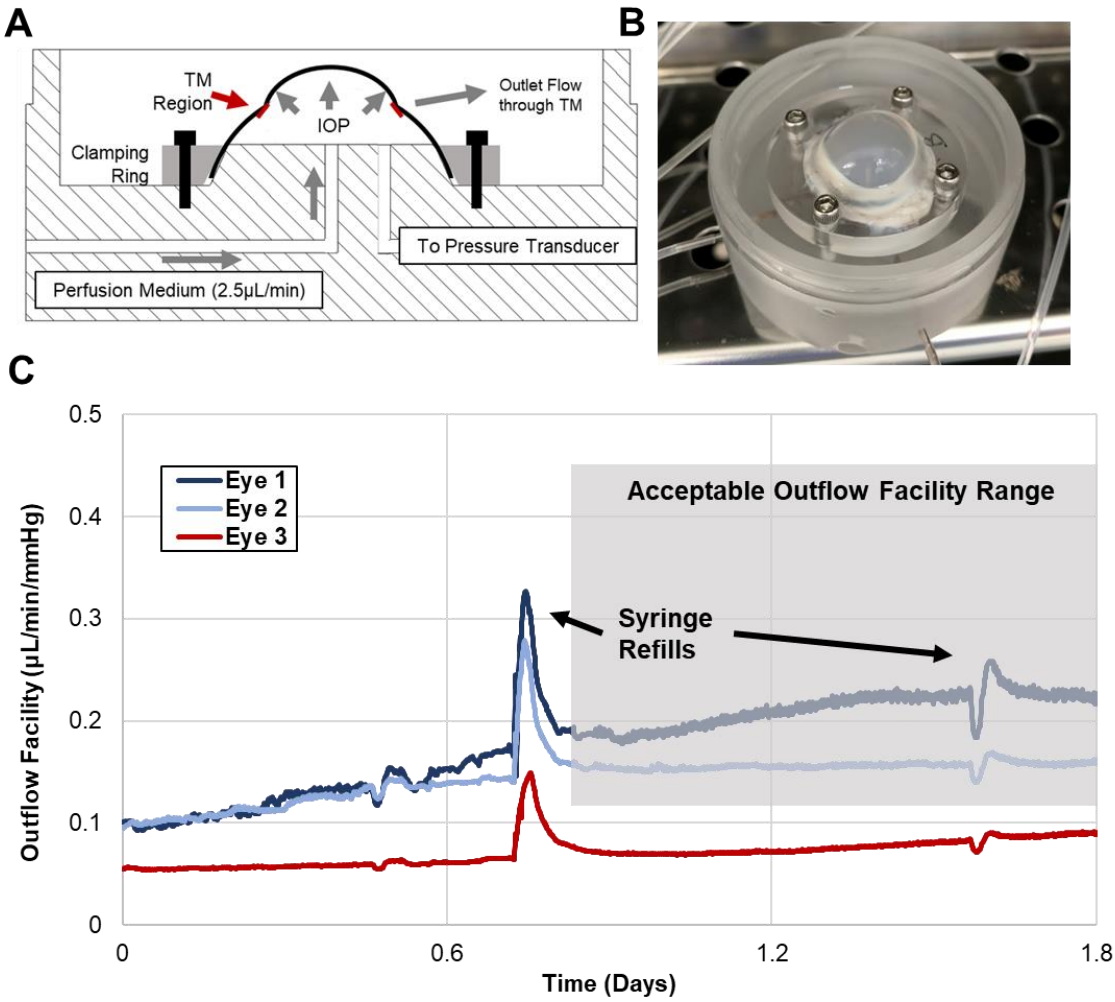


**Figure 36. Porcine Anterior Chamber Organ Culture Setup. (A)** Schematic diagram of porcine anterior segment clamped in organ culture dish. Red region indicates TM. (B) Porcine tissue in organ culture dish after 10 days of media perfusion. (C) Representative outflow facility for three porcine eyes. Pressures typically stabilize after 1-2 days, at which point any eyes outside of the healthy outflow facility range (0.125 to 0.45 µL/min/mmHg) were discarded.

### *6.3.6 Organ Culture Characterization*

#### 6.3.6.1 IOP Homeostasis Challenge

After a 24 hour IOP stabilization period following $H_2O_2$ treatment, the organ-culture perfusion flow rate was increased to 5µL/min for 72 hours to create a “2x flow challenge”. A similar 2x pressure challenge has been shown to result in higher facilities

in normal human anterior segments, presumably due to the TM adapting so as to restore a homeostatic pressure level. This adaptive response was absent or blunted in glaucomatous anterior segments (Abu-Hassan et al., 2015), and thus the flow challenge response has been interpreted as a measure of TM function. Our 2x flow challenge follows a similar approach and is easier to implement in a pump-based system, such as used in this work. When organ-cultured anterior segments are challenged in this way, we expect that pressure will spike and eventually reduce to baseline values in control anterior segments with functional TMs. On the other hand, we expect that $H_2O_2$-treated anterior segments will not adapt, so that IOP will remain elevated (diagrammed in Figure 37).

#### 6.3.6.2 Live Dead Assessment in Organ Culture

After a 24 hour IOP stabilization period following $H_2O_2$ treatment, anterior segments were live-dead stained to determine cellular viability. Anterior segments were removed from organ culture and washed once with PBS and incubated with 2 µM calcein-AM and 4 µM ethidium homodimer-1 for 30 minutes. Live-dead stained tissue was imaged *en face* by confocal microscopy (LSM 700, Carl-Zeiss). Micrographs were captured as tile scans of z-stacks (to account for TM depth and height differences in the tissue) at 50x magnification. Maximum intensity projections (MIPs) were created from z-stacks for subsequent image quantification.

Brightfield overlays were also captured to identify the corneal margin, from which we determined the approximate location of the TM. Specifically, a 1 mm wide band around the corneal margin was taken as the TM region. Average fluorescent intensities for calcein-AM (live) and ethidium homodimer (dead) within the TM were determined from MIPs using ImageJ and compared to control, untreated eyes to determine the

impact of $H_2O_2$ on TM viability. Eyes were then fixed overnight using 10% buffered-formalin at 4°C.

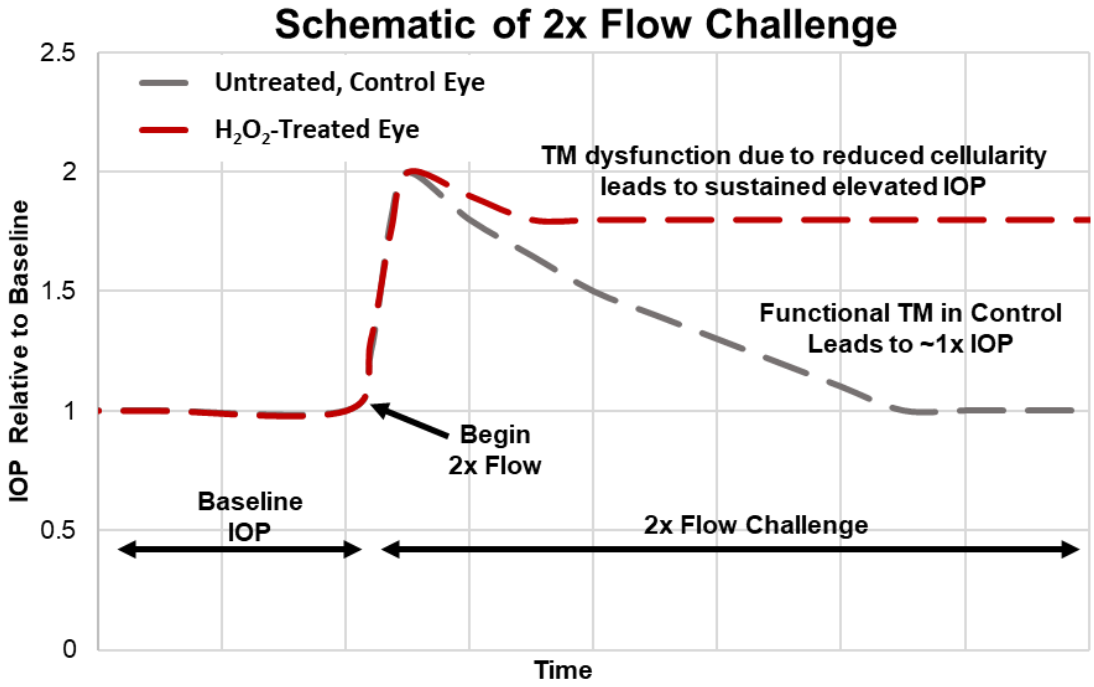


**Figure 37. Schematic of 2x Flow Challenge Paradigm**. After IOP stabilizes following $H_2O_2$ or media treatment for treated and control eyes, respectively ("Baseline IOP"), inlet flow rate is doubled ("2X Flow Challenge"). In control eyes, we expect the TM to adapt, so that IOP recovers to baseline IOP levels. In treated eyes, TM function is impaired and IOP does not return to baseline values.

6.3.6.3 Histological Processing

Anterior segment quadrants of fixed porcine eyes were cut into 3 mm wide meridional wedges and trimmed to isolate the outflow region. The tissue was dehydrated through an ethanol series, infiltrated and embedded in Histocryl media (Electron Microscopy Sciences). Two µm thick sections were cut on a Leica UC7 ultramicrotome with a glass knife and examined with a Leica DM6 Epifluorescent microscope. Sections were then stained with Toluidine blue (Sigma-Aldrich), mounted with Prolong Gold (ThermoFisher) and examined to assess cell morphology and tissue structure.

#### 6.3.6.4 Gelatin Zymography

During organ culture experiments, 1mL of media that had passed through the outflow tract was collected by aspiration from the organ culture dish daily ("conditioned outflow media"). The remaining media in the organ culture dish was discarded daily. Media was collected before $H_2O_2$ treatment and throughout the IOP homeostasis challenge and was stored at -80$^o$C prior to use.

Media was assessed for gelatinase activity (MMP-2 and MMP-9) by gelatin zymography (Chen and Platt, 2011; Raykin et al., 2017). Briefly, samples were supplemented with 4x non-reducing sample dye (250 mM Tris-HCl, pH 6.8; 40% (v/v) glycerol; 8% (w/v) SDS; and 0.01% (w/v) bromophenol blue) and were loaded at 5 µL per lane onto 10% SDS-polyacrylamide gels with 0.2% (w/v) gelatin. SDS-PAGE was run at 125 V for approximately 90 minutes at room temperature in running buffer (25 mM Tris, 192 mM Glycine, 0.1% (w/v) SDS, pH 8.3, BioRad). Gels were removed and placed in 2.5% (v/v) Triton X-100 to renature enzymes for 30 minutes, then incubated in 50 mM Tris-HCl, 150 mM NaCl, 10 mM $CaCl_2$, pH 7.8 overnight to allow sufficient time for gelatinolytic activity to occur. Following overnight incubation at 37$^o$C, the gels were incubated with Coomassie stain (0.05% (w/v) Coomassie Brilliant Blue G-250, 25% (v/v) methanol, 10% (v/v) acetic acid) for 1 hour, followed by destaining (4% (v/v) methanol, 8% (v/v) acetic acid) until clear bands were visible, at which time the gels were imaged. Total gelatinase activity was quantified using ImageQuant TL 8.1 (GE Healthcare Life Sciences).

### *6.3.7 Stem Cell Delivery to the TM*

To determine the effects of stem cells on the $H_2O_2$-treated TM, stem cells were injected into organ-cultured anterior segments 24 hours after $H_2O_2$ treatment. Adipose-

derived MSCs were detached from culture dishes with 0.05% Trypsin-EDTA, centrifuged and labeled by resuspending in 5μM carboxyfluorescein succinimidyl ester (CFSE, affymetrix eBioscience) in PBS. After incubating for 15 minutes at 37$^{o}$C, MSC media was added to quench any unreacted CFSE before injection into the anterior segment. Cells were resuspended in organ culture media, and 1 million cells in 500μL were injected (~10 second injection) through the cornea while anterior segments were pressure clamped at 6 to 12 mmHg by connection to an open reservoir. Perfusion at 2.5μL/min was resumed immediately after injection and continued overnight to allow time for cell delivery, after which anterior segments were removed from dishes and fixed in 10% buffered formalin. The TM was imaged *en face* at 100x magnification at locations where CFSE-stained MSCs were observed.

### *6.3.8 Statistics*

For *in vitro* experiments, at least 4 technical replicates for each of 2 pTM cell lines were assessed for each experiment setup. Analysis of variance (ANOVA, with post hoc Tukey test) was used to determine if untreated, control groups were significantly different from $H_2O_2$-treated groups. For *ex vivo* organ culture experiments, at least 6 eyes were assessed for every experimental condition. Similarly, analysis of variance (ANOVA, with post hoc Tukey test) was used to determine if untreated, control groups were significantly different from $H_2O_2$-treated groups. Differences in baseline IOP for control and $H_2O_2$-treated groups was determine by a paired Student's t-test. The significance threshold was taken as $p = 0.05$.

The use of ANOVA requires three assumptions to be satisfied: the outcome of interest must be continuous and measurements must be independent; the residuals must be normally distributed; and there must be homogenous variance between groups

("homoscedasticity"). For this study, all experimental variables were continuous. Uniform distribution and equal variances were routinely assessed as part of the ANOVA analysis (XLSTAT). Unfortunately, for situations in which there were small numbers of observations ($n < 5$), assessment of normality was unreliable. Further statistical analysis should be carried out to confirm the validity of these statistical tests.

## 6.4 Results

### *6.4.1 Effect of $H_2O_2$ on pTM Cell Viability in vitro*

Isolated pTM cells were treated with different concentrations of $H_2O_2$ for 1 hour and viability was measured by flow cytometry. Viability and $H_2O_2$ concentration were linearly correlated over a wide range (Figure 38A). Interestingly, cell viability continued to decrease beyond the initial 1 hour treatment with $H_2O_2$ until it stabilized at approximately 24 hours after $H_2O_2$ exposure (Figure 38B). Further, cellular viability was similar in three pTM cell lines following 1 hour treatment with 2 mM $H_2O_2$ and 24-hour incubation in organ culture media to account for extended $H_2O_2$ induced death (Figure 38C). We conclude that $H_2O_2$ treatment of pTM cells is capable of consistently producing titrated cell loss in culture.

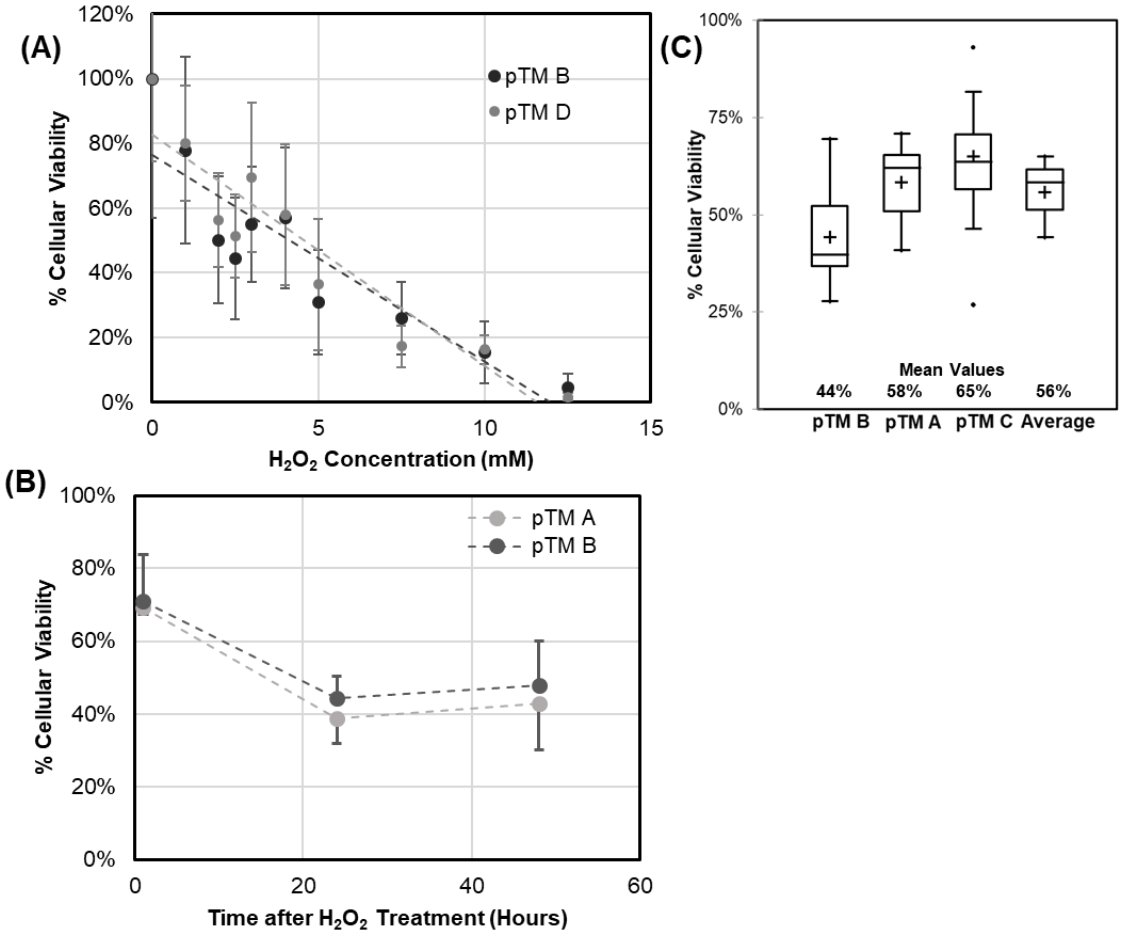


**Figure 38. Effects of $H_2O_2$ Treatment on pTM Cells *in vitro.* (A)** Effect of $H_2O_2$ concentration on pTM cell viability immediately after 1 hour exposure (n = 4 technical replicates). **(B)** Extended effects of 2mM $H_2O_2$ treatment for 1 hour on pTM cell viability, for two pTM cell lines (n=12 technical replicates). **(C)** Summary of effects of 1 hour, 2mM $H_2O_2$ treatment on 3 pTM cell lines (n=12 technical replicates). Box plot interpretation is as described in Figure 23. Mean values are shown for each pTM cell line in plot. Error bars denote standard deviation. All viability values were normalized to control conditions (no $H_2O_2$).

### *6.4.2 Functional assessment of $H_2O_2$-treated pTM cells*

To assess the effects of $H_2O_2$ treatment on pTM cell function, cells were treated with 2mM $H_2O_2$ for 1 hour and allowed to equilibrate for 24 hours. Alamar Blue staining indicated a significant decrease in metabolic activity following treatment (Figure 39A). Phagocytic activity after incubation with pHrodo *e.coli* particles was slightly reduced

following $H_2O_2$ treatment, but this did not reach statistical significance (Figure 39B). Similarly, $H_2O_2$-treated cells showed only minor changes in contractility, as assayed by a gel contraction assay (Figure 39C). We conclude that while metabolic activity is reduced, phagocytic and contractile properties of surviving pTM cells are not altered following $H_2O_2$ treatment.

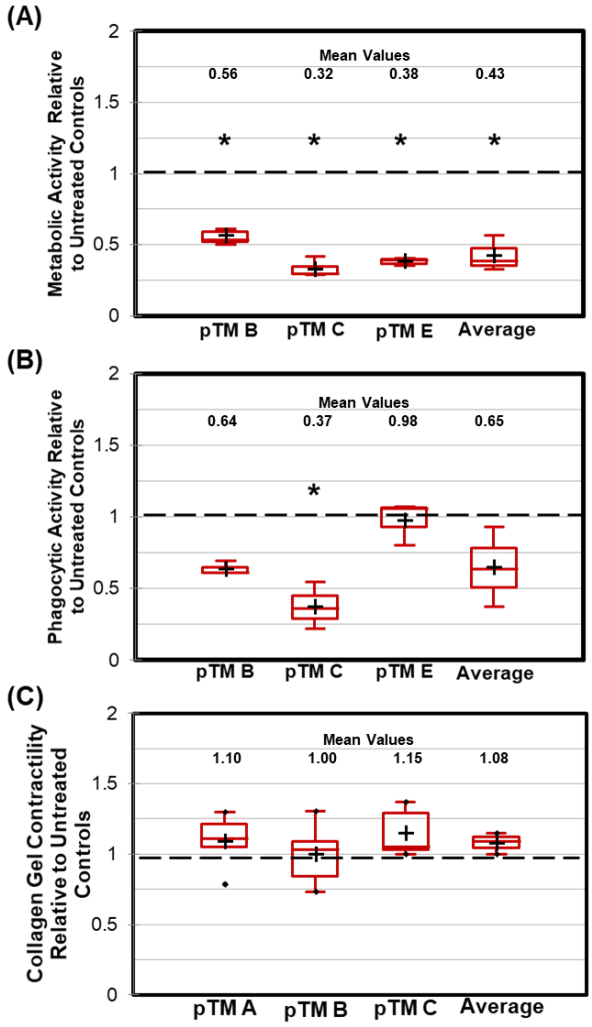


**Figure 39. Effect of $H_2O_2$ on pTM Cell Function.** pTM cells were treated with 2mM $H_2O_2$ for 1 hour. After 24 hours, pTM cells were tested for **(A)** metabolic activity (n=6 technical replicates), **(B)** phagocytic activity (n=3 technical replicates), and **(C)** collagen gel contractility (n=6 technical replicates). Black dashed lines denote untreated control results and error bars denote standard deviation. Box plot interpretation is as described in Figure 23. Significant differences (denoted by asterisks, $p < 0.05$) between $H_2O_2$-treated cells and untreated controls was determined by ANOVA, with post-hoc Tukey.

### *6.4.3 IOP homeostasis after $H_2O_2$ treatment*

After characterizing $H_2O_2$ treatment *in vitro*, experiments were translated to porcine organ-cultured anterior segments. Different $H_2O_2$ concentrations were perfused into porcine anterior segments for 1 hour followed by a stabilization period in which IOP returned to pre-treatment levels for both $H_2O_2$- treated and untreated experiments. Differences between baseline IOP values for Control and $H_2O_2$-treated eyes were not significant (Table 4). Perfusion flow rate was then doubled to evaluate the ability of the TM to respond to this “2x flow challenge”, as described in the Methods section. 2mM to 4mM $H_2O_2$ did not lead to significant TM dysfunction, i.e. elevated IOP eventually returned close to baseline levels following the 2x flow challenge (data not shown). However, 4.5mM $H_2O_2$ resulted in sustained IOP elevation for at least 3 days following the 2x flow challenge, indicating a loss of TM homeostatic response (Figure 40). This was further verified by gelatin zymography on effluent collected before and during the 2x flow challenge. Control eyes (no $H_2O_2$ exposure) exhibited significantly more gelatinase activity compared to $H_2O_2$-treated eyes (Figure 41) during the 2x flow challenge, indicating reduced extracellular remodeling capacity in $H_2O_2$-treated eyes. We conclude that 4.5 mM $H_2O_2$ is capable of disrupting IOP homeostasis in the porcine TM.

**Table 4. Baseline IOP for Control and $H_2O_2$-treated eyes.** Baseline IOP values were averaged for 10 hours of IOP readings for each untreated or H2O2-treated anterior segment (n = 9 for each condition) immediately prior to the 2x flow challenge. Average differences between each condition were not significant (p = 0.15) as determined by a paired Student's t-test. Note that control and H2O2-treated eyes were not generally from the same animal, but were obtained and perfused at the same time, and thus can be treated as a "pair" within the meaning of the paired t-test. Such "pairs" are referred to as a "cohort" in the table.

| Eye Cohort | Baseline IOP (mmHg) | | | |
|---|---|---|---|---|
| | Control | | $H_2O_2$-Treated | |
| | *Average* | *Standard Deviation* | *Average* | *Standard Deviation* |
| 1 | 6.2 | 0.3 | 13.2 | 0.3 |
| 2 | 15.8 | 0.8 | 19.3 | 0.7 |
| 3 | 19.8 | 0.4 | 11.3 | 0.4 |
| 4 | 17.9 | 1.2 | 14.9 | 0.6 |
| 5 | 15.8 | 0.5 | 10.8 | 0.2 |
| 6 | 19.8 | 0.4 | 10.5 | 0.7 |
| 7 | 15.9 | 0.4 | 9.0 | 0.4 |
| 8 | 17.1 | 0.3 | 13.1 | 0.6 |
| 9 | 10.4 | 0.4 | 10.3 | 0.4 |
| **Group mean ± SD** | **15.4 ± 4.4** | | **12.5 ± 3.1** | |

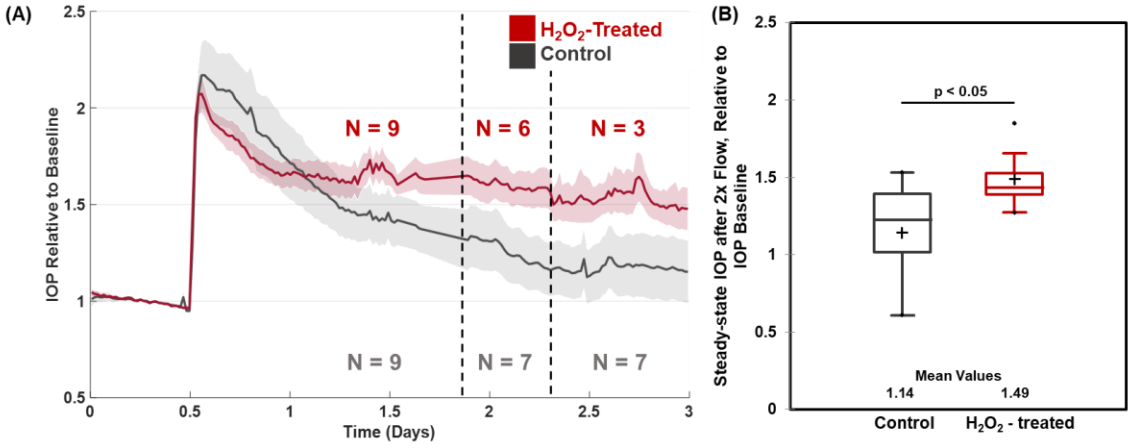


**Figure 40. 2x Perfusion Flow Challenge after $H_2O_2$ Treatment. (A)** Average IOP traces for $H_2O_2$-treated and control eyes. IOP traces are shown throughout the 2x perfusion flow challenge until IOP steady-state was reached. IOP was normalized to an eye-specific baseline IOP measured after treatment with $H_2O_2$ (experimental eyes) or media (control eyes); shaded region denotes standard error. N values indicate number

of eyes that have been averaged, accounting for different termination times for the experiments. (B) Normalized steady-state (~48 hours after H2O2 treatment) IOP after 2x flow challenge in $H_2O_2$-treated and control eyes (n=9 eyes for each). Box plot interpretation is as described in Figure 23. Mean values for control and $H_2O_2$-treated eyes are shown in plot. Significance between $H_2O_2$-treated and untreated eyes was determined by ANOVA, post-hoc Tukey.

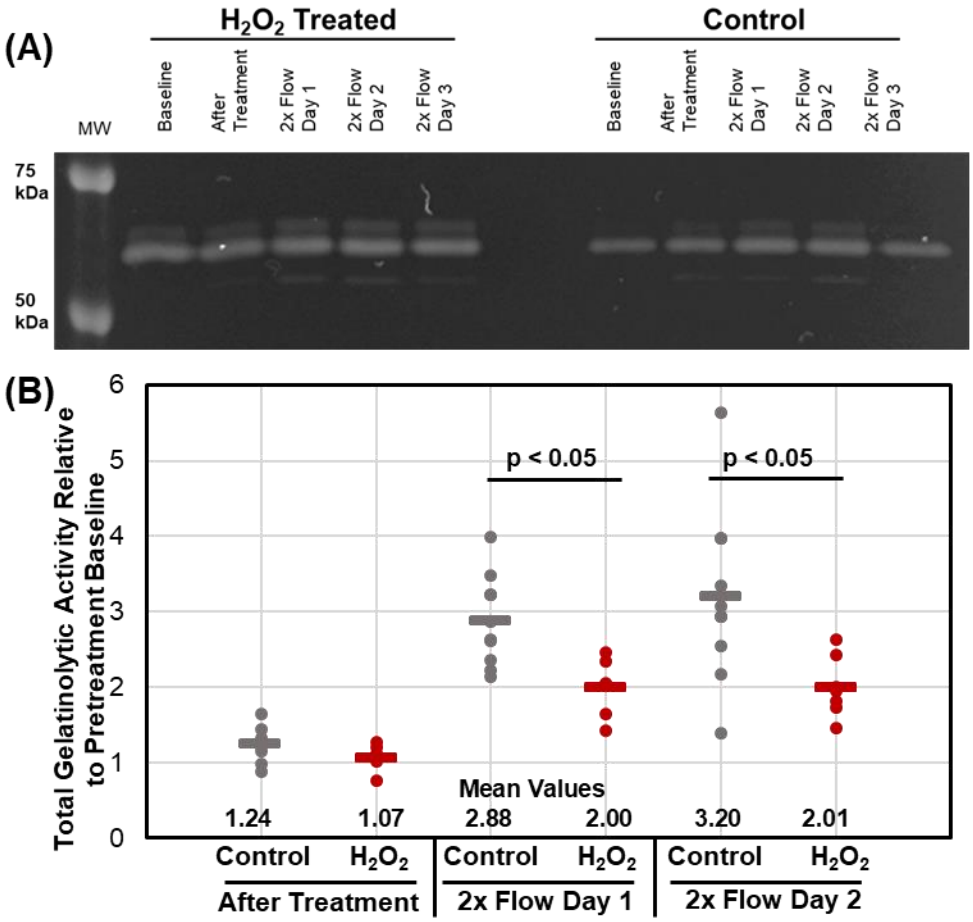


**Figure 41. Gelatinase Levels in Effluent Collected from Perfused Anterior Segments. (A)** Representative zymogram for effluent from control and $H_2O_2$-treated anterior segments. **(B)** Total gelatinolytic activity is shown relative to pretreatment activity (N > 7 biological replicates for each). 5 µL of sample was run for each time point, and, after quantifying band intensity, 2x flow results were doubled to reflect the increased flow rate. Individual data points are shown and horizontal bars denote means. Mean values for each experimental group are shown in plot. Significance between $H_2O_2$ treated and untreated eyes was determined by ANOVA, with post-hoc Tukey.

### *6.4.4 Live-Dead Assessment of Porcine TM After $H_2O_2$ Treatment*

Porcine TM tissue was assessed 24 hours after $H_2O_2$ treatment for cellular viability using calcein-AM and ethidium homodimer-1 staining. Reduced numbers of living cells and increased dead signal in the TM region of $H_2O_2$-treated eyes was observed compared to control, untreated eyes (Figure 42 A, B). $H_2O_2$ effects were highly segmental, resulting in certain regions appearing fully dead, while others showed minimal dead staining. This is likely due to the known segmental nature of outflow through the TM (Chang et al., 2014; Swaminathan et al., 2014). Live to dead fluorescent signal ratios were calculated for the entire TM region and the cornea. Although reduced live-dead ratios were consistently observed in $H_2O_2$-treated eyes, these differences did not reach statistical significance (Figure 42C).

However, dead staining may not properly capture reduced TM cell viability. Ethidium homodimer-1 was often not seen in regions of the TM which were also Calcein-AM negative. $H_2O_2$ damage is known to signal apoptosis in other tissues and eventual nucleus fragmentation, possibly resulting in minimal dead staining even though viability is reduced (Das et al., 2001; Liu et al., 2013; Nandi et al., 2010; Teramoto et al., 1999). As a result, live fluorescent signal intensities were compared to avoid inconsistencies in dead staining (Figure 42D). Significantly reduced live staining was observed in the TM region, while reduced live staining intensities in the cornea did not reach statistical significance.

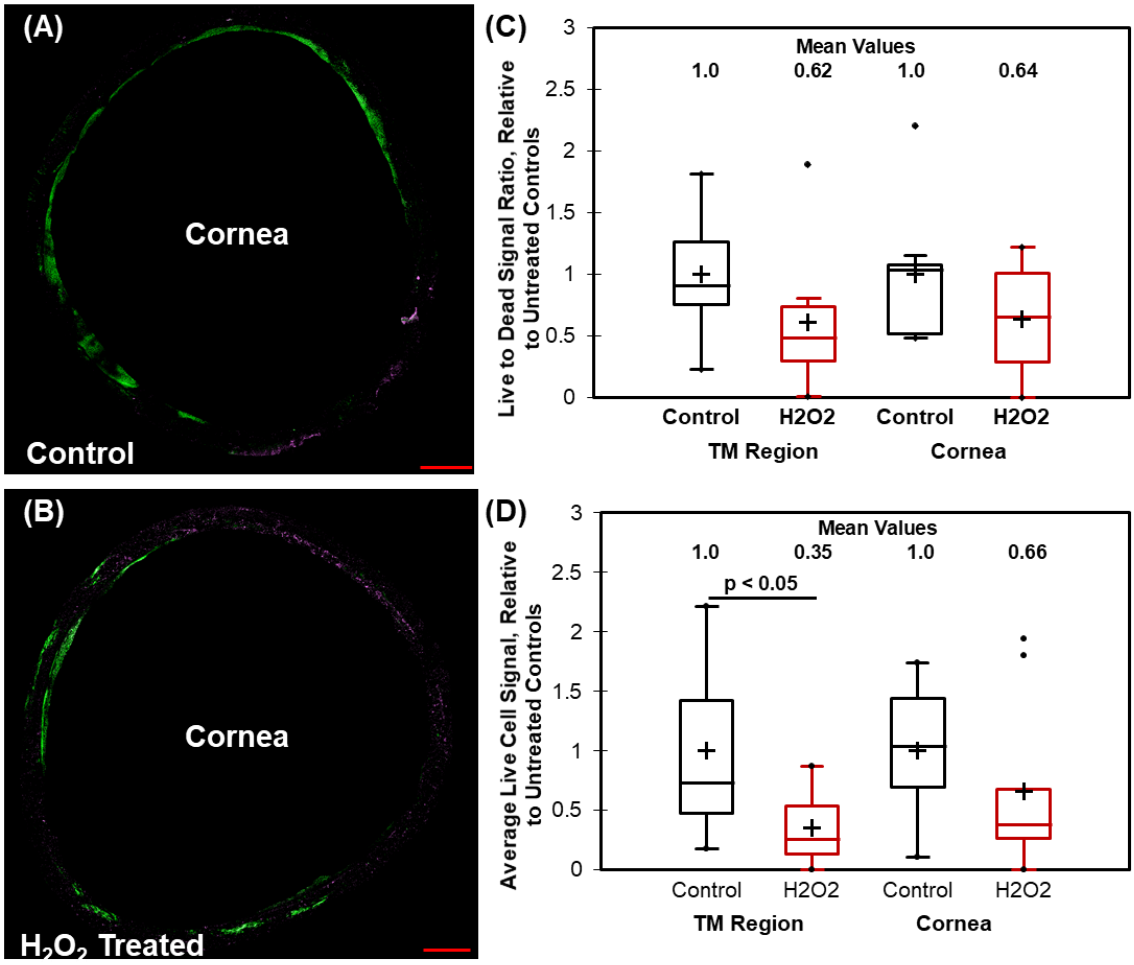


**Figure 42. Live-dead Staining in $H_2O_2$-treated Porcine Anterior Segments.** Representative *en face* images for the entire TM region of **(A)** control and **(B)** $H_2O_2$-treated porcine anterior segments. Calcein-AM (Green) and Ethidium homodimer (Red) denote live and dead cells, respectively. Scale bars are 2mm. **(C-D)** Quantification of Live and Dead fluorescent label intensities in the TM and cornea regions for $H_2O_2$-treated and control anterior segments (n=9 anterior segments each). **(C)** Live-dead fluorescent signal intensity ratios relative to controls and **(D)** Live cell signal intensities relative to controls are shown. Box plot interpretation is as described in Figure 23. Significance between $H_2O_2$-treated and untreated eyes was determined by ANOVA, with post-hoc Tukey.

### *6.4.5 Histological Assessment of $H_2O_2$-Treated Eyes*

Following $H_2O_2$ treatment, corneal swelling was qualitatively monitored in organ culture as evidenced by reduced corneal transparency. Corneal swelling indicates damage to the corneal endothelium and results in cytokine and MMP secretion that may

confound stem cell therapy results (Joyce et al., 2011; Li and Pflugfelder, 2005; Macdonald et al., 1987; Philipp et al., 2000). One day after $H_2O_2$ treatment, reduced transparency was not observed. For 2x flow experiments where $H_2O_2$ eyes were maintained for 3 – 4 days after treatment, corneal swelling was infrequent, similar to untreated eyes.

Sagittal sections from fixed porcine eyes after live-dead imaging were assessed to determine whether $H_2O_2$ treatment altered the TM microarchitecture. Tissue was stained with toluidine blue to identify cell nuclei and better visualize TM extracellular matrix. Two anterior segment quadrants from each of three $H_2O_2$-treated and untreated control eyes were processed. TM microarchitecture was not found to be disrupted by $H_2O_2$ when compared to untreated eyes (Figure 43). The number of cell nuclei in the TM were also similar between $H_2O_2$-treated and untreated eyes across all processed eyes. This is likely due to the highly segmental effects observed in $H_2O_2$-treated eyes.

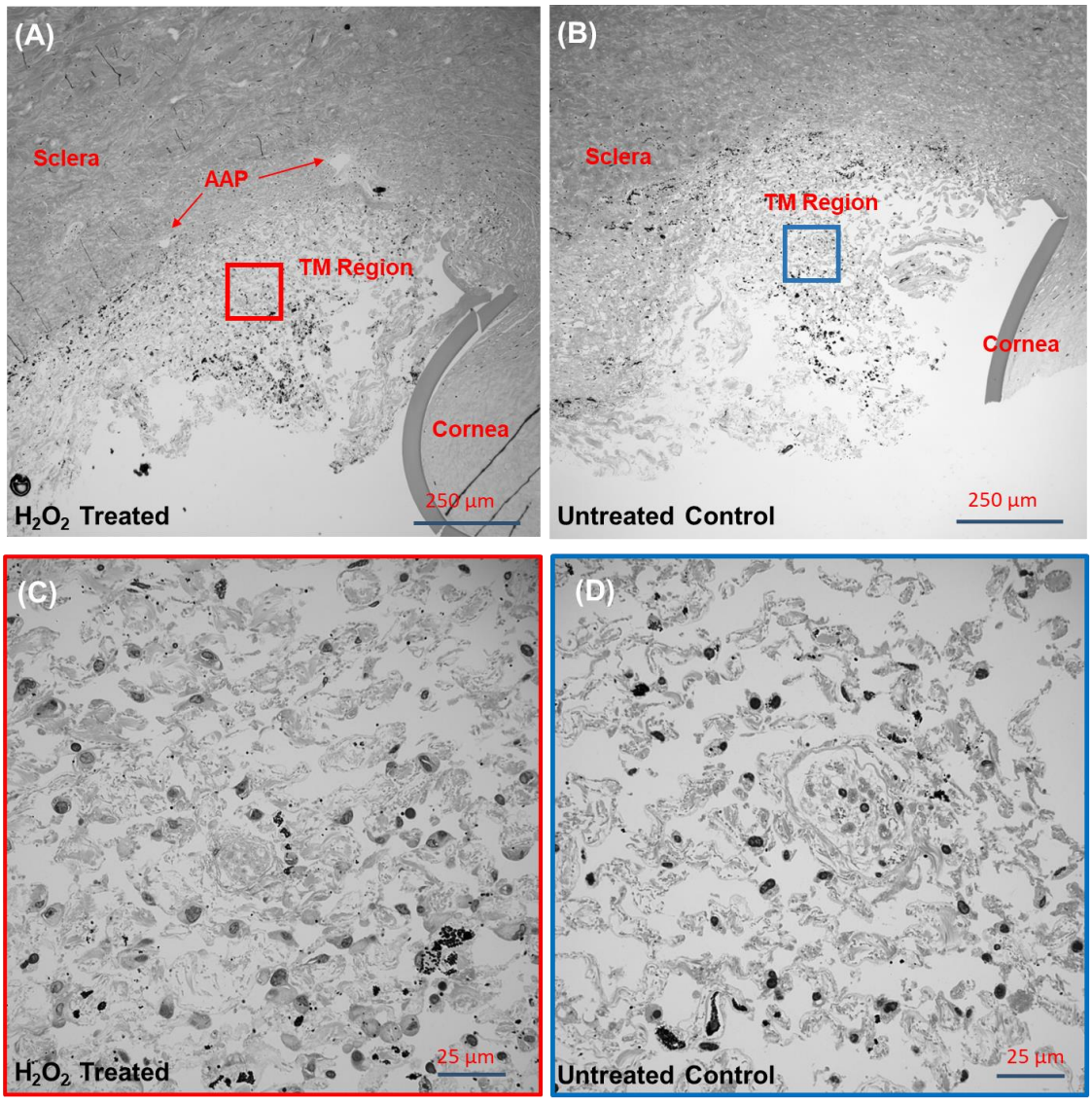


**Figure 43. Histological Assessment of TM After $H_2O_2$ Treatment.** Representative toluidine blue stained sagittal sections of the TM region for **(A,C)** $H_2O_2$-treated organ-culture porcine anterior segments and **(B,D)** untreated control anterior segments. **(A,B)** Lower magnification brightfield micrographs are labeled with relevant anatomical features for orientation (AAP = angular aqueous plexus, an analogue of Schlemm's canal in porcine eyes). Approximate zoomed regions are shown as blue and red boxes

### *6.4.6 MSC Delivery to $H_2O_2$-Treated Anterior Segments*

Stem cells were delivered into anterior segments following $H_2O_2$ treatment to determine what effect, if any, $H_2O_2$ damage had on stem cell engraftment in the TM. MSCs were consistently found at similar amounts in $H_2O_2$-treated anterior segments and

untreated anterior segments. However, MSC morphology in the TM was noticeably different in $H_2O_2$-treated eyes, with more elongated cellular bodies compared to a rounded morphology in control eyes (Figure 44). This suggests that MSC engraftment in the TM occurred more prevalently in $H_2O_2$-treated eyes compared to control eyes. This was likely due to there being more binding sites in the TM of $H_2O_2$-treated anterior segments due to lower TM cellularity.

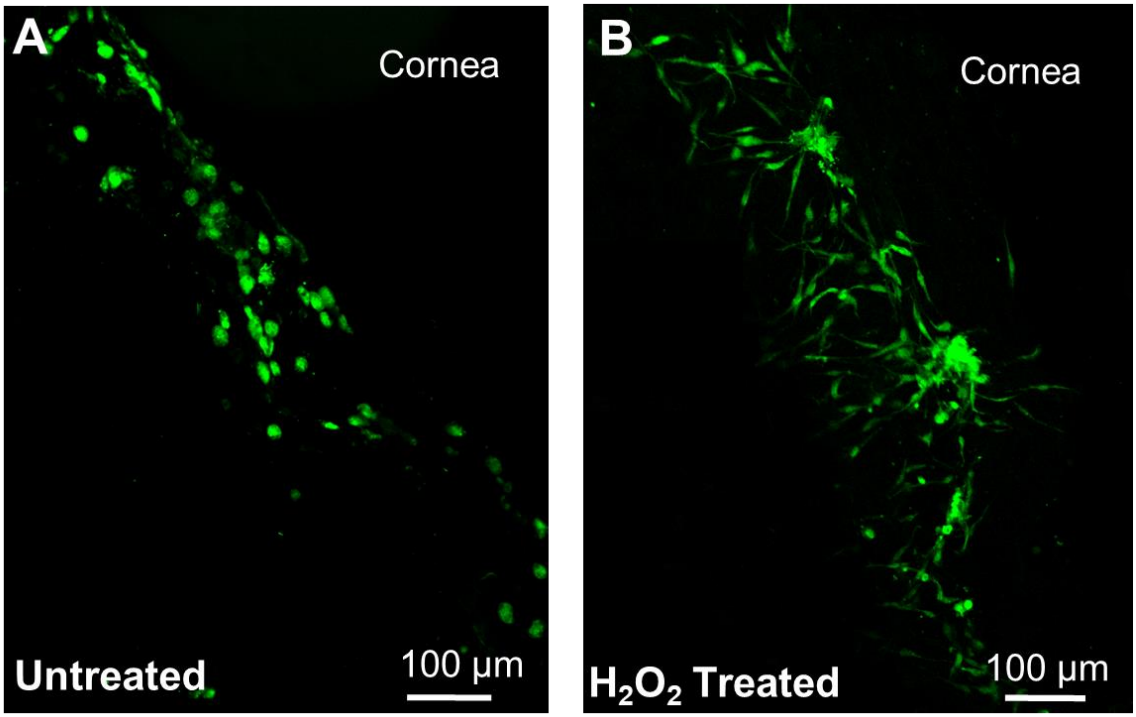


**Figure 44. MSC Delivery to the TM in $H_2O_2$-Treated Anterior Segments.** CFSE-labeled MSCs were injected at 1 million cells per anterior segment and allowed to adhere overnight. Representative *en face* fluorescent micrographs for **(A)** untreated and **(B)** $H_2O_2$-treated organ culture anterior segments.

### 6.5 Discussion

This work demonstrates that it is possible to create a pathophysiologically accurate model of TM dysfunction in commonly available porcine anterior segments. Such a model is expected to be useful for several reasons. First, reduced TM cellularity

in glaucoma is believed to cause tissue dysfunction, specifically increased outflow resistance leading to OHT. As a result, this model offers a suitable platform to test stem cell therapies to restore the cellularity and functionality of the TM. In this context, use of porcine anterior segments is attractive since they offer a more manageable TM size compared to rodents, and findings in this model are likely highly translatable to human eyes when eye size-dependent physical factors influencing stem cell delivery are considered.

We used $H_2O_2$ treatment, an acute model of oxidative stress, to induce TM dysfunction in porcine anterior segment organ culture. Oxidative stress is believed to contribute to the pathogenesis of POAG, and leads to DNA, mitochondrial, and extracellular matrix damage in the TM (Clopton and Saltman, 1995; Knepper et al., 1996; Sacca et al., 2005; Tanito et al., 2016; Yu et al., 2008; Zhao et al., 2016). Interestingly, the TM has been found to be more susceptible to oxidative damage than other anterior ocular tissues, such as the cornea (Izzotti et al., 2009).

Key features of this model include reduced TM cellularity, and a concomitant loss of IOP homeostasis after a flow challenge. Consistent with this loss of homeostasis, we observed reduced gelatinase (MMP-2 and MMP-9) activity in $H_2O_2$-treated anterior segments. TM cells have been previously shown to upregulate secretion of MMP-2, -3 and -14 after IOP elevation, all of which are involved in extracellular matrix remodeling (De Groef et al., 2013). Reduction of MMP-2 expression, as observed by gelatin zymography in media effluent, indicates reduced tissue remodeling after elevated IOP in $H_2O_2$ eyes. The reduction in gelatinase activity was not in response to $H_2O_2$ treatment, as media effluent collected before and after $H_2O_2$ treatments showed similar gelatinase activity.

Organ-cultured porcine anterior segments had a significant reduction in cellularity after 4.5mM $H_2O_2$ treatment, as determined by live-dead staining, with cell viability reduced to c. 35% of that seen in controls. This seems to be somewhat more severe than the situation in human glaucomatous tissue, where approximately 30% fewer cells are found in the TM of POAG donors compared to similarly aged healthy eyes (Alvarado et al., 1984; Liton et al., 2005). However, the porcine anterior segments are presumably from young adult pigs, and TM cells are lost continuously with age. Considering a reduction in TM cellularity associated with aging from 0 to 80 years of approximately 60% (Alvarado et al., 1981), we estimate that there are approximately 70 to 80% fewer TM cells in aged glaucomatous human eyes compared to young, healthy human tissue. This figure is quite close to the 65% mean decrease we observed after $H_2O_2$ treatment in porcine anterior segments. Interestingly, loss of IOP homeostasis was utilized as our endpoint to determine the optimal $H_2O_2$ concentration, which perhaps not coincidentally resulted in a TM cellularity reduction similar to that seen in human glaucoma in aged eyes.

Importantly, our acute oxidative stress model resulted in minimal unwanted side effects on tissue morphology and the function of the remaining TM cells. For example, histology revealed a grossly normal-appearing TM after $H_2O_2$ treatment, suggesting tissue integrity was maintained, essential for assessing stem cell therapies. However, due to cellularity effects of $H_2O_2$ being segmental, more histological assessment is needed to confirm regions of damage are properly assessed. Second, phagocytic and cell contractility functions of the remaining TM cells were not significantly altered after $H_2O_2$ treatment. This is broadly consistent with the clinical situation, where phagocytic function appears to be preserved in TM cells during glaucoma (Matsumoto and Johnson, 1997).

Our oxidative stress model was also compatible with MSC delivery to the TM. In fact, $H_2O_2$-treated eyes showed better engraftment of MSCs compared to delivery in untreated eyes. After $H_2O_2$ treatment, TM cell numbers were reduced to 35%, compared to untreated, control anterior segments. We believe this reduced cellularity “made available” binding sites in the TM for MSCs to adhere to, which were not available in untreated, control eyes. For stem cell therapies, proper MSC engraftment is essential for subsequent differentiation and refunctionalization of the TM.

There are several limitations to this model. $H_2O_2$-induced damage of the TM was non-specific and, as a result, other anterior chamber tissues exhibited reduced cellularity. This might lead to confounding factors when testing cell therapies. The non-specificity of $H_2O_2$ effects also means this approach is likely not suitable for *in vivo* applications. Nonetheless, this model shows great promise for testing mesenchymal stem cell therapies in cultured porcine anterior segments.

# CHAPTER 7. CONCLUSIONS

Mesenchymal stem cell therapies represent a new, largely unstudied, therapeutic approach for repairing the TM in glaucoma, and, as such, methods and procedures for assessing differentiation, delivering cells to the eye, and assessing these cells' therapeutic potential for glaucoma have not yet been established. The objective of this thesis was to develop these essential first steps so that mesenchymal stem cell therapies for glaucoma can be properly assessed and implemented. Towards this objective, four specific aims were defined, and conclusions, limitations, and future directions from each aim are described below:

**Specific Aim 1:** Characterize differences between mesenchymal stem cells and trabecular meshwork cells at the RNA, protein, and functional levels

A first step towards developing MSC therapies for glaucoma is confirming that MSCs are capable of differentiation to a TM-like cell phenotype. However, this step cannot be achieved without first standardizing the assessment of differentiation. Using human MSCs and TM cells, we characterized differences at the messenger (RT-qPCR), protein (western blotting, flow cytometry), and functional (gel contractility and phagocytosis) levels. RT-qPCR offered a relatively high-throughput assay for initial assessment of differentiation, while measurement of myocilin protein expression after dexamethasone treatment was in accordance with standard TM cell characterization protocols. MSC therapies will only be viable if differentiated cells are functionally similar to TM cells, and these methods allow for testing contractile and phagocytic properties, key TM functions *in vivo*.

With differentiation assessment standardized in this manner, future research can examine MSC differentiation to a TM-like cell phenotype through co-culture with human or porcine TM cells. Co-culture conditions have been used to differentiate induced pluripotent stem cells into TM cells, so this is a natural starting point for MSC differentiation (Abu-Hassan et al., 2015; Ding et al., 2014). Three different schemes will be used to differentiate MSCs, each representing a different degree of co-culture interaction. MSCs and TM cells can be grown together to allow differentiation to be driven by cell-cell interactions, paracrine signaling, and innately secreted proteins from TM cells. Cell-cell interaction can be removed by growing TM cells in Transwell inserts so that both cell types share media but are not in contact with each other. Further isolation is possible by treating MSCs with conditioned media from TM cells grown alone to assess the role of only innate protein secretion. These experiments will provide insight into whether MSCs can differentiate into TM cells as well as the required level of interaction to induce a TM cell phenotype.

**Specific Aim 2:** Implement an ultrasound-photoacoustic imaging platform for visualizing mesenchymal stem cell delivery and retention in the trabecular meshwork

We implemented an ultrasound and photoacoustic imaging platform capable of non-invasive, real-time detection of MSC delivery to TM. MSC delivery, based on two previous studies (Manuguerra-Gagne et al., 2013; Roubeix et al., 2015), is a challenging process, and this platform has the potential to expedite optimization of MSC delivery and simplify therapeutic assessment. Spectroscopic PA imaging allowed for detection of gold nanosphere-labeled MSCs, while ultrasound imaging provided anatomical details of the anterior segment. MSCs were tracked during injection into porcine eyes and were distinguishable from background PA signals from melanin-rich tissues for up to 5 hours after injection. However, MSC distribution in the TM region obtained with US-PA imaging

was not entirely consistent with the distribution measured using conventional fluorescent microscopy, and this remains an area of future work.

While US-PA imaging has the potential to non-invasively track MSC delivery, as an alternative to histology and fluorescent microscopy, additional studies are needed to improve TM imaging and correlation with more standard fluorescent imaging. Currently, delivering light to the TM region is difficult, due to the TM being recessed in the anterior chamber angle and the lens naturally focusing light away from the angle. Results from this study were mostly conducted with dissected eyes to bypass this light delivery hurdle. However, such an approach is not suitable for in vivo studies. To improve light delivery, a gonio lens, a commonly used device for reflecting laser light delivery to the anterior chamber angle in glaucoma therapies, can be used (Barkana and Belkin, 2007; Ho et al., 2009).

While US-PA and fluorescent imaging of MSC in the TM were somewhat consistent, there was high variability. This could be due to a number of confounding factors present in imaging complex porcine tissues with US-PA. We suggest simplifying the problem by first imaging labelled cells in gelatin phantoms, instead of in porcine eyes. MSCs will be placed in gelatin constructs and imaged by US-PA and fluorescence microscopy. Correlations between these two imaging modalities will be examined to determine whether variation is reduced, and to better “calibrate” the US-PA imaging of labelled cells.

Finally, longitudinal studies will be conducted to properly track MSC dynamics after delivery. It is unknown whether MSCs are retained long-term in the TM, whether they migrate within in the TM over time, and/or whether they proliferate *in situ.* Unlike fluorescent microscopy, US-PA imaging has the potential to track each of these

possibilities in the same experimental eye. MSC delivery and *in vivo* experiments are inherently variable, so being able to assess multiple time points in a single eye will simplify translation of MSC therapies for the TM.

**Specific Aim 3:** Improve mesenchymal stem cell delivery to the trabecular meshwork using magnetic nanoparticles

While US-PA allows for monitoring MSC delivery to the TM, it does not improve delivery efficiency. In fact, US-PA imaging results suggested that when cells were delivered passively by aqueous outflow, most MSCs fell under the action of gravity, settling on the anterior lens and iris. Thus, we assessed whether magnetically steered delivery of MSCs labeled with Prussian blue nanocubes (PBNCs) led to a better outcome. PBNCs were found to be suitable for MSC labeling, resulting in minimal toxicity effects in MSCs and no detectable impact on the cell's ability to differentiate toward adipogenic or osteogenic lineages. To magnetically steer MSCs to the TM, larger 200nm PBNCs were found to be most effective. Further, magnetic steering was rapid, with magnetic exposure times of as little as 15 minutes showing large effects on MSC delivery. One key issue in passive, conventional MSC delivery to the TM is segmental delivery to active flow regions of the TM. Magnetic steering of MSCs using a ring magnet resulted in relatively uniform delivery around the entire TM circumference. This approach for enhancing cell delivery has the potential to improve MSC-based therapies for the TM.

Future work will use PBNCs in the US-PA platform described in Specific Aim 2. This, however, will only be possible if PBNC-MSCs are distinguishable from endogeneous PA signal. Experiments similar to our AuNS-MSC experiments will thus be conducted to confirm PBNC-MSCs can be tracked and that results agree with fluorescence microscopy. In addition, PBNC labeling will be used in rodents to facilitate

in vivo delivery of MSCs to the TM. Magnet design and placement, and exposure duration, will need to be optimized for delivery to a smaller eye. Fortunately, radial-pulling ring magnets are commercially available that fit the smaller rodent eye, which was not the case for porcine eye.

**Specific Aim 4:** Develop an oxidative stress-derived porcine organ-culture glaucoma model mimicking trabecular meshwork damage and cell loss

Most current glaucoma models do not replicate the reduced TM cellularity seen in human glaucoma. Instead, existing models permanently damage or clog the outflow region, which is not suitable for assessing TM stem cell therapies. Here, we developed a porcine organ-culture model and used hydrogen peroxide to induce oxidative stress in the trabecular meshwork, thus partially decellularizing the TM. Following hydrogen peroxide treatment, eyes were challenged with increased fluid flow to assess the TM's ability to homeostatically maintain IOP. In response to this challenge, control eyes were able to increase outflow through the TM via MMP-mediated remodeling, while hydrogen peroxide-treated eyes were not able to do so. Further, live-dead staining and histology confirmed reduced TM cellularity in treated eyes without extensive structural damage to the TM, similar to the situation in human glaucoma. As a result, this glaucoma model is suitable for testing stem cell therapies to assess their potential for restoring function to the TM.

Future work will use this organ-culture model to assess actual MSC therapies. Hydrogen peroxide-treated anterior segments should be characterized at relevant time points for MSC differentiation. Ideally, MSCs will be injected into hydrogen peroxide-damaged anterior segments, and, after engraftment, MSCs will differentiate into a TM cell-like phenotype. However, the time course for this process is unknown until co-

culture differentiation experiments are conducted. Experiments with hydrogen peroxide-treated anterior segments have not been extended beyond one week after hydrogen peroxide delivery. If longer time points are needed, porcine anterior segments need to be characterized for TM dysfunction, viability and structural integrity for longer durations. We do not anticipate any issues for durations less than 3-4 weeks. However, maintaining viable anterior segments in organ culture beyond 3-4 weeks is very difficult. As an alternative, should longer time points be problematic for this model, MSCs could be differentiated *in vitro* to TM cells prior to injection.

**Final Thoughts**

This dissertation has taken the first steps towards testing future MSC-based therapies for repairing the glaucomatous TM. The findings from this dissertation will allow researchers to define initial *in vitro* differentiation, optimize delivery, and assess efficacy of proposed therapies for the TM, bringing clinical translation of MSC therapies for the glaucomatous TM closer to reality.

# REFERENCES


Abu-Hassan, D.W., Acott, T.S., and Kelley, M.J. (2014a). The Trabecular Meshwork: A Basic Review of Form and Function. J Ocul Biol *2*.

Abu-Hassan, D.W., Li, X., Ryan, E.I., Acott, T.S., and Kelley, M.J. (2014b). Induced pluripotent stem cells restore function in a human cell loss model of open-angle glaucoma. Stem Cells.

Abu-Hassan, D.W., Li, X., Ryan, E.I., Acott, T.S., and Kelley, M.J. (2015). Induced pluripotent stem cells restore function in a human cell loss model of open-angle glaucoma. Stem Cells *33*, 751-761.

Acott, T.S., and Kelley, M.J. (2008). Extracellular matrix in the trabecular meshwork. Exp Eye Res *86*, 543-561.

Acott, T.S., Kelley, M.J., Keller, K.E., Vranka, J.A., Abu-Hassan, D.W., Li, X., Aga, M., and Bradley, J.M. (2014). Intraocular pressure homeostasis: maintaining balance in a high-pressure environment. J Ocul Pharmacol Ther *30*, 94-101.

Acott, T.S., Samples, J.R., Bradley, J.M., Bacon, D.R., Bylsma, S.S., and Van Buskirk, E.M. (1989). Trabecular repopulation by anterior trabecular meshwork cells after laser trabeculoplasty. Am J Ophthalmol *107*, 1-6.

Aillon, K.L., Xie, Y., El-Gendy, N., Berkland, C.J., and Forrest, M.L. (2009). Effects of nanomaterial physicochemical properties on in vivo toxicity. Adv Drug Deliv Rev *61*, 457-466.

Alvarado, J., Murphy, C., and Juster, R. (1984). Trabecular meshwork cellularity in primary open-angle glaucoma and nonglaucomatous normals. Ophthalmology *91*, 564-579.

Alvarado, J., Murphy, C., Polansky, J., and Juster, R. (1981). Age-related changes in trabecular meshwork cellularity. Invest Ophthalmol Vis Sci *21*, 714-727.

Asrani, S., Zeimer, R., Wilensky, J., Gieser, D., Vitale, S., and Lindenmuth, K. (2000). Large diurnal fluctuations in intraocular pressure are an independent risk factor in patients with glaucoma. J Glaucoma *9*, 134-142.

Bachmann, B., Birke, M., Kook, D., Eichhorn, M., and Lutjen-Drecoll, E. (2006). Ultrastructural and biochemical evaluation of the porcine anterior chamber perfusion model. Invest Ophthalmol Vis Sci *47*, 2011-2020.

Baleriola, J., Garcia-Feijoo, J., Martinez-de-la-Casa, J.M., Fernandez-Cruz, A., de la Rosa, E.J., and Fernandez-Durango, R. (2008). Apoptosis in the trabecular meshwork of glaucomatous patients. Mol Vis *14*, 1513-1516.

Barbero, A., Grogan, S., Schafer, D., Heberer, M., Mainil-Varlet, P., and Martin, I. (2004). Age related changes in human articular chondrocyte yield, proliferation and post-expansion chondrogenic capacity. Osteoarthritis Cartilage *12*, 476-484.

Barkana, Y., and Belkin, M. (2007). Selective laser trabeculoplasty. Surv Ophthalmol *52*, 634-654.

Battista, S.A., Lu, Z., Hofmann, S., Freddo, T., Overby, D.R., and Gong, H. (2008). Reduction of the available area for aqueous humor outflow and increase in meshwork herniations into collector channels following acute IOP elevation in bovine eyes. Invest Ophthalmol Vis Sci *49*, 5346-5352.

Berens, P. (2009). CircStat: A MATLAB Toolbox for Circular Statistics. J Stat Softw *31*, 1-21.

Bhattacharya, S.K., Gabelt, B.T., Ruiz, J., Picciani, R., and Kaufman, P.L. (2009). Cochlin expression in anterior segment organ culture models after TGFbeta2 treatment. Invest Ophthalmol Vis Sci *50*, 551-559.

Bianco, P., Riminucci, M., Gronthos, S., and Robey, P.G. (2001). Bone marrow stromal stem cells: nature, biology, and potential applications. Stem Cells *19*, 180-192.

Bieback, K., Hecker, A., Kocaomer, A., Lannert, H., Schallmoser, K., Strunk, D., and Kluter, H. (2009). Human alternatives to fetal bovine serum for the expansion of mesenchymal stromal cells from bone marrow. Stem Cells *27*, 2331-2341.

Bill, A. (1989). Uveoscleral drainage of aqueous humor: physiology and pharmacology. Prog Clin Biol Res *312*, 417-427.

Boisselier, E., and Astruc, D. (2009). Gold nanoparticles in nanomedicine: preparations, imaging, diagnostics, therapies and toxicity. Chem Soc Rev *38*, 1759-1782.

Bradley, J.M., Kelley, M.J., Rose, A., and Acott, T.S. (2003). Signaling pathways used in trabecular matrix metalloproteinase response to mechanical stretch. Invest Ophthalmol Vis Sci *44*, 5174-5181.

Braunger, B.M., Fuchshofer, R., and Tamm, E.R. (2015). The aqueous humor outflow pathways in glaucoma: A unifying concept of disease mechanisms and causative treatment. Eur J Pharm Biopharm *95*, 173-181.

Brubaker, R.F. (1970). The measurement of pseudofacility and true facility by constant pressure perfusion in the normal rhesus monkey eye. Invest Ophthalmol *9*, 42-52.

Brubaker, R.F. (1991). Flow of aqueous humor in humans [The Friedenwald Lecture]. Invest Ophthalmol Vis Sci *32*, 3145-3166.

Buller, C., Johnson, D.H., and Tschumper, R.C. (1990). Human trabecular meshwork phagocytosis. Observations in an organ culture system. Invest Ophthalmol Vis Sci *31*, 2156-2163.

Cairns, J.E. (1968). Trabeculectomy. Preliminary report of a new method. Am J Ophthalmol *66*, 673-679.

Cellini, L., Grande, R., Di Campli, E., Di Bartolomeo, S., Di Giulio, M., Robuffo, I., Trubiani, O., and Mariggio, M.A. (2008). Bacterial response to the exposure of 50 Hz electromagnetic fields. Bioelectromagnetics *29*, 302-311.

Chamberlain, G., Fox, J., Ashton, B., and Middleton, J. (2007). Concise review: mesenchymal stem cells: their phenotype, differentiation capacity, immunological features, and potential for homing. Stem Cells *25*, 2739-2749.

Chang, J.Y., Folz, S.J., Laryea, S.N., and Overby, D.R. (2014). Multi-scale analysis of segmental outflow patterns in human trabecular meshwork with changing intraocular pressure. J Ocul Pharmacol Ther *30*, 213-223.

Chen, B., and Platt, M.O. (2011). Multiplex zymography captures stage-specific activity profiles of cathepsins K, L, and S in human breast, lung, and cervical cancer. J Transl Med *9*, 109.

Civan, M.M., and Macknight, A.D. (2004). The ins and outs of aqueous humour secretion. Exp Eye Res *78*, 625-631.

Clark, A.F., Steely, H.T., Dickerson, J.E., Jr., English-Wright, S., Stropki, K., McCartney, M.D., Jacobson, N., Shepard, A.R., Clark, J.I., Matsushima, H.*, et al.* (2001). Glucocorticoid induction of the glaucoma gene MYOC in human and monkey trabecular meshwork cells and tissues. Invest Ophthalmol Vis Sci *42*, 1769-1780.

Clopton, D.A., and Saltman, P. (1995). Low-level oxidative stress causes cell-cycle specific arrest in cultured cells. Biochem Biophys Res Commun *210*, 189-196.

Cook, C., and Foster, P. (2012). Epidemiology of glaucoma: what's new? Canadian journal of ophthalmology Journal canadien d'ophtalmologie *47*, 223-226.

Cook, J.R., Bouchard, R.R., and Emelianov, S.Y. (2011). Tissue-mimicking phantoms for photoacoustic and ultrasonic imaging. Biomed Opt Express *2*, 3193-3206.

Cook, J.R.D., Diego S. ; Kubelick, Kelsey P. ; Luci, Jeffrey ; Emelianov, Stanislav Y. (2017). Prussian blue nanocubes: multi-functional nanoparticles for multimodal imaging and image-guided therapy. Paper presented at: SPIE BiOS.

Cvekl, A., and Tamm, E.R. (2004). Anterior eye development and ocular mesenchyme: new insights from mouse models and human diseases. Bioessays *26*, 374-386.

Das, M., Mukherjee, S.B., and Shaha, C. (2001). Hydrogen peroxide induces apoptosis-like death in Leishmania donovani promastigotes. J Cell Sci *114*, 2461-2469.

De Groef, L., Van Hove, I., Dekeyster, E., Stalmans, I., and Moons, L. (2013). MMPs in the trabecular meshwork: promising targets for future glaucoma therapies? Invest Ophthalmol Vis Sci *54*, 7756-7763.

de Kater, A.W., Melamed, S., and Epstein, D.L. (1989). Patterns of aqueous humor outflow in glaucomatous and nonglaucomatous human eyes. A tracer study using cationized ferritin. Arch Ophthalmol *107*, 572-576.

Ding, Q.J., Zhu, W., Cook, A.C., Anfinson, K.R., Tucker, B.A., and Kuehn, M.H. (2014). Induction of trabecular meshwork cells from induced pluripotent stem cells. Invest Ophthalmol Vis Sci *55*, 7065-7072.

Dismuke, W.M., Liang, J., Overby, D.R., and Stamer, W.D. (2014a). Concentration-related effects of nitric oxide and endothelin-1 on human trabecular meshwork cell contractility. Exp Eye Res *120*, 28-35.

Dismuke, W.M., Liang, J., Overby, D.R., and Stamer, W.D. (2014b). Concentration-related. effects of nitric oxide and endothelin-1 on human trabecular meshwork cell contractility. Experimental eye research *120*, 28-35.

Dominici, M., Le Blanc, K., Mueller, I., Slaper-Cortenbach, I., Marini, F., Krause, D., Deans, R., Keating, A., Prockop, D., and Horwitz, E. (2006). Minimal criteria for defining multipotent mesenchymal stromal cells. The International Society for Cellular Therapy position statement. Cytotherapy *8*, 315-317.

Du, Y., Roh, D.S., Mann, M.M., Funderburgh, M.L., Funderburgh, J.L., and Schuman, J.S. (2012). Multipotent stem cells from trabecular meshwork become phagocytic TM cells. Invest Ophthalmol Vis Sci *53*, 1566-1575.

El May, A., Snoussi, S., Ben Miloud, N., Maatouk, I., Abdelmelek, H., Ben Aissa, R., and Landoulsi, A. (2009). Effects of static magnetic field on cell growth, viability, and differential gene expression in Salmonella. Foodborne Pathog Dis *6*, 547-552.

Erickson-Lamy, K., Rohen, J.W., and Grant, W.M. (1991). Outflow facility studies in the perfused human ocular anterior segment. Exp Eye Res *52*, 723-731.

Fautsch, M.P., and Johnson, D.H. (2006). Aqueous humor outflow: what do we know? Where will it lead us? Invest Ophthalmol Vis Sci *47*, 4181-4187.

Fong, C.Y., Gauthaman, K., and Bongso, A. (2010). Teratomas from pluripotent stem cells: A clinical hurdle. J Cell Biochem *111*, 769-781.

Gaasterland, D., and Kupfer, C. (1974). Experimental glaucoma in the rhesus monkey. Invest Ophthalmol *13*, 455-457.

Gabelt, B.T., Kiland, J., Tian, B., and Kaufman, P.L. (1995). Aqueous Humor: Secretion and Dynamics. In Duane's Foundations of Clinical Ophthalmology (Philadelphia: Lipincott-Raven).

Gagen, D., Filla, M.S., Clark, R., Liton, P., and Peters, D.M. (2013). Activated alphavbeta3 integrin regulates alphavbeta5 integrin-mediated phagocytosis in trabecular meshwork cells. Invest Ophthalmol Vis Sci *54*, 5000-5011.

Galanzha, E.I., Shashkov, E.V., Spring, P.M., Suen, J.Y., and Zharov, V.P. (2009). In vivo, noninvasive, label-free detection and eradication of circulating metastatic

melanoma cells using two-color photoacoustic flow cytometry with a diode laser. Cancer Res *69*, 7926-7934.

Gilda, J.E., and Gomes, A.V. (2013). Stain-Free total protein staining is a superior loading control to beta-actin for Western blots. Anal Biochem *440*, 186-188.

Gnecchi, M., Zhang, Z., Ni, A., and Dzau, V.J. (2008). Paracrine mechanisms in adult stem cell signaling and therapy. Circ Res *103*, 1204-1219.

Goel, M., Picciani, R.G., Lee, R.K., and Bhattacharya, S.K. (2010). Aqueous humor dynamics: a review. Open Ophthalmol J *4*, 52-59.

Gonzalez, P., Epstein, D.L., Luna, C., and Liton, P.B. (2006). Characterization of free-floating spheres from human trabecular meshwork (HTM) cell culture in vitro. Experimental Eye Research *82*, 959-967.

Gould, D.B., Smith, R.S., and John, S.W. (2004). Anterior segment development relevant to glaucoma. Int J Dev Biol *48*, 1015-1029.

Grant, W.M. (1958). Further studies on facility of flow through the trabecular meshwork. AMA Arch Ophthalmol *60*, 523-533.

Grant, W.M. (1963). Experimental aqueous perfusion in enucleated human eyes. Arch Ophthalmol *69*, 783-801.

Greenspan, P., Mayer, E.P., and Fowler, S.D. (1985). Nile red: a selective fluorescent stain for intracellular lipid droplets. J Cell Biol *100*, 965-973.

Grierson, I., and Howes, R.C. (1987). Age-related depletion of the cell population in the human trabecular meshwork. Eye *1 ( Pt 2)*, 204-210.

Gurwitz, J.H., Yeomans, S.M., Glynn, R.J., Lewis, B.E., Levin, R., and Avorn, J. (1998). Patient noncompliance in the managed care setting. The case of medical therapy for glaucoma. Med Care *36*, 357-369.

Hann, C.R., Bahler, C.K., and Johnson, D.H. (2005). Cationic ferritin and segmental flow through the trabecular meshwork. Invest Ophthalmol Vis Sci *46*, 1-7.

Hanna, J.H., Saha, K., and Jaenisch, R. (2010). Pluripotency and cellular reprogramming: facts, hypotheses, unresolved issues. Cell *143*, 508-525.

Ho, C.L., Lai, J.S., Aquino, M.V., Rojanapongpun, P., Wong, H.T., Aquino, M.C., Gerber, Y., Belkin, M., and Barkana, Y. (2009). Selective laser trabeculoplasty for primary angle closure with persistently elevated intraocular pressure after iridotomy. J Glaucoma *18*, 563-566.

Iscove, N.N., Barbara, M., Gu, M., Gibson, M., Modi, C., and Winegarden, N. (2002). Representation is faithfully preserved in global cDNA amplified exponentially from sub-picogram quantities of mRNA. Nat Biotechnol *20*, 940-943.

Ishikawa, M., Yoshitomi, T., Zorumski, C.F., and Izumi, Y. (2015). Experimentally Induced Mammalian Models of Glaucoma. Biomed Res Int *2015*, 281214.

Ito, A., Hibino, E., Kobayashi, C., Terasaki, H., Kagami, H., Ueda, M., Kobayashi, T., and Honda, H. (2005). Construction and delivery of tissue-engineered human retinal pigment epithelial cell sheets, using magnetite nanoparticles and magnetic force. Tissue Eng *11*, 489-496.

Izzotti, A., Sacca, S.C., Longobardi, M., and Cartiglia, C. (2009). Sensitivity of ocular anterior chamber tissues to oxidative damage and its relevance to the pathogenesis of glaucoma. Invest Ophthalmol Vis Sci *50*, 5251-5258.

Jin, H.J., Bae, Y.K., Kim, M., Kwon, S.J., Jeon, H.B., Choi, S.J., Kim, S.W., Yang, Y.S., Oh, W., and Chang, J.W. (2013). Comparative analysis of human mesenchymal stem cells from bone marrow, adipose tissue, and umbilical cord blood as sources of cell therapy. Int J Mol Sci *14*, 17986-18001.

Johnson, D.H., Richardson, T.M., and Epstein, D.L. (1989). Trabecular meshwork recovery after phagocytic challenge. Curr Eye Res *8*, 1121-1130.

Johnson, D.H., and Tschumper, R.C. (1987). Human trabecular meshwork organ culture. A new method. Invest Ophthalmol Vis Sci *28*, 945-953.

Johnson, D.H., and Tschumper, R.C. (1989). The effect of organ culture on human trabecular meshwork. Exp Eye Res *49*, 113-127.

Johnson, M. (2006). 'What controls aqueous humour outflow resistance?'. Exp Eye Res *82*, 545-557.

Johnson, M., McLaren, J.W., and Overby, D.R. (2017). Unconventional aqueous humor outflow: A review. Exp Eye Res *158*, 94-111.

Johnson, M., Shapiro, A., Ethier, C.R., and Kamm, R.D. (1992). Modulation of outflow resistance by the pores of the inner wall endothelium. Invest Ophthalmol Vis Sci *33*, 1670-1675.

Jokerst, J.V., Thangaraj, M., Kempen, P.J., Sinclair, R., and Gambhir, S.S. (2012). Photoacoustic imaging of mesenchymal stem cells in living mice via silica-coated gold nanorods. ACS Nano *6*, 5920-5930.

Joyce, N.C., Harris, D.L., and Zhu, C.C. (2011). Age-related gene response of human corneal endothelium to oxidative stress and DNA damage. Invest Ophthalmol Vis Sci *52*, 1641-1649.

Keller, K.E., and Acott, T.S. (2013). The Juxtacanalicular Region of Ocular Trabecular Meshwork: A Tissue with a Unique Extracellular Matrix and Specialized Function. J Ocul Biol *1*, 3.

Keller, K.E., Aga, M., Bradley, J.M., Kelley, M.J., and Acott, T.S. (2009). Extracellular matrix turnover and outflow resistance. Exp Eye Res *88*, 676-682.

Keller, K.E., Bradley, J.M., Vranka, J.A., and Acott, T.S. (2011). Segmental versican expression in the trabecular meshwork and involvement in outflow facility. Invest Ophthalmol Vis Sci *52*, 5049-5057.

Kempf, S., Hortsch, M., and MacCallum, D. (2013). Don MacCullum's Michigan Histology, Vol 2, 1 edn (University of Michigan Office of Technology Transfer).

Kern, S., Eichler, H., Stoeve, J., Kluter, H., and Bieback, K. (2006). Comparative analysis of mesenchymal stem cells from bone marrow, umbilical cord blood, or adipose tissue. Stem Cells *24*, 1294-1301.

Khlebtsov, N., and Dykman, L. (2011). Biodistribution and toxicity of engineered gold nanoparticles: a review of in vitro and in vivo studies. Chem Soc Rev *40*, 1647-1671.

Kim, J.W., Galanzha, E.I., Shashkov, E.V., Moon, H.M., and Zharov, V.P. (2009). Golden carbon nanotubes as multimodal photoacoustic and photothermal high-contrast molecular agents. Nat Nanotechnol *4*, 688-694.

Kimling, J., Maier, M., Okenve, B., Kotaidis, V., Ballot, H., and Plech, A. (2006). Turkevich method for gold nanoparticle synthesis revisited. J Phys Chem B *110*, 15700-15707.

Knepper, P.A., Goossens, W., and Palmberg, P.F. (1996). Glycosaminoglycan stratification of the juxtacanalicular tissue in normal and primary open-angle glaucoma. Invest Ophthalmol Vis Sci *37*, 2414-2425.

Kosoko, O., Quigley, H.A., Vitale, S., Enger, C., Kerrigan, L., and Tielsch, J.M. (1998). Risk factors for noncompliance with glaucoma follow-up visits in a residents' eye clinic. Ophthalmology *105*, 2105-2111.

Krumholz, A., Shcherbakova, D.M., Xia, J., Wang, L.V., and Verkhusha, V.V. (2014). Multicontrast photoacoustic in vivo imaging using near-infrared fluorescent proteins. Sci Rep *4*, 3939.

Kubelick, K.P., Snider, E.J., Ethier, C.R., and Emelianov, S. (2017). Photoacoustic Properties of the Anterior Eye. Journal of Biomedical Optics (In Preparation).

Kuiper, N.H. (1960). Tests concerning random points on a circle. Indagationes Mathematicae (Proceedings) *63*, 38-47.

Ladner, C.L., Yang, J., Turner, R.J., and Edwards, R.A. (2004). Visible fluorescent detection of proteins in polyacrylamide gels without staining. Anal Biochem *326*, 13-20.

Lee, D.A., and Higginbotham, E.J. (2005). Glaucoma and its treatment: a review. Am J Health Syst Pharm *62*, 691-699.

Levkovitch-Verbin, H., Quigley, H.A., Martin, K.R., Valenta, D., Baumrind, L.A., and Pease, M.E. (2002). Translimbal laser photocoagulation to the trabecular meshwork as a model of glaucoma in rats. Invest Ophthalmol Vis Sci *43*, 402-410.

Li, D.Q., and Pflugfelder, S.C. (2005). Matrix metalloproteinases in corneal inflammation. Ocul Surf *3*, S198-202.

Liton, P.B., Challa, P., Stinnett, S., Luna, C., Epstein, D.L., and Gonzalez, P. (2005). Cellular senescence in the glaucomatous outflow pathway. Exp Gerontol *40*, 745-748.

Liu, J., Wang, Y., Du, W., Liu, W., Liu, F., Zhang, L., Zhang, M., Hou, M., Liu, K., Zhang, S.*, et al.* (2013). Wnt1 inhibits hydrogen peroxide-induced apoptosis in mouse cardiac stem cells. PLoS One *8*, e58883.

Livak, K.J., and Schmittgen, T.D. (2001). Analysis of relative gene expression data using real-time quantitative PCR and the 2(-Delta Delta C(T)) Method. Methods *25*, 402-408.

Llobet, A., Gasull, X., and Gual, A. (2003). Understanding trabecular meshwork physiology: a key to the control of intraocular pressure? News Physiol Sci *18*, 205-209.

Loeffler, M., and Roeder, I. (2002). Tissue stem cells: definition, plasticity, heterogeneity, self-organization and models--a conceptual approach. Cells Tissues Organs *171*, 8-26.

Lu, Z., Zhang, Y., Freddo, T.F., and Gong, H. (2011). Similar hydrodynamic and morphological changes in the aqueous humor outflow pathway after washout and Y27632 treatment in monkey eyes. Exp Eye Res *93*, 397-404.

Luke, G.P., Nam, S.Y., and Emelianov, S.Y. (2013). Optical wavelength selection for improved spectroscopic photoacoustic imaging. Photoacoustics *1*, 36-42.

Lutjen-Drecoll, E. (1999). Functional morphology of the trabecular meshwork in primate eyes. Prog Retin Eye Res *18*, 91-119.

Macdonald, J.M., Geroski, D.H., and Edelhauser, H.F. (1987). Effect of inflammation on the corneal endothelial pump and barrier. Curr Eye Res *6*, 1125-1132.

MacQueen, L., Sun, Y., and Simmons, C.A. (2013). Mesenchymal stem cell mechanobiology and emerging experimental platforms. J R Soc Interface *10*, 20130179.

Manuguerra-Gagne, R., Boulos, P.R., Ammar, A., Leblond, F.A., Krosl, G., Pichette, V., Lesk, M.R., and Roy, D.C. (2013). Transplantation of mesenchymal stem cells promotes tissue regeneration in a glaucoma model through laser-induced paracrine factor secretion and progenitor cell recruitment. Stem Cells *31*, 1136-1148.

Mao, W.M., Tovar-Vidales, T., Yorio, T., Wordinger, R.J., and Clark, A.F. (2011). Perfusion-Cultured Bovine Anterior Segments as an Ex Vivo Model for Studying Glucocorticoid-Induced Ocular Hypertension and Glaucoma. Investigative Ophthalmology & Visual Science *52*, 8068-8075.

Marchini, G., Pagliarusco, A., Toscano, A., Tosi, R., Brunelli, C., and Bonomi, L. (1998). Ultrasound biomicroscopic and conventional ultrasonographic study of ocular dimensions in primary angle-closure glaucoma. Ophthalmology *105*, 2091-2098.

Masihzadeh, O., Ammar, D.A., Kahook, M.Y., Gibson, E.A., and Lei, T.C. (2013). Direct trabecular meshwork imaging in porcine eyes through multiphoton gonioscopy. J Biomed Opt *18*, 036009.

Mason, C., and Dunnill, P. (2008). A brief definition of regenerative medicine. Regen Med *3*, 1-5.

Matsumoto, Y., and Johnson, D.H. (1997). Trabecular meshwork phagocytosis in glaucomatous eyes. Ophthalmologica *211*, 147-152.

McCarron, M., Osborne, Y., Story, C.J., Dempsey, J.L., Turner, D.R., and Morley, A.A. (1987). Effect of age on lymphocyte proliferation. Mech Ageing Dev *41*, 211-218.

McKinnon, S.J., Goldberg, L.D., Peeples, P., Walt, J.G., and Bramley, T.J. (2008). Current management of glaucoma and the need for complete therapy. Am J Manag Care *14*, S20-27.

Morgan, J.T., Wood, J.A., Walker, N.J., Raghunathan, V.K., Borjesson, D.L., Murphy, C.J., and Russell, P. (2014). Human trabecular meshwork cells exhibit several characteristics of, but are distinct from, adipose-derived mesenchymal stem cells. J Ocul Pharmacol Ther *30*, 254-266.

Morrison, J.C., Moore, C.G., Deppmeier, L.M., Gold, B.G., Meshul, C.K., and Johnson, E.C. (1997). A rat model of chronic pressure-induced optic nerve damage. Exp Eye Res *64*, 85-96.

Nam, S.Y., Ricles, L.M., Suggs, L.J., and Emelianov, S.Y. (2012). In vivo ultrasound and photoacoustic monitoring of mesenchymal stem cells labeled with gold nanotracers. PLoS One *7*, e37267.

Nandi, N., Sen, A., Banerjee, R., Kumar, S., Kumar, V., Ghosh, A.N., and Das, P. (2010). Hydrogen peroxide induces apoptosis-like death in Entamoeba histolytica trophozoites. Microbiology *156*, 1926-1941.

Neofytou, E., O'Brien, C.G., Couture, L.A., and Wu, J.C. (2015). Hurdles to clinical translation of human induced pluripotent stem cells. J Clin Invest *125*, 2551-2557.

Niederkorn, J.Y. (2002). Immune privilege in the anterior chamber of the eye. Crit Rev Immunol *22*, 13-46.

Nolan, W. (2008). Anterior segment imaging: ultrasound biomicroscopy and anterior segment optical coherence tomography. Curr Opin Ophthalmol *19*, 115-121.

O'Brien, J., Wilson, I., Orton, T., and Pognan, F. (2000). Investigation of the Alamar Blue (resazurin) fluorescent dye for the assessment of mammalian cell cytotoxicity. Eur J Biochem *267*, 5421-5426.

Overby, D., Gong, H., Qiu, G., Freddo, T.F., and Johnson, M. (2002). The mechanism of increasing outflow facility during washout in the bovine eye. Invest Ophthalmol Vis Sci *43*, 3455-3464.

Overton, W.R. (1988). Modified histogram subtraction technique for analysis of flow cytometry data. Cytometry *9*, 619-626.

Pavlin, C.J., Harasiewicz, K., and Foster, F.S. (1992). Ultrasound biomicroscopy of anterior segment structures in normal and glaucomatous eyes. Am J Ophthalmol *113*, 381-389.

Philipp, W., Speicher, L., and Humpel, C. (2000). Expression of vascular endothelial growth factor and its receptors in inflamed and vascularized human corneas. Invest Ophthalmol Vis Sci *41*, 2514-2522.

Quigley, H.A., and Broman, A.T. (2006). The number of people with glaucoma worldwide in 2010 and 2020. The British journal of ophthalmology *90*, 262-267.

Raviola, G. (1982). Schwalbe line's cells: a new cell type in the trabecular meshwork of Macaca mulatta. Invest Ophthalmol Vis Sci *22*, 45-56.

Raykin, J., Snider, E., Bheri, S., Mulvihill, J., and Ethier, C.R. (2017). A modified gelatin zymography technique incorporating total protein normalization. Anal Biochem *521*, 8-10.

Raylman, R.R., Clavo, A.C., and Wahl, R.L. (1996). Exposure to strong static magnetic field slows the growth of human cancer cells in vitro. Bioelectromagnetics *17*, 358-363.

Reisman, M., and Adams, K.T. (2014). Stem cell therapy: a look at current research, regulations, and remaining hurdles. P T *39*, 846-857.

Reme, C., and d'Epinay, S.L. (1981). Periods of development of the normal human chamber angle. Doc Ophthalmol *51*, 241-268.

Ricles, L.M., Nam, S.Y., Sokolov, K., Emelianov, S.Y., and Suggs, L.J. (2011). Function of mesenchymal stem cells following loading of gold nanotracers. Int J Nanomedicine *6*, 407-416.

Ricles, L.M., Nam, S.Y., Trevino, E.A., Emelianov, S.Y., and Suggs, L.J. (2014). A Dual Gold Nanoparticle System for Mesenchymal Stem Cell Tracking. J Mater Chem B Mater Biol Med *2*, 8220-8230.

Roubeix, C., Godefroy, D., Mias, C., Sapienza, A., Riancho, L., Degardin, J., Fradot, V., Ivkovic, I., Picaud, S., Sennlaub, F.*, et al.* (2015). Intraocular pressure reduction and neuroprotection conferred by bone marrow-derived mesenchymal stem cells in an animal model of glaucoma. Stem Cell Res Ther *6*, 177.

Sacca, S.C., Pascotto, A., Camicione, P., Capris, P., and Izzotti, A. (2005). Oxidative DNA damage in the human trabecular meshwork: clinical correlation in patients with primary open-angle glaucoma. Arch Ophthalmol *123*, 458-463.

Sakuma, T., Sawada, A., Yamamoto, T., and Kitazawa, Y. (1997). Appositional angle closure in eyes with narrow angles: an ultrasound biomicroscopic study. J Glaucoma *6*, 165-169.

Schindelin, J., Rueden, C.T., Hiner, M.C., and Eliceiri, K.W. (2015). The ImageJ ecosystem: An open platform for biomedical image analysis. Mol Reprod Dev *82*, 518-529.

Schneider, C.A., Rasband, W.S., and Eliceiri, K.W. (2012). NIH Image to ImageJ: 25 years of image analysis. Nat Methods *9*, 671-675.

Sellami, D., Abid, S., Bouaouaja, G., Ben Amor, S., Kammoun, B., Masmoudi, M., Dabbeche, K., Boumoud, H., Ben Zina, Z., and Feki, J. (2007). Epidemiology and risk factors for corneal graft rejection. Transplant Proc *39*, 2609-2611.

Senatorov, V., Malyukova, I., Fariss, R., Wawrousek, E.F., Swaminathan, S., Sharan, S.K., and Tomarev, S. (2006). Expression of mutated mouse myocilin induces open-angle glaucoma in transgenic mice. J Neurosci *26*, 11903-11914.

Shareef, S.R., Garcia-Valenzuela, E., Salierno, A., Walsh, J., and Sharma, S.C. (1995). Chronic ocular hypertension following episcleral venous occlusion in rats. Exp Eye Res *61*, 379-382.

Sherwood, M.E., and Richardson, T.M. (1988). Phagocytosis by trabecular meshwork cells: sequence of events in cats and monkeys. Exp Eye Res *46*, 881-895.

Shuman, M.A., Polansky, J.R., Merkel, C., and Alvarado, J.A. (1988). Tissue plasminogen activator in cultured human trabecular meshwork cells. Predominance of enzyme over plasminogen activator inhibitor. Invest Ophthalmol Vis Sci *29*, 401-405.

Snider, E., Vannatta, R.T., Stamer, W.D., and Ethier, C.R. (2016). Co-Culture Stimulated Differentiation of Mesenchymal Stem Cells to Trabecular Meshwork Cells. Investigative Ophthalmology & Visual Science.

Snider, E.J., Kubelick, K.P., Tweed, K., Kim, R.K., Gao, K., Read, A., Emelianov, S.Y., and Ethier, C.R. (2018). Magnetic Nanoparticle Assisted Stem Cell Delivery to the Trabecular Meshwork. In Preparation.

Snider, E.J., Taylor Vannatta, R., Schildmeyer, L., Daniel Stamer, W., and Ross Ethier, C. (2017). Characterizing differences between MSCs and TM cells: Towards autologous stem cell therapies for the glaucomatous trabecular meshwork. J Tissue Eng Regen Med.

Song, J., Lee, P.P., Epstein, D.L., Stinnett, S.S., Herndon, L.W., Jr., Asrani, S.G., Allingham, R.R., and Challa, P. (2005). High failure rate associated with 180 degrees selective laser trabeculoplasty. J Glaucoma *14*, 400-408.

Sowden, J.C. (2007). Molecular and developmental mechanisms of anterior segment dysgenesis. Eye *21*, 1310-1318.

Spandidos, A., Wang, X., Wang, H., Dragnev, S., Thurber, T., and Seed, B. (2008). A comprehensive collection of experimentally validated primers for Polymerase Chain Reaction quantitation of murine transcript abundance. BMC Genomics *9*, 633.

Spandidos, A., Wang, X., Wang, H., and Seed, B. (2010). PrimerBank: a resource of human and mouse PCR primer pairs for gene expression detection and quantification. Nucleic Acids Res *38*, D792-799.

Stamer, D.W., Roberts, B.C., Epstein, D.L., and Allingham, R.R. (2000). Isolation of primary open-angle glaucomatous trabecular meshwork cells from whole eye tissue. Curr Eye Res *20*, 347-350.

Stamer, W.D., and Clark, A.F. (2016). The many faces of the trabecular meshwork cell. Exp Eye Res.

Stamer, W.D., and Clark, A.F. (2017). The many faces of the trabecular meshwork cell. Exp Eye Res *158*, 112-123.

Stamer, W.D., Seftor, R.E., Williams, S.K., Samaha, H.A., and Snyder, R.W. (1995). Isolation and culture of human trabecular meshwork cells by extracellular matrix digestion. Curr Eye Res *14*, 611-617.

Strašák, L., Vetterl, V., and Fojt, L. (2005). Effects of 50 Hz Magnetic Fields on the Viability of Different Bacterial Strains. Electromagnetic Biology and Medicine *24*, 293-300.

Stumpff, F., and Wiederholt, M. (2000). Regulation of trabecular meshwork contractility. Ophthalmologica *214*, 33-53.

Swaminathan, S.S., Oh, D.J., Kang, M.H., and Rhee, D.J. (2014). Aqueous outflow: segmental and distal flow. J Cataract Refract Surg *40*, 1263-1272.

Takahashi, K., Tanabe, K., Ohnuki, M., Narita, M., Ichisaka, T., Tomoda, K., and Yamanaka, S. (2007). Induction of pluripotent stem cells from adult human fibroblasts by defined factors. Cell *131*, 861-872.

Takahashi, K., and Yamanaka, S. (2006). Induction of pluripotent stem cells from mouse embryonic and adult fibroblast cultures by defined factors. Cell *126*, 663-676.

Tamm, E.R. (2002). Myocilin and glaucoma: facts and ideas. Prog Retin Eye Res *21*, 395-428.

Tamm, E.R. (2009). The trabecular meshwork outflow pathways: structural and functional aspects. Exp Eye Res *88*, 648-655.

Tanito, M., Kaidzu, S., Takai, Y., and Ohira, A. (2016). Association between systemic oxidative stress and visual field damage in open-angle glaucoma. Sci Rep *6*, 25792.

Tay, C.Y., Sathiyanathan, P., Chu, S.W., Stanton, L.W., and Wong, T.T. (2012). Identification and characterization of mesenchymal stem cells derived from the trabecular meshwork of the human eye. Stem Cells Dev *21*, 1381-1390.

Tektas, O.Y., and Lutjen-Drecoll, E. (2009). Structural changes of the trabecular meshwork in different kinds of glaucoma. Exp Eye Res *88*, 769-775.

Teramoto, S., Tomita, T., Matsui, H., Ohga, E., Matsuse, T., and Ouchi, Y. (1999). Hydrogen peroxide-induced apoptosis and necrosis in human lung fibroblasts: protective roles of glutathione. Jpn J Pharmacol *79*, 33-40.

Thomas, B.J., Galor, A., Nanji, A.A., El Sayyad, F., Wang, J., Dubovy, S.R., Joag, M.G., and Karp, C.L. (2014). Ultra high-resolution anterior segment optical coherence tomography in the diagnosis and management of ocular surface squamous neoplasia. Ocul Surf *12*, 46-58.

Treacy, O., Fahy, G., Ritter, T., and O'Flynn, L. (2016). Corneal Immunosuppressive Mechanisms, Anterior Chamber-Associated Immune Deviation (ACAID) and Their Role in Allograft Rejection. Methods Mol Biol *1371*, 205-214.

Tripathi, B.J., and Tripathi, R.C. (1989). Neural crest origin of human trabecular meshwork and its implications for the pathogenesis of glaucoma. Am J Ophthalmol *107*, 583-590.

Tsai, J.C., and Kanner, E.M. (2005). Current and emerging medical therapies for glaucoma. Expert Opin Emerg Drugs *10*, 109-118.

Turkevich, J. (1985). Colloidal gold. Part I. Gold Bulletin *18*, 86-91.

Turkevich, J., Stevenson, P.C., and Hillier, J. (1951). A Study of the Nucleation and Growth Processes in the Synthesis of Colloidal Gold. Discuss Faraday Soc, 55-&.

Vandesompele, J., De Preter, K., Pattyn, F., Poppe, B., Van Roy, N., De Paepe, A., and Speleman, F. (2002). Accurate normalization of real-time quantitative RT-PCR data by geometric averaging of multiple internal control genes. Genome Biol *3*, RESEARCH0034.

Wang, L.V., and Yao, J. (2016). A practical guide to photoacoustic tomography in the life sciences. Nat Methods *13*, 627-638.

Wang, X., and Seed, B. (2003). A PCR primer bank for quantitative gene expression analysis. Nucleic Acids Res *31*, e154.

Weber, A.J., and Zelenak, D. (2001). Experimental glaucoma in the primate induced by latex microspheres. J Neurosci Methods *111*, 39-48.

Weih, L.M., Nanjan, M., McCarty, C.A., and Taylor, H.R. (2001). Prevalence and predictors of open-angle glaucoma: results from the visual impairment project. Ophthalmology *108*, 1966-1972.

Weinreb, R.N. (2000). Uveoscleral outflow: the other outflow pathway. J Glaucoma *9*, 343-345.

Weinreb, R.N., Aung, T., and Medeiros, F.A. (2014). The pathophysiology and treatment of glaucoma: a review. JAMA *311*, 1901-1911.

Weinreb, R.N., and Khaw, P.T. (2004). Primary open-angle glaucoma. Lancet *363*, 1711-1720.

Xu, M.H., and Wang, L.H.V. (2006). Photoacoustic imaging in biomedicine. Rev Sci Instrum *77*.

Yanai, A., Hafeli, U.O., Metcalfe, A.L., Soema, P., Addo, L., Gregory-Evans, C.Y., Po, K., Shan, X.H., Moritz, O.L., and Gregory-Evans, K. (2012). Focused Magnetic Stem Cell Targeting to the Retina Using Superparamagnetic Iron Oxide Nanoparticles. Cell Transplant *21*, 1137-1148.

Ye, J., Coulouris, G., Zaretskaya, I., Cutcutache, I., Rozen, S., and Madden, T.L. (2012). Primer-BLAST: a tool to design target-specific primers for polymerase chain reaction. BMC Bioinformatics *13*, 134.

Yu, A.L., Fuchshofer, R., Kampik, A., and Welge-Lussen, U. (2008). Effects of oxidative stress in trabecular meshwork cells are reduced by prostaglandin analogues. Invest Ophthalmol Vis Sci *49*, 4872-4880.

Zhang, Z., Dhaliwal, A.S., Tseng, H., Kim, J.D., Schuman, J.S., Weinreb, R.N., and Loewen, N.A. (2014). Outflow tract ablation using a conditionally cytotoxic feline immunodeficiency viral vector. Invest Ophthalmol Vis Sci *55*, 935-940.

Zhao, J., Wang, S., Zhong, W., Yang, B., Sun, L., and Zheng, Y. (2016). Oxidative stress in the trabecular meshwork (Review). Int J Mol Med *38*, 995-1002.

Zhou, Y., Yun, H., Yang, E., Schuman, J.S., and Du, Y. (2015). Induction of Adipose-derived Stem Cells to Trabecular Meshwork Cells for Glaucoma. Investigative Ophthalmology & Visual Science *56*, 3279-3279.

Zhu, W., Gramlich, O.W., Laboissonniere, L., Jain, A., Sheffield, V.C., Trimarchi, J.M., Tucker, B.A., and Kuehn, M.H. (2016a). Transplantation of iPSC-derived TM cells rescues glaucoma phenotypes in vivo. Proc Natl Acad Sci U S A *113*, E3492-3500.

Zhu, W., Gramlich, O.W., Laboissonniere, L., Jain, A., Sheffield, V.C., Trimarchi, J.M., Tucker, B.A., and Kuehn, M.H. (2016b). Transplantation of iPSC-derived TM cells rescues glaucoma phenotypes in vivo. Proceedings of the National Academy of Sciences *113*, E3492-E3500.

Zode, G.S., Kuehn, M.H., Nishimura, D.Y., Searby, C.C., Mohan, K., Grozdanic, S.D., Bugge, K., Anderson, M.G., Clark, A.F., Stone, E.M.*, et al.* (2011). Reduction of ER stress via a chemical chaperone prevents disease phenotypes in a mouse model of primary open angle glaucoma. J Clin Invest *121*, 3542-3553.

Zucker, R.M., Massaro, E.J., Sanders, K.M., Degn, L.L., and Boyes, W.K. (2010). Detection of TiO2 nanoparticles in cells by flow cytometry. Cytometry A *77*, 677-685.

Zuk, P.A., Zhu, M., Ashjian, P., De Ugarte, D.A., Huang, J.I., Mizuno, H., Alfonso, Z.C., Fraser, J.K., Benhaim, P., and Hedrick, M.H. (2002). Human adipose tissue is a source of multipotent stem cells. Mol Biol Cell *13*, 4279-4295.